

## **General Disclaimer**

### **One or more of the Following Statements may affect this Document**

- This document has been reproduced from the best copy furnished by the organizational source. It is being released in the interest of making available as much information as possible.
- This document may contain data, which exceeds the sheet parameters. It was furnished in this condition by the organizational source and is the best copy available.
- This document may contain tone-on-tone or color graphs, charts and/or pictures, which have been reproduced in black and white.
- This document is paginated as submitted by the original source.
- Portions of this document are not fully legible due to the historical nature of some of the material. However, it is the best reproduction available from the original submission.

(NASA-TR-155949) EXCIMER LASERS Final  
Report, 30 May 1975 - 10 Jun. 1976 (Hughes  
Research Labs.) 129 p HC A07/MF A01

N78-19480

CSSL 20E

Unclas  
G3/36 07339

# EXCIMER LASERS

By

A.J. Palmer, L.D. Hess, R.R. Stephens, and D.M. Pepper

November 1977

Hughes Research Laboratories  
3011 Malibu Canyon Road  
Malibu, CA 90265

Prepared For  
NATIONAL AERONAUTICS AND SPACE ADMINISTRATION

Lewis Research Center  
2100 Brookpark Road  
Cleveland, OH 44135



1. Report No.		2. Government Accession No.		3. Recipient's Catalog No.	
4. Title and Subtitle  EXCIMER LASERS				5. Report Date November 1977	
				6. Performing Organization Code	
7 Author(s) A.J. Palmer, L.D. Hess, R.R. Stephens, and D.M. Pepper				8. Performing Organization Report No.	
9. Performing Organization Name and Address Hughes Research Laboratories 3011 Malibu Canyon Road Malibu, CA 90265				10. Work Unit No. V6864	
				11. Contract or Grant No. NAS 3-19707	
12. Sponsoring Agency Name and Address Dr. J.W. Dunning, Project Manager NASA Lewis Research Center 2100 Brookpark Road Cleveland, OH 44135				13. Type of Report and Period Covered FINAL 30 May 75 to 10 June 76	
				14. Sponsoring Agency Code 6344	
15. Supplementary Notes					
16. Abstract The results of a two-year investigation into the possibility of developing continuous wave excimer lasers are reported. The program included the evaluation and selection of candidate molecular systems and discharge-pumping techniques. The K Ar/K <sub>2</sub> excimer dimer molecules and the xenon fluoride excimer molecule were selected for study; each used a transverse and capillary discharge-pumping technique. Experimental and theoretical studies of each of the two discharge techniques applied to each of the two molecular systems are reported. Discharge stability and fluorine consumption were found to be the principle impediments to extending the XeF excimer laser into the continuous wave regime. Potassium vapor handling problems were the principal difficulty in achieving laser action on the K Ar/K <sub>2</sub> system. Of the four molecular systems and pumping techniques explored, the capillary-discharge-pumped K Ar/K <sub>2</sub> system appears to be the most likely candidate for demonstrating continuous wave excimer laser action primarily because of its predicted lower pumping threshold and a demonstrated discharge stability advantage.					
17. Key Words (Selected by Author(s)) Excimer lasers; KAr/K <sub>2</sub> excimer/dimer system; XeF excimer system; cw excimer lasers; discharge pumped excimer lasers.			18. Distribution Statement  Unclassified/Unlimited		
19. Security Classif. (of this report) Unclassified		20. Security Classif. (of this page) Unclassified		21. No. of Pages 129	22. Price*

## SUMMARY

This report covers a two-year period of work on the NASA LeRC research program on continuous wave (cw) excimer lasers. The primary objectives of the research program covered by this report are (1) to identify potential excimer molecules for visible and near visible cw laser operation based on electrical excitation, (2) to predict the specific operating conditions required for such laser action, and (3) to demonstrate cw laser gain on such a system in a laboratory experiment.

The first objective was approached on the basis of fundamental principles concerning the nature of an excimer transition. Strictly defined evaluation procedures for the selection of suitable cw excimer molecules were applied to the periodic table of elements. These evaluations resulted in the selection of the  $KXe/K_2$  excimer/dimer molecules and the XeF excimer molecule for further study. Self-sustained transverse and capillary discharges were the pumping techniques selected to be applied to these molecular systems.

The second objective was addressed largely with the use of computer modeling of the discharge kinetics. The modeling was a continuously evolving activity throughout the duration of the program.

Early in the program the evaluation and modeling results showed that the attainment of cw excimer laser action would require a significant advance in the state of the art of discharge pumping of excimer lasers, primarily with respect to the thermal dissipation problem. In view of the required state-of-the-art advance, a multidirectional approach to the third objective of the program was chosen wherein each of the pumping techniques would be explored experimentally on each of the two molecular systems selected. Thus, four separate experimental apparatus were used for this purpose, and experiments were carried out with all of them.

Difficulties in achieving the cw excimer laser oscillation that we anticipated in the evaluation and modeling, together with many materials problems, prevented a demonstration of cw excimer laser oscillation.

However, sufficient information was gained throughout the program to enable us to identify a narrower set of priorities which can now be used in any subsequent effort to develop cw excimer lasers. In particular, of the four combinations of excimer systems and pumping methods explored, the capillary discharge-pumped KXe/K<sub>2</sub> appears the closest to demonstrating cw excimer laser action, because of the lower predicted pumping threshold required compared to the other molecular system explored and to the predicted and demonstrated discharge stability.

## TABLE OF CONTENTS

SECTION		PAGE
1	INTRODUCTION . . . . .	1
2	FUNDAMENTAL REQUIREMENTS FOR A CW EXCIMER LASER SYSTEM. . . . .	3
	A. Extended Definition of an Excimer System and the Red Shift Requirement . . . . .	3
	B. Cooling Requirements . . . . .	5
	C. Discharge Stability . . . . .	7
3	SELECTION OF CANDIDATE CW EXCIMER MOLECULES AND PUMPING TECHNIQUES . . . . .	13
4	THEORETICAL EVALUATION OF OPERATING CONDITIONS FOR THE XeF EXCIMER SYSTEM . . . . .	27
	A. Modeling Procedures . . . . .	27
	B. Results and Discussion . . . . .	33
5	THEORETICAL MODEL OF OPERATING CONDITIONS FOR THE K Ar/K <sub>2</sub> SYSTEM . . . . .	39
	A. Modeling Procedures . . . . .	39
	B. Results and Discussion . . . . .	42
6	DISCHARGE EXPERIMENTS ON THE XeF EXCIMER SYSTEM . . . . .	51
	A. Capillary Discharge . . . . .	51
	B. Transverse Discharge . . . . .	78
7	DISCHARGE EXPERIMENTS ON THE KAr/K <sub>2</sub> EXCIMER/DIMER SYSTEM . . . . .	81
	A. Transverse Discharge . . . . .	81
	B. Capillary Discharge . . . . .	93
8	CONCLUSIONS . . . . .	107
	REFERENCES . . . . .	109
	APPENDIX . . . . .	111

LIST OF ILLUSTRATIONS

FIGURE		PAGE
1	Excimer and dimer potential energy curves . . . . .	4
2	Evaluation procedure applied to the periodic table . . . . .	14
3	Group I — Hydrogen . . . . .	15
4	Group I — Alkali metals: Na, K, Rb, Cs . . . . .	17
5	Transition element subgroup: Zn, Cd, Hg . . . . .	19
6	Groups V and VI: N, P, As, O, S, Se . . . . .	19
7	Group VII: F, Bi, Cl, I . . . . .	21
8	Group VIII: He, Ne, Ar, Kr, Xe . . . . .	22
9	Laser transition data: Kxe, K <sub>2</sub> . . . . .	23
10	Laser transition data: Hg <sub>2</sub> . . . . .	24
11	Laser transition data: XeF . . . . .	24
12	Capillary discharge pumped XeF excimer results: theory versus experiment . . . . .	34
13	Current density and small signal gain temporal profile for avalanche and AID discharges . . . . .	38
14	Na-Xe/Na <sub>2</sub> system-comparison with JILA model . . . . .	43
15	K Ar/K <sub>2</sub> capillary discharge: results . . . . .	45
16	K Ar/K <sub>2</sub> transverse discharge: results . . . . .	46
17	K Ar/K <sub>2</sub> transverse discharge system: absorption spectra . . . . .	48
18	K Ar/K <sub>2</sub> capillary discharge system: absorption spectra . . . . .	49
19	Rare-gas halide capillary discharge laser apparatus. . . . .	52
20	Schematic diagram of XeF capillary discharge tube and pulse circuit . . . . .	52
21	Experimental arrangement for absolute fluorescence measurements . . . . .	53

FIGURE		PAGE
22	Spectral profile of XeF excimer fluorescence from capillary discharge tube . . . . .	55
23	Quasi-cw operation of a typical NF <sub>3</sub> mixture in the 3-mm tube . . . . .	58
24	Optimized fluorescence for 3-mm tube experiments . . . . .	60
25	Quasi-cw operation in typical NF <sub>3</sub> mixture . . . . .	63
26	Quasi-cw operation in typical F <sub>2</sub> mixture . . . . .	65
27	Operation at 200 Torr with high helium concentration . . . . .	68
28	V-I data for NF <sub>3</sub> mixtures illustrating current density limit . . . . .	70
29	V-I data for NF <sub>3</sub> mixture illustrating the discharge stability condition . . . . .	72
30	Pressure dependence of fluorescence from a typical NF <sub>3</sub> mixture . . . . .	75
31	Optimized fluorescence in 1 mm bore tube for several NF <sub>3</sub> mixtures . . . . .	76
32	Fluorescence and discharge measurements for a typical F <sub>2</sub> mixture . . . . .	77
33	Schematic diagram of the apparatus used to investigate avalanche discharges in rare-gas monohalide device . . . . .	79
34	Photograph of KAr/K <sub>2</sub> transverse discharge apparatus. . . . .	82
35	Schematic of KAr/K <sub>2</sub> transverse discharge apparatus and optical monitoring equipment . . . . .	83
36	Calibrated spectral sensitivity of photomultiplier used for measurement of absolute excimer fluorescence power; RCA 7102, -1250 V; dark current — 5 x 10 <sup>-3</sup> μA . . . . .	86
37	Transmission spectra of potassium dimer at 325 <sup>o</sup> C and argon pressures from 0 to 105 psia . . . . .	88
38	Transmission spectra of atomic potassium at 325 <sup>o</sup> C and argon pressures from 0 to 40 psia . . . . .	89

FIGURE		PAGE
39	Current and voltage waveforms for potassium-argon transverse discharge at 325°C, 105 psia argon. . . .	90
40	Emission spectra of transverse discharge pumped potassium excimer at 325°C and 105 psia argon . . . .	91
41	Schematic diagram of KAr/K <sub>2</sub> capillary discharge apparatus . . . . .	94
42	Photograph of KAr/K <sub>2</sub> capillary apparatus in final stages of fabrication . . . . .	95
43(a)	Capillary discharge gas handling manifold . . . . .	96
43(b)	Schematic diagram of KAr/K <sub>2</sub> capillary discharge tube and pulse circuit . . . . .	96
44	Apparatus used for emission/absorption measurements. . . . .	98
45	Experimental arrangement for absolute fluorescence measurements . . . . .	99
46	I-V characteristic of K/Ar discharge . . . . .	102
47	Photomultiplier output of fluorescence . . . . .	102
48	Angular response of interference filter used for fluorescence measurements . . . . .	103
49	Potassium dimer (X → B) absorption spectrum . . . . .	103
50(a)	Potassium-argon absorption spectrum . . . . .	104
50(b)	Potassium-argon excimer emission spectrum . . . . .	104

**ORIGINAL PAGE IS  
OF POOR QUALITY**

## SECTION 1

### INTRODUCTION

An excimer laser transition is a transition between two electronic states of a diatomic molecule: the upper state is a bound state and the lower state is an unbound state. Such a transition will exhibit advantageous features when compared with other types of lasers. These include

- Broadband tunability ( $\Delta\lambda \sim 1000$  to  $2000 \text{ \AA}$ )
- High cw saturation power ( $\sim 50 \text{ kW/cm}^2$ )
- Large high-power system capability (low gain, fewer parasitic problems).

The excimer laser transition is thus uniquely suited to meeting NASA's ultimate cw high-power laser mission requirements.

The primary objectives of the NASA program covered by this report are (1) to identify potential excimer molecules for visible and near-visible cw laser operation based on electrical excitation, (2) to predict the specific operating conditions required for such laser action, and (3) to demonstrate cw laser gain on such a system in a laboratory experiment.

Accomplishments toward these objectives are covered in the following sections. Sections 2 and 3 cover the procedure for the selection of suitable cw candidate excimer molecules and pumping techniques. Sections 4 and 5 are devoted to the theoretical modeling of the selected cw excimer systems. Sections 6 and 7 report on the experiments that were carried out on these systems. Finally, conclusions are presented in Section 8. An appendix containing the listings of the computer programs that were used for theoretical modeling is also contained in this report.

## SECTION 2

### FUNDAMENTAL REQUIREMENTS FOR A CW EXCIMER LASER SYSTEM

#### A. EXTENDED DEFINITION OF AN EXCIMER SYSTEM AND THE RED SHIFT REQUIREMENT

The basic definition of an excimer laser transition is a transition that occurs between two electronic states of a diatomic molecule of which the lower state is a dissociative or repulsive state as in Figure 1(a). In our selection of candidate cw excimer systems we broaden the definition of an excimer system to include any molecular electronic transition that exhibits a continuum red shift relative to the transition between the associated parent atomic states, since it is this feature that is fundamentally responsible for the ability to maintain a cw population inversion on a broadened molecular electronic transition. To see this, one assumes that the molecular states are populated in thermal equilibrium with respect to their parent atomic states in accordance with the gas temperature, while the population of the atomic states are in thermal equilibrium at the electron temperature. The population ratio between the upper and lower molecular levels then can be written

$$\frac{N_u}{N_l} = \exp \left( \frac{\Delta(h\nu)}{T_g} - \frac{h\nu_o}{T_e} \right), \quad (1)$$

where  $\Delta(h\nu)$  is the red shift,  $h\nu_o$  is the atomic transition energy, and  $T_g$  and  $T_e$  is the gas temperature and electron temperature, respectively; we have omitted degeneracy factors for simplicity. Therefore, an inversion will result under this two-temperature equilibrium condition, if the ratio of gas to electron temperature is less than the fractional red shift, i.e., if

$$\frac{T_g}{T_e} < \frac{\Delta h\nu}{h\nu_o}, \quad (2)$$

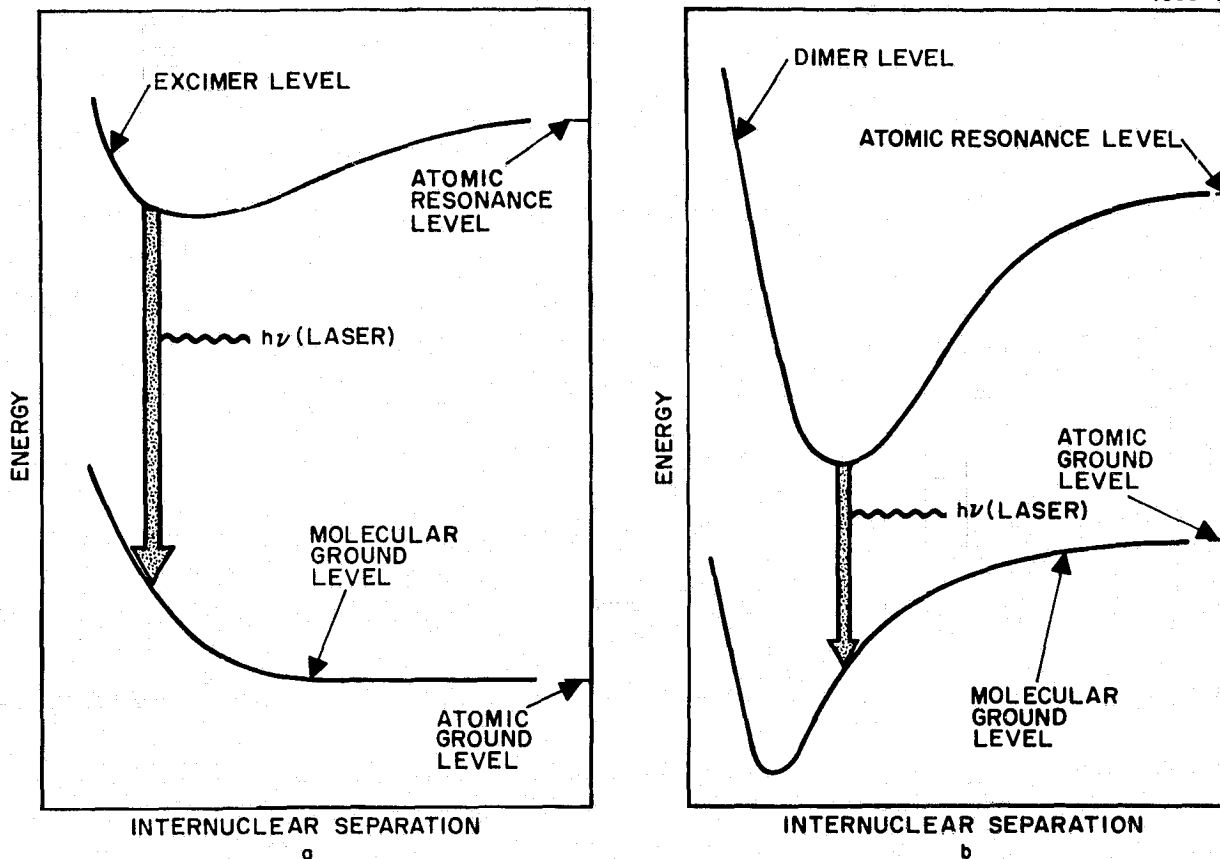


Figure 1. Excimer and dimer potential energy curves. (a) Excimer. (b) Dimer.

regardless of the bound or unbound nature of the molecular potential energy curves. An example situation, which exhibits the required red shift but does not involve a repulsive lower molecular level, is the dimer transition, illustrated in Figure 1(b), where the red shift is a result of the shift in the internuclear separations of the potential minima of two bound molecular states.

While the red shift requirement on the transition is not a necessary condition for achieving a population inversion for general pumping conditions, it is necessary for maintaining an inversion under the two temperature-equilibrium conditions assumed above; such an equilibrium condition will tend to develop at the high electron densities and high pressures required of excimer laser systems as cw conditions are approached.

## B. COOLING REQUIREMENTS

We have seen that the nature of an excimer laser transition under cw conditions will likely demand that the gas temperature always remain less than the electron temperature by at least the amount given by the fractional red shift of the transition (Eq. (2)). In selecting a cw pumping technique we must then ensure an adequate means of dissipating the thermal energy deposited into the gas mixture by the pump. Some general arguments can be presented at this stage as to the order of magnitude cooling requirements for a cw excimer laser.

The stimulated emission cross sections for visible-near visible excimer lasers average on the order of  $3 \times 10^{-17} \text{ cm}^2$ . To sustain a practical laser gain of 1% per centimeter required for laser action it is necessary to sustain an excimer level population density of  $\sim 3 \times 10^{14} \text{ cm}^{-3}$ . Visible transition excimer levels have a radiative decay rate of  $\sim 3 \times 10^7 \text{ sec}^{-1}$ . Discharge pumping efficiencies, from recent experiments, are near 1%. Thus, assuming a 1 to 3 eV photon, a minimum cw input power density of  $\sim 10^4$  to  $10^5 \text{ W/cm}^3$  must be provided to the excimer system for it to oscillate near threshold.

Under the high-pressure conditions required of most excimer systems the pump power coupled into the thermal energy of the gas is comparable to the power coupled into the excimer transition. Thus one must find a means of dissipating a power density comparable to the above values if the gas temperature is to be controlled and kept below the limit set by the red-shift requirement.

The three basic mechanisms for removing heat from the system are radiation, convection, and conduction. We consider now the requirements for each of these mechanisms to be applied to a cw excimer laser.

### 1. Radiation

For radiative cooling to reach the minimum required rate of  $10^4 \text{ W/cm}^2$  (assuming a transverse dimension of  $\sim 0.1$  to  $1 \text{ cm}$ ), the active medium would have to have an effective blackbody temperature of  $\sim 1 \text{ eV}$ . An excimer system in thermal equilibrium at this temperature will not exhibit a population inversion.

## 2. Convection

Convective cooling using gas flow at or near atmospheric pressure is commonly used to remove heat from high average power  $\text{CO}_2$  lasers such as the Hughes Peacemaker laser. In these devices the temperature is controlled simply by the residence time of a volume element of gas together with its specific heat:  $(3/2) NT \cong p \cdot (d/v_{\text{flow}})$ , where  $N$  is the gas density,  $p$  is the input power density,  $v_{\text{flow}}$  is the flow velocity, and  $d$  is the discharge dimension along the flow direction. It is easy to see that this technique is impractical for excimer lasers requiring a  $10^5 \text{ W/cm}^3$  power dissipation. With an input power of this magnitude at atmospheric pressure, sonic flow conditions ( $N = 3 \times 10^{19} \text{ cm}^{-3}$ ,  $v_{\text{flow}} \cong 10^5 \text{ cm/sec}$ ),  $d$  would have to be  $\lesssim 1 \text{ mm}$  to keep  $T < 1000^\circ\text{C}$ . If the lower end of the above threshold pumping range is relevant ( $\sim 10^4 \text{ W/cm}^3$ ), then convection may be practical.

## 3. Conduction

Thermal conduction of the heat to a wall in a static gas and its subsequent removal by flowing coolants can achieve  $10^4 \text{ W/cm}^2$ . This will be obtained for a helium gas mixture (independent of pressure) across an assumed thermal gradient of  $\sim 1000^\circ\text{C}$ , which is close to the upper limit defined by thermal bottlenecking of the population inversion and by the integrity of the wall material. For the  $10^5 \text{ W/cm}^3$  pumping requirement, surface-to-volume ratios of  $\sim 10$  will suffice for this mode of cooling. Some perspective on the use of thermal conduction to stabilize the gas temperature of cw lasers can be established by noting that capillary discharge pumping of  $\text{CO}_2$  waveguide lasers is now routinely used under cw conditions at pressures comparable to the pressures required of an excimer laser, although under significantly lower power loading. On the other hand, capillary discharges are also used for argon ion lasers under comparable power loading but at pressures lower than required for an excimer laser.

### C. DISCHARGE STABILITY

Discharge stability considerations are, of course, of paramount importance in considering cw operation of a discharge-pumped excimer laser. A wide range of discharge instabilities can occur in discharge-pumped lasers. Many of these instabilities, such as the various thermal instabilities, have relatively slow growth rates and can be stabilized by controlling the gas temperature or gas flow. However, there is one fairly fast-growing instability that is a particular problem with discharge-pumped excimer lasers and deserves special discussion. This is the two-step ionization instability which results from the high metastable or resonance level population required in these systems. Collisional ionization of these levels dominates the ionization of an excimer system pumped over laser threshold and leads to a quadratic increase of the ionization rate with electron density. The ionization is thus unstable when the electron loss rate varies only linearly with electron density as is the case for attachment or diffusion-controlled discharges. Recombination controlled discharges are only marginally stable against two-step ionization instabilities.

There are only four basic ways to achieve excimer laser threshold without encountering the above instability:

1. Establish the threshold input power in the discharge in a time that is short compared with the growth time of the instability (TEA and Bloomline fast-discharge devices).
2. Operate the discharge at below avalanche E/P values where the instability does not occur. This requires the use of an external source of ionization.
3. Stabilize the instability with a current-limiting element in the discharge circuit, such as a ballast resistor.
4. Operate the discharge in a regime which depletes the ionizing species thereby saturating the two-step ionization rate.

**ORIGINAL PAGE IS  
OF POOR QUALITY**

Approach No. 1 is a demonstrated means of obtaining discharge-pumped laser action on the rare-gas monohalide excimer systems. It is, by its definition, inapplicable to cw operation.

Approach No. 2, using an electron beam as the external source of ionization, is currently being pursued elsewhere for high average power operation on the rare-gas monohalide excimer lasers. It is not applicable to cw operation because of thermal loading of the electron beam foil window.

Approach No. 3 has been used for decades to stabilize low-to-moderate pressure gas discharges. Below we sketch a simple first-order stability analysis of the two-step ionization process which indicates the conditions under which a ballast resistor is expected to stabilize the two-step ionization.

The two-step ionization instability in an excimer laser is described by the following coupled-rate equations for electrons and the metastable (or resonance) level population:

$$\frac{d}{dt} n_e = R_i n^* n_e - \beta n_e \quad (3)$$

$$\frac{d}{dt} n^* = R_m n_e - n^*/\tau, \quad (4)$$

where  $n^*$  and  $n_e$  are the metastable (or resonance) level concentration and electron concentration, respectively,  $R_i$  is the rate constant (per  $n^*$ ) for ionization of the metastable,  $R_m$  is the production rate constant for metastables,  $\beta$  is the linear loss rate of electrons, and  $\tau$  is the effective lifetime of the metastable.

The steady-state solution to these equations is

$$n_{e_0} = \beta/R_i R_m \tau \quad (5)$$

and

$$n_o^* = R_m \tau n_{e_o} . \quad (6)$$

This solution is unstable as shown by linearizing Eqs. (3) and (4) with respect to the perturbed solution:

$$n_e = n_{e_o} + n'_e(t) \exp(\alpha t) \quad (7)$$

and

$$n^* = n_o^* + n^{*'}(t) \exp(\alpha t) . \quad (8)$$

This procedure gives

$$\alpha = 1/2 \times 1/\tau \times [-1 \pm \sqrt{1 + 4\beta\tau}] . \quad (9)$$

Thus the steady state solutions (5) and (6) are unstable with a growth rate given by the positive root for  $\alpha$ . However, if there is a ballast resistor in the discharge circuit, the rate constants  $R_m$  and  $R_i$  will be decreasing functions of  $n_e$ , and one must include this dependence in the linearized stability analysis. The most sensitive dependence will be on  $R_m$ , since it contains the most strongly varying Boltzmann factor ( $\exp(-E_m/Te)$ ) compared with  $\exp(-(E_i - E_m)/Te)$  for  $R_i$  where  $E_i$  and  $E_m$  are ionization and metastable level energies, respectively. Thus, in the perturbation analysis of Eqs. (3) and (4) we also write

$$R_m = R_{m_o} + \frac{d R_m}{d n_e} n_e . \quad (10)$$

ORIGINAL PAGE IS  
OF POOR QUALITY

After collecting terms linear in  $n_e'$  as before, the solution for  $\alpha$  will now have an added term:

$$\alpha = 1/2 \left[ 1/\tau - 1 \pm \sqrt{1 + 4\beta\tau \left( 1 + \frac{(dR_m/dn_e)}{R_{m0}} n_{e0} \right)} \right]. \quad (11)$$

To determine  $dR_m/dn_e$  we now make use of the fact that under conditions required for pumping excimer lasers, the dominant electron energy loss is caused by the inelastic collisional pumping of the metastable level. Thus the energy conservation relation for electrons can be written approximately as

$$J \times E = n_e R_m E_m, \quad (12)$$

where  $J$  and  $E$  are the current density and field in the discharge. If there is a ballast resistor in the circuit this equation can be written

$$eN_e V_d (V - IR)/\ell = n_e R_m E_m \quad (13)$$

where  $V$  is the maintained power supply voltage,  $I$  is the current,  $R$  is the ballast resistance,  $\ell$  is the discharge gap, and  $V_d$  is the drift velocity.

Using  $I = n_e V_d eA$  where  $A$  is the discharge area and  $e$  the electron charge we can write

$$\frac{dR_m}{dn_e} = \frac{V_d}{\ell E_m} RA V_d e = - \frac{R_{m0} RA V_d e}{V - IR} = \left( - \frac{R_{m0}}{n_{e0}} \right) \times \left( \frac{RI}{V - IR} \right). \quad (14)$$

Using Eq. (14) we see that stability is achieved if  $RI/(V - IR) \geq 1$ , i.e., the drop across the ballast resistor must be equal to or greater than the discharge voltage. The onset of discharge stability when this condition is met is revealed in the numerical modeling for the XeF

system presented in Section 4 as well as in the observed current-voltage waveforms in the capillary discharge-pumped XeF experiments discussed in Section 6.

Finally, approach No. 4 can be used for an excimer system whose active species is at a tenuous enough concentration that depletion of the ground state occurs. This will cause a saturation of the growth of  $n^*$  with  $n_e$  given by Eq. (1) and thereby quench the unstable growth of  $n_e$  with time given by Eq. (3). This quenching of the two-step ionization instability is also revealed in the numerical modeling results of the KAr excimer system presented in Section 6.

### SECTION 3

#### SELECTION OF CANDIDATE CW EXCIMER MOLECULES AND PUMPING TECHNIQUES

The search for potential excimer molecules began with the observation that every element in the periodic table will probably form at least one excimer or excimer-like (in the sense defined in Section 2) laser transition, either in a homonuclear or heteronuclear diatomic molecule. Thus, our preliminary evaluation of potential excimer molecules first involved various processes of elimination applied to the elements of the periodic table (Figure 2).

The first criterion applied in the elimination procedure is somewhat arbitrary but motivated by the desire for expediency. Since electrical excitation is to be used, it is required that the active medium be in the gas phase. In particular, we consider only those elements that have a vapor pressure greater than one Torr at temperatures below 500°C, and are reasonably abundant and nonradioactive. This leaves us with the following elements (see Figure 2):

Group I	H, Na, K, Rb, Cs
Group II	None
Transition Elements	Zn, Cd, Hg
Group III	None
Group IV	None
Group V	N, P, As
Group VI	O, S, Se
Group VII	F, Cl, Br, I
Group VIII	He, Ne, A, Kr, Xe

A further narrowing of the group of candidate excimer systems was then achieved through qualitative considerations on the nature of the known excimer or excimer-like transitions on both the heteronuclear diatomic molecule formed by the association of the element with a rare gas atom as well as on the homonuclear diatomic molecule. Figure 3 shows potential energy curves of a heteronuclear (excimer) and homonuclear (dimer) candidate molecule representative of each group, together with

## FIRST REQUIREMENTS:

1. VAPOR PRESSURE &gt; 1 Torr AT T &lt; 500 °C

2. REASONABLY ABUNDANT AND NONRADIOACTIVE

14

1s	1 H	
2s	3 Li	4 Be
3s	11 Na	12 Mg
4s	19 K	20 Ca
5s	37 Rb	38 Sr
6s	55 Cs	56 Ba
7s	87 Fr	88 Ra

3d	21 Sc	22 Ti	23 V	24 Cr $4s^1 3d^5$	25 Mn	26 Fe	27 Co	28 Ni	29 Cu $4s^1 3d^{10}$	30 Zn
4d	39 Y	40 Zr	41 Nb $5s^1 4d^4$	42 Mo	43 Tc	44 Ru $5s^1 4d^7$	45 Rh $5s^1 4d^8$	46 Pd $5s^0 4d^{10}$	47 Ag $5s^1 4d^{10}$	48 Cd
5d	57 La Lanthanides	72 Hf	73 Ta	74 W	75 Re	76 Os	77 Ir $6s^1 5d^9$	78 Pt $6s^1 5d^9$	79 Au $6s^1 5d^{10}$	80 Hg
6d	89 Ac Actinides									

2p	5 B	6 C	7 N	8 O	9 F	10 Ne $1s^2$
3p	13 Al	14 Si	15 P	16 S	17 Cl	18 Ar
4p	31 Ga	32 Ge	33 As	34 Se	35 Br	36 Kr
5p	49 In	50 Sn	51 Sb	52 Te	53 I	54 Xe
6p	81 Tl	82 Pb	83 Bi	84 Po	85 At	86 Rn
7p						

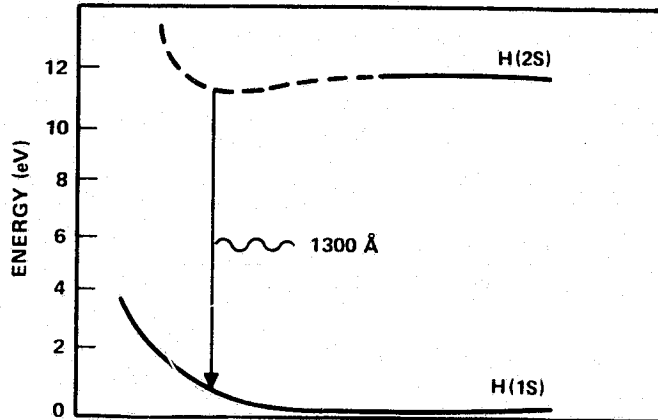
4f	58 Ce $5d^1 4f^1$	59 Pr $5d^0 4f^3$	60 Nd $5d^0 4f^4$	61 Pm ?	62 Sm $5d^0 4f^6$	63 Eu $5d^0 4f^7$	64 Gd $5d^1 4f^7$	65 Tb $5d^1 4f^8$	66 Dy ?	67 Ho ?	68 Er ?	69 Tm $5d^0 4f^{13}$	70 Yb $5d^0 4f^{14}$	71 Lu $5d^1 4f^{14}$
----	-------------------------	-------------------------	-------------------------	---------------	-------------------------	-------------------------	-------------------------	-------------------------	---------------	---------------	---------------	----------------------------	----------------------------	----------------------------

5f	90 Th $6d^2 5f^0$	91 Pa ?	92 U $6d^1 5f^3$	93 Np ?	94 Pu ?	95 Am $6d^0 5f^7$	96 Cm ?	97 Bk ?	98 Cf ?	99 Es ?	100 Fm ?	101 Md ?	102 No ?	
----	-------------------------	---------------	------------------------	---------------	---------------	-------------------------	---------------	---------------	---------------	---------------	----------------	----------------	----------------	--

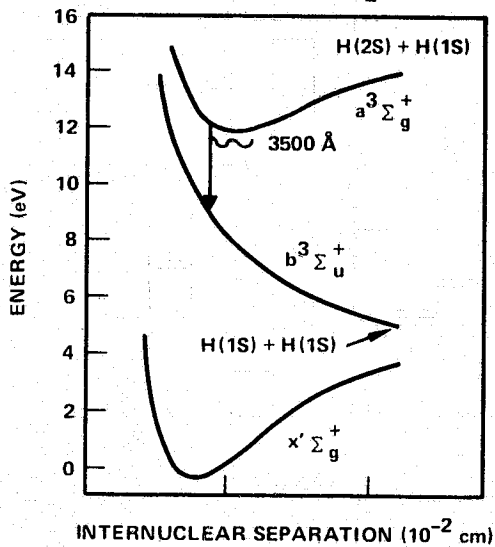
$s^1$     $s^2$     $d^1$     $d^2$     $d^3$     $d^4$     $d^5$     $d^6$     $d^7$     $d^8$     $d^9$     $d^{10}$     $p^1$     $p^2$     $p^3$     $p^4$     $p^5$     $p^6$

Figure 2. Evaluation procedure applied to the periodic table.

## EXCIMER (H Xe)



Problems: Wrong  
Wavelength  
Candidate Systems?: No

DIMER (H<sub>2</sub>)

Problems:  
No net gain due to photoionization  
of upper laser level

Candidate System?: No

Figure 3. Group 1 - Hydrogen.

a brief listing of problems and advantages associated with the use of the system as a cw excimer laser. References consulted for the survey are listed in Table 1. A brief summary of our considerations of these systems follows.

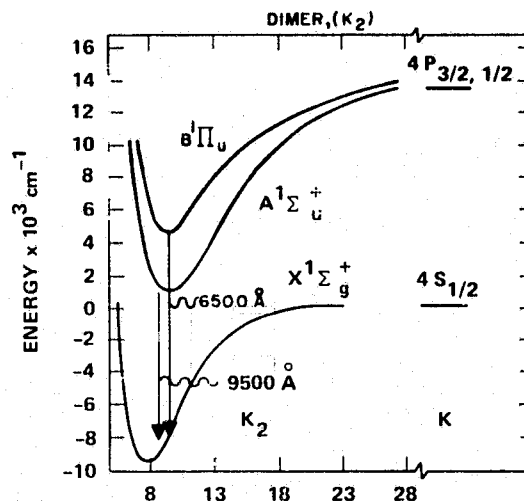
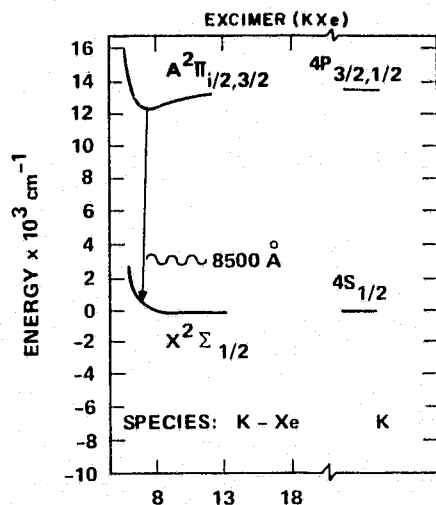
Table 1

EXIMER CANDIDATE	REFERENCE
HXe	1,2
H <sub>2</sub>	3
Kx <sub>e</sub>	4
K <sub>2</sub>	5
HgXe	1
Hg <sub>2</sub>	6,7,8
Xe O	9
Xe F	10
Xe <sub>2</sub>	11

T1937

Group I: Hydrogen — The bound-free excimer transition on the hydrogen rare-gas molecule, which correlates with the resonance transition, will lie in the vacuum ultraviolet and therefore is not a candidate system. The well-known bound-free transition at 3500 Å of H<sub>2</sub> has been investigated as a possible laser transition by Palmer several years ago (Ref. 3). It was found in that investigation that photoionization transitions from the upper laser level will not permit net gain to be realized on this system. The associated bound-bound transitions of H<sub>2</sub> are in the vacuum ultraviolet and involve well depths far too deep for the transition to be broadened into a continuum as is necessary to qualify it as an excimer-like transition. Therefore, hydrogen was not considered a good candidate element for this program.

Group I: Alkali Metals — The alkali metals are known to be excellent candidate excimer laser systems in both the A-X bound-unbound transition on the alkali-rare gas molecules and the A-X bound-bound transition of the alkali dimer molecules (Figure 4). The dimer transition is red shifted as required and is broadened into a continuum at buffer gas pressures greater than or near one atmosphere. The excimer laser features of these systems are discussed in detail in Refs. 5 and 12. Possible problems associated with the use of these systems for

**Advantages:**

- Good wavelength (near IR - visible)
- Strong oscillator strength
- No competing photoexcitation processes
- Low pumping threshold (flash-lamps, discharges)

**Problems:**

- Weak upper level binding (~0.1 eV)
- Thermal bottle-necking and dimer absorption at moderate temperatures
- High pressure alkali-rare gas mixture, difficult to handle

Candidate System: Yes

**Advantages:**

- Same as excimer except: potentially broader wavelength range and operation at lower pressure

**Problems:**

- Same as excimer except: can operate at slightly higher temperatures

Candidate System: Yes

Figure 4. Group 1 - Alkali metals: Na, K, Rb, Cs.

cw operation are thermal dissociation of the upper levels resulting from the relatively shallow well depths and discharge instabilities caused by the metal vapor gradients. The K-Xe/K<sub>2</sub> system was selected as the first of the three candidate cw excimer systems to be chosen from the preliminary evaluation. Potassium was chosen in favor of the other

alkalis because it requires the lowest oven vaporization temperatures of the alkalis whose excimer and dimer transitions both lie within the range of a silicon detector. Xenon is chosen in favor of the other rare gases because it forms the deepest excimer state well depth (resulting in the farthest red shift).

Zn, Cd, Hg Transition Element Subgroup — These elements have bound-free transitions to the ground state on both the heteronuclear rare-gas molecules and on the homonuclear dimer molecules (Figure 5).

In particular,  $\text{Hg}_2$  has both a visible excimer transition at  $4850 \text{ \AA}$  and an ultraviolet excimer transition at  $3350 \text{ \AA}$  which have been recognized for some time as potential laser transitions (Ref. 6). Gain measurements carried out on the  $4850 \text{ \AA}$  transition have revealed the same problem with this transition as with the  $\text{H}_2$  excimer transition, i.e., no net gain as a result of upper state absorption (Ref. 7). On the other hand, the  $3350 \text{ \AA}$  transition has now been shown to exhibit net gain both with probe laser gain measurements as well as with a recent demonstration of oscillation under optical pumping by a laser.\* The  $\text{Hg}_2 A^3 1_u \rightarrow X^1 \Sigma_g^+$   $3350 \text{ \AA}$  excimer transition was identified as another candidate cw excimer system.

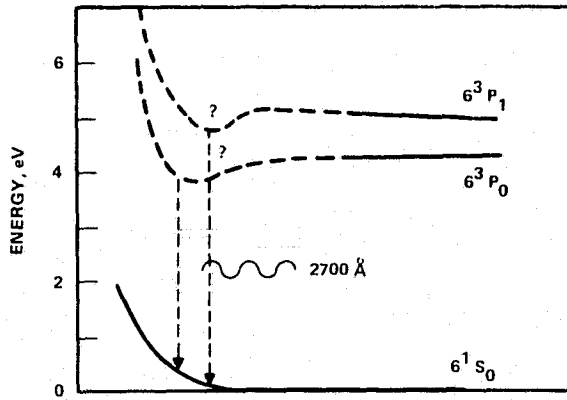
The corresponding heteronuclear Hg rare-gas excimer transition is not well studied. One can anticipate a weak oscillator strength for the transition and a weak excimer state binding a relatively short transition wavelength, probably about  $2700 \text{ \AA}$ , which will elevate the pumping power required for threshold. Thus the heteronuclear Hg rare-gas molecule is not admitted as a candidate system.

Groups V and VI — The excimer and dimer transition involving the Group V elements are similar to those involving the Group VI elements (Figure 6). Of the elements in these groups, oxygen has recently been particularly well studied as an excimer laser. The recently demonstrated XeO electron-beam pumped excimer laser operates on a bound-bound molecular transition which correlates with the atomic oxygen auroral transition. While this system may be well suited to large energy

---

\*V. Schlie, private communication.

EXCIMER (HgXe)



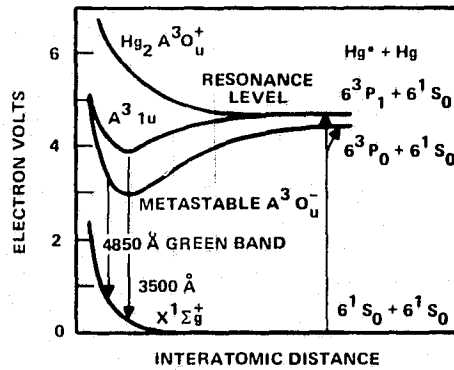
Problems:

- Weak oscillator strength
- Short wavelength
- Weak upper state binding
- Lack of data and theory on potential curves

Candidate System: No

DIMER (Hg<sub>2</sub>)

4388-8



Advantages:

- Measured gain on  $3^1u \rightarrow 1^1\Sigma_g$  transition
- Good wavelength

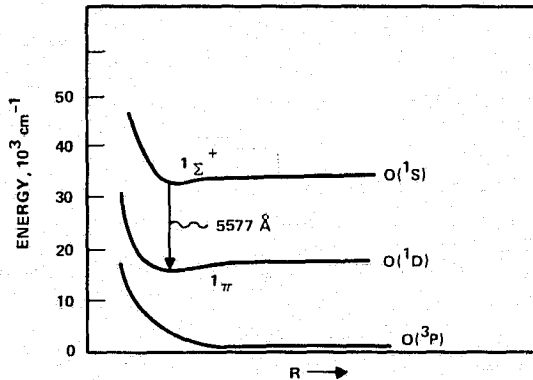
Problems:

- Weak upper state binding

Candidate System: Yes

Figure 5. Transition element subgroup: Zn, Cd, Hg.

EXCIMER (X<sub>g</sub>O)



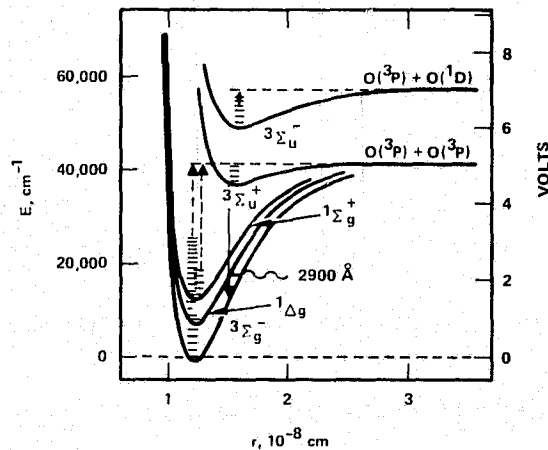
Problems:

- Extremely weak upper state binding ~0.05 eV
- Evidently a self terminating transition
- Collisionally induced dipole moment requires high pumping and high pressure

Candidate Systems: No

DIMER (O<sub>2</sub>)

4388-9



Problems:

- Lower level vibration structure
- Too large: cannot broaden
- Transition into a continuum and collisionally deactivate lower laser level

Candidate System: No

Figure 6. Groups V and VI: N, P, As, O, S, Se.

storage because of the long lifetime, it is poorly suited to cw application because of the evident self-terminating nature of the transition. The transition correlating with the resonance transition on both the heteronuclear excimer and homonuclear dimer molecules are in the vacuum ultraviolet and are also unsuitable for the present program.

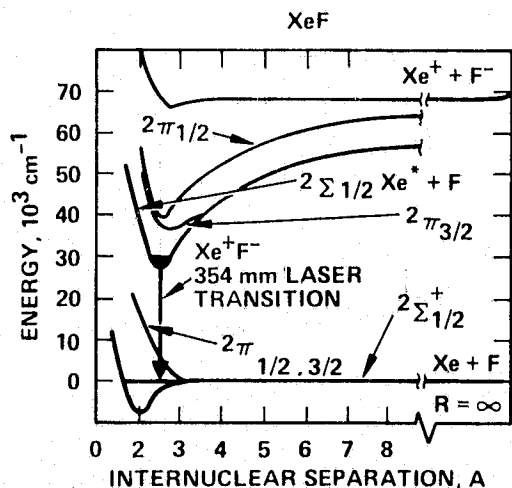
Group VII<sup>\*</sup> — The halogen rare-gas excimer molecules appeared to be one of the most promising systems of all for use as a cw excimer laser (Figure 7). Strong ionic-bonded excimer levels are formed by the association of a metastable rare-gas atom with a ground state halogen and the strongly allowed transition to the repulsive or weakly bound ground state is near 3000 Å. The deep excimer state well ( $\sim 4$  eV) will permit the use of high cw input power densities without upper state dissociation as occurs with the alkali systems. Also, because F, Br, and Cl are room-temperature gases, the experimental apparatus is enormously simplified. The XeF excimer transition at 3450 Å was chosen as the candidate excimer molecule from this class because it has the longest wavelength. The halogen dimer bound-bound transition correlating with the resonance transition is not suitable because of the short wavelength and deep well depths, with vibrational level spacing too large to be broadened into a continuum.

Group VIII — The rare gas dimer bound-unbound transitions are well known laser transitions, but they lie in the vacuum ultraviolet thus requiring very large pumping thresholds, and thus are not candidate systems for this program (Figure 8).

Having identified four specific candidate excimer molecules for detailed theoretical modeling, our next task was to assemble preliminary quantitative data on the laser transition. The four candidate excimer transitions selected and their approximate wavelength are

---

\* The halogen-mercury molecular systems are analogous to the halogen rare-gas system with Hg\* playing the role of the alkali. Lasing of the Hg-Cl excimer transition recently has been demonstrated at  $\sim 5580$  Å (Ref. 13).



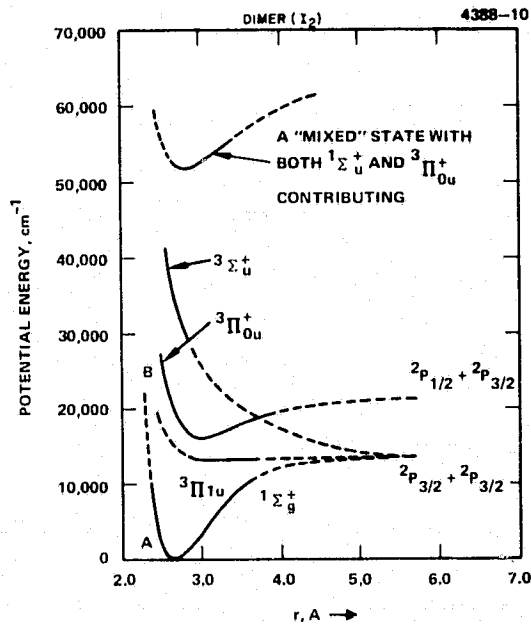
**Advantages:**

- Ideal wavelength
- Strong oscillator strength
- Strong upper state binding 4 eV
- Fast excimer association rates  $10^{-9} \text{ cm}^3 \text{ sec}^{-1}$
- Discharge pumping
- F, Be, Cl gasses at STP

**Problems:**

- Discharge stability?

Candidate System: Yes



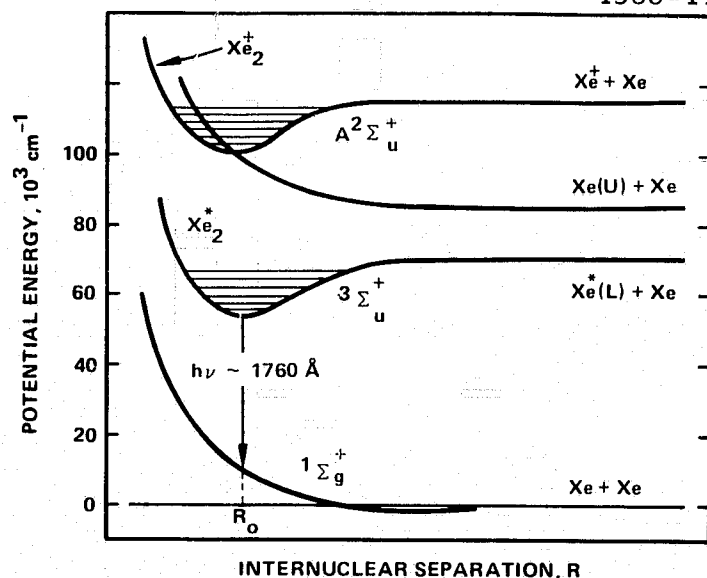
**Problem:**

Same as for Group V and VI dimers

Candidate System: No

Figure 7. Group VII: F, Bi, Cl, I.

...AL PAGE IS  
OF POOR QUALITY



Problems:  
Wrong Wavelength

Candidate Systems:  
No

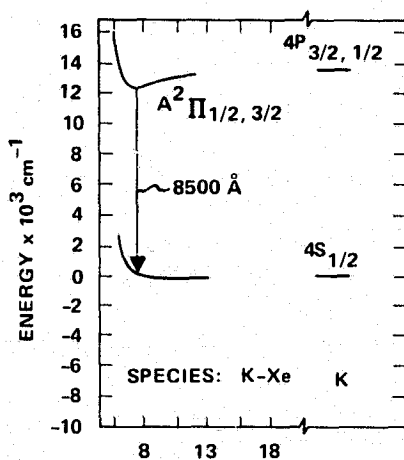
Figure 8. Group VIII: He, Ne, Ar, Kr, Xe.

- |     |  |          |
|-----|--|----------|
| (1) | $KXe \ 2\pi_{1/2,3/2} \rightarrow 2\Sigma_{1/2}$ | 8,500 Å  |
| (2) | $K_2 \ 1\Sigma_u^+ \rightarrow 1\Sigma_g^+$      | 10,400 Å |
| (3) | $Hg_2 \ A \ 31u \rightarrow X^1\Sigma^+$         | 3,350 Å  |
| (4) | $XeF \ 2\Sigma_{1/2} \rightarrow 2\Sigma_{1/2}$  | 3,450 Å  |

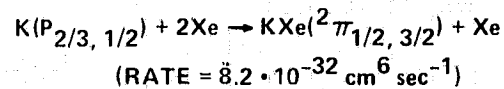
A compilation of pertinent quantitative data, including a set of potential energy curves for these transitions, is presented in Figures 9 through 11. References used for these data are the same as those listed in Table 1.

The primary criterion used in the selection of a pumping technique was the ability to meet the cooling and discharge stability requirement pointed out in Section 2. The cooling requirement might be met (if pumping thresholds are  $\lesssim 10^4 \text{ W/cm}^3$ ) with both a thermal conductivity

KXe



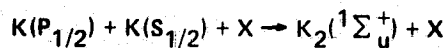
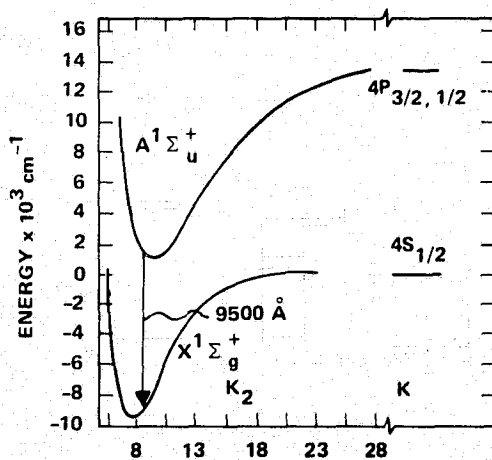
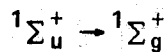
EXCIMER FORMATION REACTION:

LASER TRANSITION:  $^2\Pi_{1/2, 3/2} \rightarrow ^2\Sigma_{1/2}$ TRANSITION WAVELENGTH:  $\lambda \approx 8200 - 9000 \text{ \AA}$ UPPER LEVEL LIFETIME:  $\tau \approx 2.7 \cdot 10^{-8} \text{ sec}$ 

$$\text{STIMULATED CROSS SECTION: } \sigma_s \approx \frac{\lambda^3}{4\pi^3 c} \left( \frac{\lambda}{\Delta\lambda} \right) \cdot \tau^{-1}$$

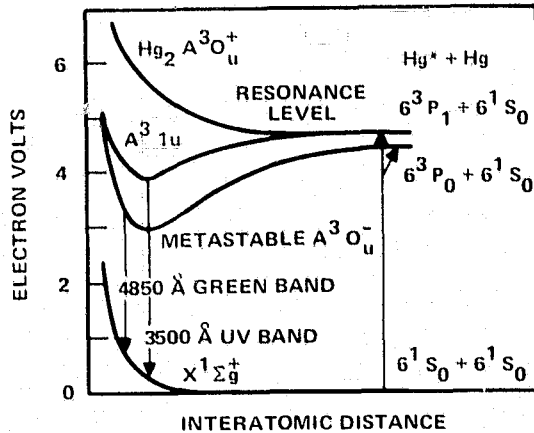
$$\approx 4 \cdot 10^{-16} \text{ cm}^2$$

$$\text{FRACTIONAL RED SHIFT } \frac{\nu - \nu_0}{\nu_0} \approx 0.092$$

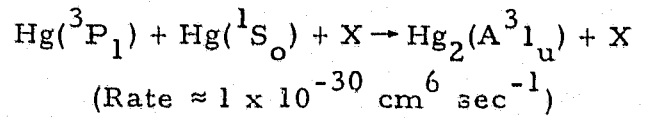
(EQUALS MAXIMUM  $T_g/T_e$  FOR 2-TEMPERATURE INVERSION)(RATE =  $8 \cdot 10^{-30} \text{ cm}^6 \text{ sec}^{-1}$ ) $\lambda \approx 9300 - 10,500 \text{ \AA}$  $\tau \approx 2.5 \cdot 10^{-8} \text{ sec}$  $\sigma \approx 1 \cdot 10^{-16} \text{ cm}^2$ 

$$\frac{\nu - \nu_0}{\nu_0} \approx 0.19$$

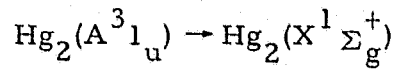
Figure 9. Laser transition data: Kxe, K<sub>2</sub>.

DIMER (Hg<sub>2</sub>)

Excimer formation reaction:



Laser transition:



Transition wavelength:

$$\lambda \approx 3000 - 3600 \text{ Å}$$

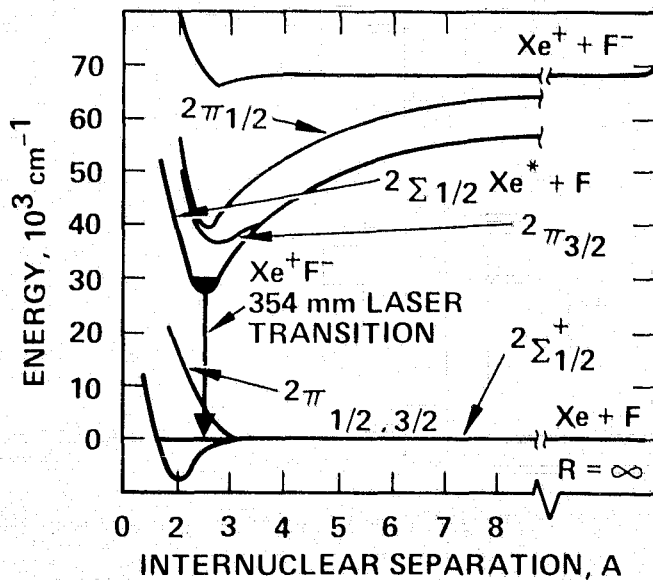
Upper level lifetime:  $\tau_u \approx 0.22 \text{ μsec}$ 

Stimulated emission cross section:

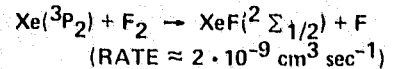
$$\sigma = 0.97 \times 10^{-18} \text{ cm}^2$$

Fractional red shift:  $\frac{\nu - \nu_0}{\nu_0} = 0.34$ Figure 10. Laser transition data: Hg<sub>2</sub>.

## XeF



EXCIMER FORMATION REACTION:

LASER TRANSITION:  $\text{XeF}(^2\Sigma_{1/2}') \rightarrow \text{XeF}(^2\Sigma_{1/2})$ TRANSITION WAVELENGTH:  $\lambda \approx 3250 - 3500 \text{ Å}$ UPPER LEVEL LIFETIME:  $\tau_u \approx 50 \cdot 10^{-9} \text{ sec}$ 

STIMULATED EMISSION CROSS SECTION:

$$\sigma \approx 0.5 \cdot 10^{-17} \text{ cm}^2$$

FRACTIONAL RED SHIFT  $\frac{\nu - \nu_0}{\nu_0} \approx 0.58$ 

Figure 11. Laser transition data: XeF.

stabilized capillary discharge and with a convectively stabilized transverse discharge. The latter technique can be scaled to meet cw power levels sufficient to meet NASA mission requirements, but the former technique can not be scaled. The capillary and transverse discharge techniques were chosen and applied to both the XeF excimer system and the K Ar/K<sub>2</sub> system. The capillary discharge was chosen for its simplicity in potentially offering an expedient first demonstration of cw excimer laser action; the transverse discharge was chosen for its ultimate scalability.

Ballast resistor stabilization of the two-step ionization was applied to the XeF discharge, while no such stabilization techniques were required for the K Ar/K<sub>2</sub> system because of the occurrence in that system of a ground state depletion and resonance level saturation effect. For the XeF capillary discharge a simple-series ballast resistor was employed in the discharge circuit in the usual manner while for the transverse XeF discharge experiments, a resistive electrode was used.

ORIGINAL PAGE IS  
OF POOR QUALITY

## SECTION 4

### THEORETICAL EVALUATION OF OPERATING CONDITIONS FOR THE XeF EXCIMER SYSTEM

This section summarizes theoretical modeling procedures and results for discharge pumping of the XeF excimer system. Modeling and experimental results are compared.

#### A. MODELING PROCEDURES

By means of numerical integration of the appropriate rate equations, the model follows the time evolution in the discharge of several excited and ionized species, the electron and gas temperatures, and the net small signal gain coefficient near the peak of the excimer gain band. The time dependence of the circuit currents and voltages is also included with a series resistance, a series inductance, and a storage capacitor as the modeled circuit elements.

The average electron energy is computed by solving the electron energy equation,

$$J \cdot E_{\text{disch}} = \sum_i (\text{inelastic collision rate } (Te))_i \times E_i + (\text{elastic collision rate}) \times 2 \left( \frac{M_e}{M_M} \right) \times Te, \quad (15)$$

where  $J$  is the current density,  $E_{\text{disch}}$  is the discharge electric field,  $E_i$  is the inelastic energy loss for the  $i^{\text{th}}$  process, and  $M_M$  and  $M_e$  are the masses of the major component species and electron, respectively. The metastable level pumping is assumed to be the dominant inelastic process contributing to the energy equation.

A Maxwellian energy distribution is assumed. The Maxwell distribution should be a fair approximation because of the dominance of two-step ionization processes over single-step ionization under the considered operating conditions. Only the latter process requires electrons with

energies in the tail of the distribution where a large reduction of the number of electrons from a Maxwellian distribution is known to occur.

The electron collisional rate constants are expressed in a form that results from assuming a linear rise of the cross section with energy above threshold (Ref. 14):

$$R(Te) = \frac{6 \times 10^2}{(e/m_e)/\pi} \frac{d\sigma}{d\varepsilon} \Big|_{\varepsilon_0} \left( \frac{2}{m_e} Te \right)^{3/2} \exp(-\varepsilon_0/Te) \left( 1 + \frac{\varepsilon_0}{2Te} \right), \quad (16)$$

where  $\varepsilon_0$  is the threshold energy for the excitation or ionization process,  $d\sigma/d\varepsilon|_{\varepsilon_0}$  is the rate of rise of cross section with energy above threshold, and  $m_e$  and  $e$  are electron mass and charge.

Also, in solving Eq. (15) we use an expression for the drift velocity obtained from Ref. 14:

$$V_{\text{drift}} = (2 Te/M_M)^{1/2}. \quad (17)$$

The gas temperature is calculated by assuming that all of the discharge power goes into gas heating and that heat is removed only by thermal conduction to a wall (assumed cylindrical).

$$\frac{d T_G}{dt} = J \cdot E_{\text{disch}} / (3/2 M) - (\text{thermal conductivity}) \\ \times \left( \frac{4.8}{\text{diameter}} \right)^2 \times (T_G - T_{\text{wall}}). \quad (18)$$

The discharge circuit response is governed by the familiar circuit equations.

$$V_{\text{disch}} = V_c(t) - L \times \frac{dI}{dt} - R \times I \quad (19)$$

$$V_c(t) = V_{\text{charge}} - 1/C \int I dt, \quad (20)$$

where  $V_{\text{disch}}$  is the discharge voltage,  $V_c$  is the capacitor voltage,  $V_{\text{charge}}$  is the initial charging voltage,  $I$  is the discharge current, and  $R$ ,  $L$ , and  $C$  are the series resistance, inductance, and storage capacitance, respectively.

The plasma, gas kinetic, and radiative processes included in the rate equations governing the species concentrations are presented in Tables 2, 3, and 4, together with source references and in the computer code listing presented in Section 1 of the appendix. (In the listing, a B at the end of the label refers to the back reaction that is computed by detailed balancing using the appropriate equilibrium constant or Boltzmann factor for the reaction.)

The small signal gain coefficient for the XeF system is computed as follows:

$$\text{gain} = \sigma_{\text{stim}} \times ([\text{XeF}^*] - [\text{XeF}_g] \times \exp(-0.074/T_G)) \quad (21)$$

where,

$$\sigma_{\text{stim}}(P) = \frac{\lambda^3}{4\pi^2 c} \times \left( \frac{\lambda}{\Delta\lambda(p)} \right) \times A_{\text{einst}}, \quad (22)$$

and  $\Delta\lambda$  is the measured half width of excimer band as a function of pressure,  $\lambda$  is the wavelength (3450 Å for XeF\*),  $A_{\text{einst}}$  is the A coefficient for the transition,  $[\text{XeF}^*]$  and  $[\text{XeF}_g]$  are the upper and lower laser level concentrations, and the Boltzmann function accounts for gas heating effects on the population distribution in the lower level.

The computer program listings in the appendix show how the coupled rate equations governing all of the above processes are integrated numerically using a time step chosen by the user and altered, if desired,

Table 2. Plasma Processes Modeled for the XeF Excimer System

LABEL	PROCESS	$\frac{d\sigma}{d\epsilon_{e0}}$	COMMENT
R1X	$e^- + Xe \rightleftharpoons Xe^* + e^-$	$0.3 \times 10^{-10} \text{ cm}^2 \text{ eV}^{-1}$ $0.05 \times 10^{-16} \text{ cm}^2 \text{ eV}^{-1}$	15 Rough Estimate
R37X	$e^- + Xe \rightleftharpoons Xe^{**} + e^-$		
R2X	$e^- + Xe \rightarrow Xe^+ + 2e^-$	$0.11 \times 10^{-16} \text{ cm}^2 \text{ eV}^{-1}$	15
R38X	$e^- + Xe^* \rightarrow Xe^+ + 2e^-$	$5 \times 10^{-16} \text{ cm}^2 \text{ eV}^{-1}$	Rough Estimate
R39X	$e^- + Xe^{**} \rightarrow Xe^+ + 2e^-$	$5 \times 10^{-16} \text{ cm}^2 \text{ eV}^{-1}$	Rough Estimate
R4X	$e^- + Xe_2^+ \rightarrow Xe^* + Xe$	$(\alpha =) 0.346 \times 10^{-8} (T_e \text{ (eV)})^{-1/2}$ $\text{cm}^6 \text{ sec}^{-1}$	16
R4MX	$e^- + XeM^+ \rightarrow Xe^* + M$	$(\alpha =) 0.346 \times 10^{-8} \times (T_e \text{ (eV)})^{-1/2}$ $\text{cm}^6 \text{ sec}^{-1}$	Rough Estimate
<b>Corresponding Processes for M species = Helium</b>			
R1	$e^- + M \rightleftharpoons M^* + e^-$	$0.025 \times 10^{-17} \text{ cm}^2 \text{ eV}^{-1}$	15
R137	$e^- + M \rightleftharpoons M^{**} + e^-$	$0.025 \times 10^{-17} \text{ cm}^2 \text{ eV}^{-1}$	Rough Estimate
R2	$e^- + M \rightarrow M^+ + 2e^-$	$0.08 \times 10^{-17} \text{ cm}^2 \text{ eV}^{-1}$	15
R38	$e^- + M^* \rightarrow M^+ + 2e^-$	$5 \times 10^{-16} \text{ cm}^2 \text{ eV}^{-1}$	Rough Estimate
R39	$e^- + M^{**} \rightarrow M^+ + 2e^-$	$5 \times 10^{-16} \text{ cm}^2 \text{ eV}^{-1}$	Rough Estimate
R4	$e^- + M_2^+ \rightarrow M^* + M$	$(\alpha =) 0.29 \times 10^{-8} (T_e)^{-1/2}$ $\text{cm}^6 \text{ sec}^{-1}$	16
REL	$e^- + M \rightarrow e^- + M$	$(\sigma =) 5.5 \times 10^{-16} \text{ cm}^2$ (elastic collisions)	15
R17	$e^- + F_2 \rightarrow F^- + F$	$(\beta =) 9.1 \times 10^{-10} (T_e)^{-2.16}$ $\exp(-0.165/T_e) \text{ cm}^3 \text{ sec}^{-1}$	17
R28	$e^- + XeF \rightleftharpoons XeF^* + e^-$	$(R_{\leftarrow} =) 2 \times 10^{-8} \text{ cm}^3 \text{ sec}^{-1}$	18
DEL	$e^- + Xe^+ + \text{wall} \rightarrow Xe$	(ambipolar diffusion) $Da = 2 \times 10^3 \times (3 \times 10^{16}/[M])$ $\cdot \sqrt{0.03/T_g} \cdot T_e$	14

Table 3. Gas Kinetic Processes Modeled for the XeF Excimer System

LABEL	PROCESS	RATE COEFFICIENT	COMMENT
G3	$M^+ + M + M \rightleftharpoons M_2^+ + M$	$3.7 \times 10^{-31} \times T_G^{1/2}$	All gas kinetic rates were obtained from Ref. 18 or from scaling arguments applied to rates given in Ref. 18.
G3X	$Xe^+ + Xe + M \rightleftharpoons Xe_2^+ + M$	$12 \times 10^{-31} \times T_G^{1/2}$	
G3MX	$Xe^+ + M + M \rightleftharpoons XeM^+ + M$	$5.8 \times 10^{-31} \times T_G^{1/2}$	
G5	$M^* + M + M \rightleftharpoons M_2^+ + M$	$12 \times 10^{-33} T_G^{1/2}$	
G5X	$Xe^* + Xe + M \rightleftharpoons Xe_2^* + M$	$15 \times 10^{-32} T_G^{1/2}$	
G5MX	$Xe^* + M + M \rightarrow XeM^* + M$	$47 \times 10^{-33} T_G^{1/2}$	
G13	$M^* + Xe \rightarrow Xe^+ + e^- + M$	$29 \times 10^{-10} T_G^{1/2}$	
G14	$M_2^* + Xe \rightarrow Xe^+ + e^- + M$	$29 \times 10^{-10} T_G^{1/2}$	
G18X	$Xe^* + F_2 \rightarrow XeF^* + F$	$34.7 \times 10^{-10} \times T_G^{1/2}$	
G20X	$Xe_2^* + F_2 \rightarrow XeF^* + F + Xe$	$35 \times 10^{-10} \times T_G^{1/2}$	
G22	$M^+ + F^- \rightarrow M^* + F$	$5 \times 10^{-7} T_G^{1/2}$	
G22X	$Xe^+ + F^- \rightarrow Xe^* + F$	$17 \times 10^{-7} T_G^{1/2}$	
G23	$M^+ + F^- + M \rightarrow MF^* + M$	$3 \times 10^{-25} T_G^{1/2}$	
G23X	$Xe^+ + F^- + M \rightarrow XeF^* + M$	$12 \times 10^{-25} T_G^{1/2}$	
G24	$M_2^+ + F^- \rightarrow M_2^* + F$	$5 \times 10^{-7} T_G^{1/2}$	
G24X	$Xe_2^+ + F^- \rightarrow Xe_2^* + F$	$17 \times 10^{-7} T_G^{1/2}$	
G25	$M_2^+ + F^- \rightarrow Xe_2^* + F$	$3 \times 10^{-25} T_G^{1/2}$	
G25X	$Xe_2^+ + F^- + M \rightarrow XeF^* + F + M$	$12 \times 10^{-25} T_G^{1/2}$	
G27X	$XeF^* + F_2 \rightarrow XeF + F + F$	$46 \times 10^{-10} T_G^{1/2}$	
G31	$M^* + M^* \rightarrow M_2^+ + e^-$	$10 \times 10^{-10} T_G^{1/2}$	
G31X	$Xe^* + Xe^* \rightarrow Xe_2^+ + e^-$	$30 \times 10^{-10} T_G^{1/2}$	
G31MX	$Xe^* + M^* \rightarrow XeM^+ + e^-$		
G32	$M^* + M_2^* \rightarrow M_2^+ + M + e^-$	$10 \times 10^{-10} T_G^{1/2}$	
G32X	$Xe^* + Xe_2^* \rightarrow Xe_2^+ + Xe + e^-$	$20 \times 10^{-10} T_G^{1/2}$	
G33	$M_2^* + M_2^* \rightarrow M_2^+ + 2M + e^-$	$10 \times 10^{-10} T_G^{1/2}$	
G33X	$Xe_2^* + Xe_2^* \rightarrow Xe_2^+ + 2Xe$	$30 \times 10^{-10} T_G^{1/2}$	

Table 3. Continued

LABEL	PROCESS	RATE COEFFICIENT	COMMENT
G33MX	$\text{XeM}^* + \text{XeM}^* \rightarrow \text{XeM}^+ + \text{M}^+\text{Xe} + e^-$	$20 \times 10^{-10} T_G^{1/2}$	
G34	$\text{M}^* + \text{XeF}^* \rightarrow \text{XeM}^* + \text{F} + e^-$	$10 \times 10^{-10} T_G^{1/2}$	
G34X	$\text{Xe}^* + \text{XeF}^* \rightarrow \text{Xe}_2^+ + \text{F} + e^-$	$30 \times 10^{-10} T_G^{1/2}$	
G35X	$\text{Xe}_2^* + \text{XeF}^* \rightarrow \text{Xe}_2^+ + \text{XeF} + e^-$	$30 \times 10^{-10} T_G^{1/2}$	
G35MX	$\text{XeM}^* + \text{XeF}^* \rightarrow \text{XeM}^+ + \text{XeF} + e^-$	$20 \times 10^{-10} T_G^{1/2}$	
G40	$\text{F} + \text{F} + \text{M} \rightarrow \text{F}_2 + \text{M}$	$1 \times 10^{-32} T_G^{1/2}$	
G41	$\text{F} + \text{Xe} + \text{M} \rightleftharpoons \text{F Xe} + \text{M}$	$2 \times 10^{-32} T_G^{1/2}$	
G44	$\text{F} + \text{Xe}^* + \text{M} \rightarrow \text{XeF}^* + \text{M}$	$6 \times 10^{-32} T_G^{1/2}$	
<b>Equilibrium Constants for Processes 3X, 5X, and 41</b>			
K3X		$1 \times 10^{-23} \exp(0.6/T_G)$	Rough Estimate
K5X		$1 \times 10^{-23} \exp(1.5/T_G)$	Rough Estimate
K41		$1 \times 10^{-23} \exp(0.074/T_G)$	Rough Estimate

T1944

Table 4. Radiative Processes Modeled for the XeF Excimer System

LABEL	PROCESS	RATE	REFERENCE
AX2	$\text{Xe}^{**} \rightarrow \text{Xe} + h\nu$	$4 \times 10^7 \text{ sec}^{-1}$	Rough Estimate
AXED1	$\text{Xe}_2^* \rightarrow \text{Xe} + \text{Xe} + h\nu$	$4 \times 10^7 \text{ sec}^{-1}$	Ref. 18
AXEF	$\text{XeF}^* \rightarrow \text{XeF} + h\nu$	$2 \times 10^7 \text{ sec}^{-1}$	Ref. 18
AMX	$\text{XeM}^* \rightarrow \text{Xe} + \text{M} + h\nu$	$10 \times 10^7 \text{ sec}^{-1}$	Rough Estimate
AM <sub>2</sub>	$\text{M}^{**} \rightarrow \text{M} + h\nu$	$32 \times 10^7 \text{ sec}^{-1}$	Rough Estimate
AMD1	$\text{M}_2^* \rightarrow \text{M} + \text{M} + h\nu$	$32 \times 10^7 \text{ sec}^{-1}$	Scaled from $\text{Xe}_2^*$ value in Ref. 18

T1945

during the course of the computer run. The computer program is run on a PDP10 computer.

#### B. RESULTS AND DISCUSSION

The XeF excimer model was used to predict the operating conditions for a XeF excimer laser in both a low-pressure and high-pressure regime. The low-pressure modeling results were of interest primarily for the capillary discharge and resistive electrode discharge pumping techniques, while the high-pressure modeling results were generated primarily to evaluate the feasibility of what we have termed the avalanche initiated discharge (AID) approach to cw operation of the system. Typical modeling results for both these regimes are discussed below.

A typical low-pressure modeling result is presented in Figure 12. In this case, experiments in the capillary discharge tube were carried out under the same conditions; the corresponding experimental results are shown in the inset. The curves are discharge current and voltage and the excimer level population density versus time.

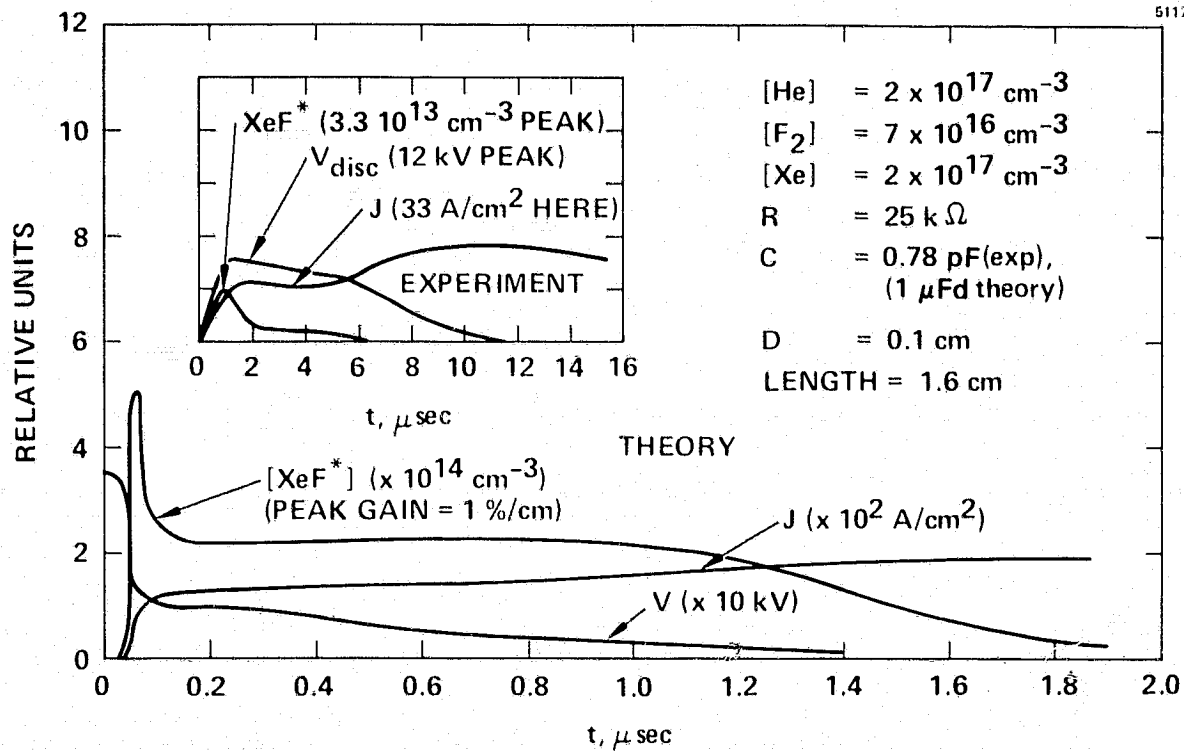


Figure 12. Capillary discharge pumped XeF excimer results: theory versus experiment.

As can be seen, the qualitative features of experimentally observed waveforms are well reproduced by the theory. The time scale over which these features occur is shorter for the theoretical case because of the high currents reached in modeling. In both the experimental and theoretical waveforms, three distinct phases of the temporal development are revealed: an initial transient phase, an intermediate steady-state phase, and a final terminated-fluorescence phase.

The initial phase in which the excimer fluorescence reaches its peak value is the transient period during which the discharge field and electron temperature attain their peak values. These values are limited by the discharge circuit inductance. This is the discharge phase during which XeF excimer laser action is being achieved in the TEA and Bloom line fast-discharge devices (although at higher buffer gas pressures). Although it may be possible to achieve laser action in the capillary discharge during this phase through optimization of the discharge risetime, what happens during this transient phase is immaterial for cw operation.

The intermediate steady-state phase of the discharge is the desired cw operating regime. Although not shown in the plot, the modeling results confirm that the gas temperature rise has been stabilized by thermal conduction to the wall during this phase. Also, as can be seen, the discharge is stable during this period because the two-step ionization was stabilized by the 25 k $\Omega$  ballast resistor. The magnitude of the excimer fluorescence and discharge current during this and the preceding transient phase of the discharge are lower in the experiment than those predicted by theory by factors of ten. The fluorescence during this phase would have to be increased by about a factor of ten to give a practical laser gain coefficient of  $\sim 1\%/cm$ .

For cw operation a more serious problem than the low value of observed fluorescence is the observed and predicted termination of fluorescence. This occurs in both the experimental and theoretical cases long before the discharge capacitor is drained and has been traced to the consumption of fluorine by the XeF excimer level pumping reaction itself (reaction G18X). We have identified, therefore, a

fundamental constraint to cw operation of an XeF excimer laser. The basic requirements for overcoming the fluorine consumption problem can be appreciated by examining the rate equation for  $F_2$ . Replenishment of  $F_2$  at the required rate by gas flow is not practical in a capillary tube so the rate equation is written for a static gas:

$$\frac{d[F_2]}{dt} = \Gamma_{\text{diss}} [Xe^*] [F_2] - \Gamma_{\text{rec}} [F_2]^2 [He] = 0$$

$$\parallel$$

$$4 \times 10^{21} \text{ cm}^{-3} \text{ sec}^{-1} \text{ (for 0.2\%/cm gain)} \quad (23)$$

and

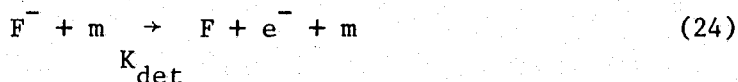
$$\Gamma_{\text{rec}} = 1.5 \times 10^{-33} \text{ cm}^3 \text{ sec}^{-1} .$$

To achieve a minimum practical laser gain of 0.2%/cm the pumping rate (equal to the consumption rate) must be  $\geq 4 \times 10^{21} \text{ cm}^{-3} \text{ sec}^{-1}$ . For molecular recombination to stabilize the  $F_2$  concentration at  $\sim [F_2] \approx 10^{17} \text{ cm}^{-3}$  where stable discharge operation is presently being achieved (higher  $F_2$  concentration will lead to impractically high discharge voltages to overcome the higher attachment loss), a 50% dissociation fraction and a third-body concentration of  $\sim 3 \times 10^{20} \text{ cm}^{-3}$  is required. In principle, the requirement of a high buffer gas pressure is not incompatible with the operation of cw capillary discharge pumping of this excimer system, since neither thermal conduction nor the two-step ionization instability is dependent on buffer gas pressure. Experimentally, however, attempts to elevate the buffer gas (helium) pressure above  $\sim 100$  Torr have led to filamenting of the discharge.

The XeF excimer model was also used to evaluate the AID approach. This approach to cw operation is based on a concept analogous to A. Hill's "Poker" discharge pumping of high pressure  $CO_2$  lasers (Ref. 19). In this technique the pumping is repetitively initiated with avalanche discharges whose pulse length is shorter than the growth time of the fastest discharge instability (in our case the two-step ionization

instability of Xe), and maintained between the avalanche pulses by an afterglow driven by a sub-avalanche field. Figure 13 shows the current and gain during the avalanche pulse and during an afterglow which was maintained by an avalanche field. Less relative stretching occurs on the gain pulse than on the current pulse, because the net attachment rate of the electrons in the afterglow can be made only slightly smaller than the afterglow time of the XeF excimer pumping process which occurs even in the absence of a subsequent sub-avalanche field. If lasing were occurring, the relative stretching would be much greater, but an afterglow time of more than a few hundred nanoseconds does not appear possible. Avalanche pulse repetitive rates on this time scale would be impractical.

An important process that could affect this approach and was not included in the computer model is electron detachment from negative fluorine ions caused by heavy particle collisions:



where m represents a heavy particle. The detachment rate depends on the ion temperature,  $T_i$  as follows (Ref. 20):

$$K_{det} = 1.3 \cdot 10^{-10} T_i^{1/2} \exp(-4.2 (T_i)) \text{ cm}^3/\text{sec} . \quad (25)$$

Unfortunately, for the detachment rate to be comparable to the attachment rate and thereby significantly affect the afterglow time, the afterglow field (which is controlling  $T_i$ ) would have to be higher than an avalanche field (Ref. 8) which would, of course, bring back the two-step ionization instability. Thus the AID concept was scrutinized and ultimately abandoned as a means toward developing cw XeF excimer lasers.

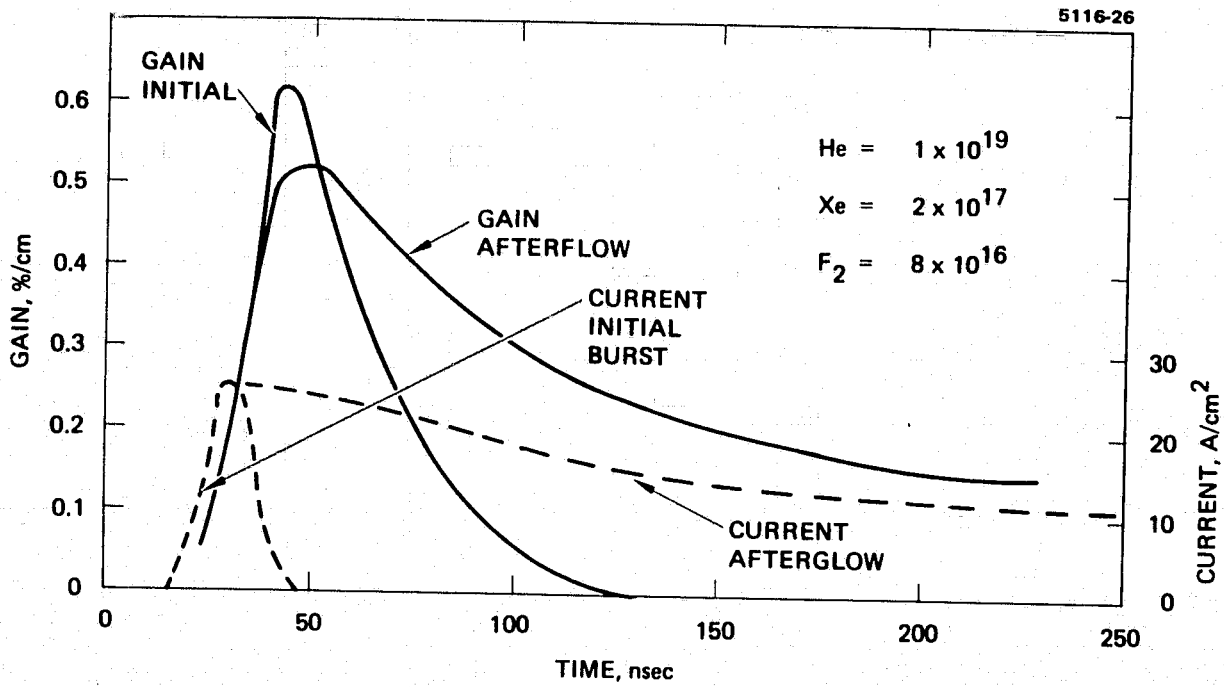


Figure 13. Current density and small signal gain temporal profile for avalanche and AID discharges.

ORIGINAL PAGE IS  
OF POOR QUALITY

## SECTION 5

### THEORETICAL MODEL OF OPERATING CONDITIONS FOR THE K Ar/K<sub>2</sub> SYSTEM

The modeling of the K Ar/K<sub>2</sub> excimer/dimer system parallels the procedure used for the XeF system. The model follows, by means of numerical integration of rate equations, the time evolution in the discharge of several excited and ionized species, the electron and gas temperatures, and the net small-signal gain coefficients near the peak of the excimer and dimer gain bands. The average electron energy, collisional rate, and drift velocity, the gas temperature, and the circuit response are computed on the basis of Eqs. (15) through (20) presented in Section 4.

#### A. MODELING PROCEDURES

The plasma and gas kinetic processes included in the rate equations governing the species concentrations are listed below. The rate constants, cross sections, and equilibrium constants for these processes can be found in the computer code listing included in the appendix, and, together with a source reference, in Table 5. An R label refers to a plasma process and a G label refers to a gas kinetic process. In the listing, a B at the end of the label refers to the back reaction, which is computed by detailed balancing using the appropriate equilibrium constant or Boltzmann factor reaction. The particular case presented refers to a potassium-xenon mixture.

#### Plasma Processes Modeled

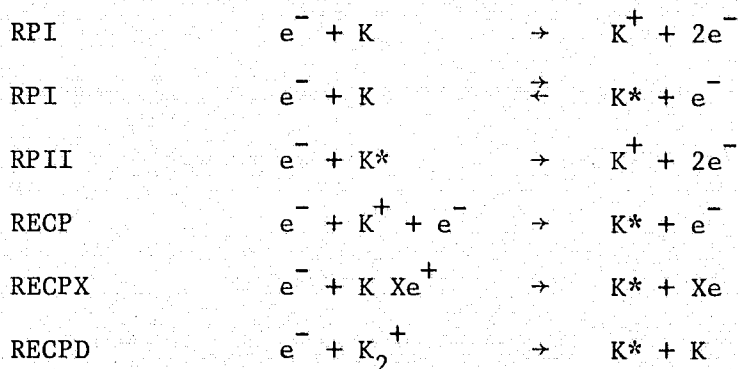


Table 5. Cross Sections, Rate Constants, Equilibrium Constants and Source References Used for Discharge Pumped K-Xe/K<sub>2</sub> Modeling

Parameter	Value	Comments
Inelastic electron collision cross sections: initial slope of cross sections with respect to energy above threshold		
CP1	$6 \times 10^{-15} \text{ cm}^2/\text{eV}$	Ref. 15
CPI	$0.5 \times 10^{-16} \text{ cm}^2/\text{eV}$	Ref. 15
CP11	$3 \times 10^{-15} \text{ cm}^2/\text{eV}$	Ref. 21 (sodium)
Recombination coefficients		
Three-body RECP	$2.28 \times 10^{-26} \times [\text{K}^+] \times [\text{Ne}]^2 \times T_e^{(-4.39)} \text{ cm}^{-3} \text{ sec}^{-1}$	Ref. 22 (cesium)
Dissociative - (K Xe <sup>+</sup> )		
RECPX	$1 \times 10^{-8} \times [\text{KXe}^+] \times [\text{Ne}] \text{ cm}^{-3} \text{ sec}^{-1}$	Ref. 21 (sodium)
Dissociative - (K <sub>2</sub> <sup>+</sup> )		
RECPD	$1 \times 10^{-8} \times [\text{K}_2^+] \times [\text{Ne}] \text{ cm}^{-3} \text{ sec}^{-1}$	Ref. 21 (sodium)
Photoionization cross section		
CPHI	$0.5 \times 10^{-19} \text{ cm}^2$	Ref. 5
Electron elastic cross section		
CEL	$3 \times 10^{-15} \text{ cm}^2$	Rough estimate
Heavy particle elastic cross section		
CDIF	$1 \times 10^{-15} \text{ cm}^2$	Rough estimate
Gas kinetic rates		
GPD	$8 \times 10^{-32} \times [\text{Xe}] \times [\text{K}] \times [\text{K}^+] \text{ cm}^{-3} \text{ sec}^{-1}$	Ref. 5
Equilibrium constants		
KAEX	$2.2 \times 10^{-23} \times \exp(0.074/T_g) \text{ cm}^3$	Ref. 23 (rubidium)
KXDI	$1.8 \times 10^{-22} \times \exp(0.56/T_g) \text{ cm}^3$	Ref. 5
KADI	$6.5 \times 10^{-23} \times \exp(0.735/T_g) \text{ cm}^3$	Ref. 5

5947

ORIGINAL PAGE IS  
OF POOR QUALITY

### Gas Kinetic Processes Modeled

GPX	K + 2 Xe	↕ ↔	K Xe + Xe
GPD	K + K + Xe	↕ ↔	K <sub>2</sub> + Xe
GPXL	K* + 2 Xe	↕ ↔	K Xe* + Xe
GPDL	K* + K + Xe	↕ ↔	K <sub>2</sub> * + Xe
GPXI	K <sup>+</sup> + 2 Xe	↕ ↔	K Xe <sup>+</sup> + Xe
GPDI	K <sup>+</sup> + K + Xe	↕ ↔	K <sub>2</sub> <sup>+</sup> + Xe

### Radiative Processes Modeled

AT	K*	→	K + hν (trapped)
AP	K**	→	K + hν
AP	KXe*	→	KXe + hν
AP	K <sub>2</sub> *	→	K <sub>2</sub> + hν

Under the conditions we consider ( $[Xe] \approx 1 \times 10^{20} \text{ cm}^{-3}$ ), the gas kinetic rates dominate the electron collisional rates in controlling the population of the molecular states. Therefore, we assume thermal equilibrium between the molecular states and their dissociation products. An exception is the A state of K<sub>2</sub>, for which radiative losses are included since they can compete with the dissociation rate.

The small-signal gain coefficient for the KXe/K<sub>2</sub> system is computed from the quasi-static theory of line broadening as in Ref. 24:

$$\begin{aligned}
 \text{gain}(\lambda) = & \sigma_{\text{stim,ex}}(\lambda) \left\{ [KXe^*] \times \frac{\exp(-V_{A,Ex}(\lambda)/T_G)}{(K_{eq A,Ex} \times 3/2)} \right. \\
 & \left. - 2 \times [K] \times [Xe] \times \exp(-V_{x,Ex}(\lambda)/T_G) \right\} \\
 & + \sigma_{\text{stim,Di}}(\lambda) \left\{ [K_2^*] \times \frac{\exp(-V_{A,Di}(\lambda)/T_G)}{(K_{eq A,Di} \times 12)} \right. \\
 & \left. - 0.25 \times [K]^2 \times \exp(-V_{x,Di}(\lambda)/T_G) \right\} \quad (26)
 \end{aligned}$$

$$\sigma_{\text{stim}}(\lambda)_{\text{Ex}} = (A_E/2c) \times \frac{2}{R_{\text{Ex}}^2} \times \frac{R_{\text{Ex}}^2}{D_i} \times \frac{dR(\lambda)}{d\nu} \Big|_{\text{Ex}}, \quad (27)$$

where  $\lambda$  and  $\nu$  are the transition wavelength and frequency,  $c$  is the speed of light,  $R_{\text{Ex}}$  is the internuclear separation on the excimer or dimer band corresponding to the wavelength,  $\lambda$ ,  $A_E$  is the Einstein A coefficient assumed equal to the resonance line at coefficient for both the excimer and dimer bands,  $V(\lambda)$ s are the potential energies of the molecular state measured relative to their dissociation products, and  $K_{\text{eq,A,Ex}}$  and  $K_{\text{eq,A,Di}}$  are the equilibrium constants for the excimer and dimer A states. This notation follows that used in Ref. 24.

## B. RESULTS AND DISCUSSION

During the development of the  $KAr/K_2$  model at Hughes Research Laboratories the results of another model of a discharge-pumped  $NaXe/Na_2$  system became available (Ref. 12). This model used a full Boltzmann equation analysis of the electron energy distribution. Although such an analysis is a more accurate approximation of the electron energy distribution than our assumed Maxwellian distribution, it is also more costly and time consuming. Also, it was anticipated that for the cw domain of operating condition of the alkali excimer systems, the actual energy distribution would be very close to a Maxwellian because of the high electron densities and the effects of super-elastic collisions. As a check on the validity of the Maxwellian approximation for the cw regime we applied our model to the  $NaXe/Na_2$  system to make a comparison of results with the full Boltzmann code model.

In applying our model to the  $NaXe/Na_2$  system we changed the potassium resonance level and ionization level energies, the resonance level A coefficient, and the vapor pressure constants to those for sodium but left the cross section unchanged. A comparison of the two models under these conditions is shown in Figure 14. Although the results of the two models do differ during the transient phase of the

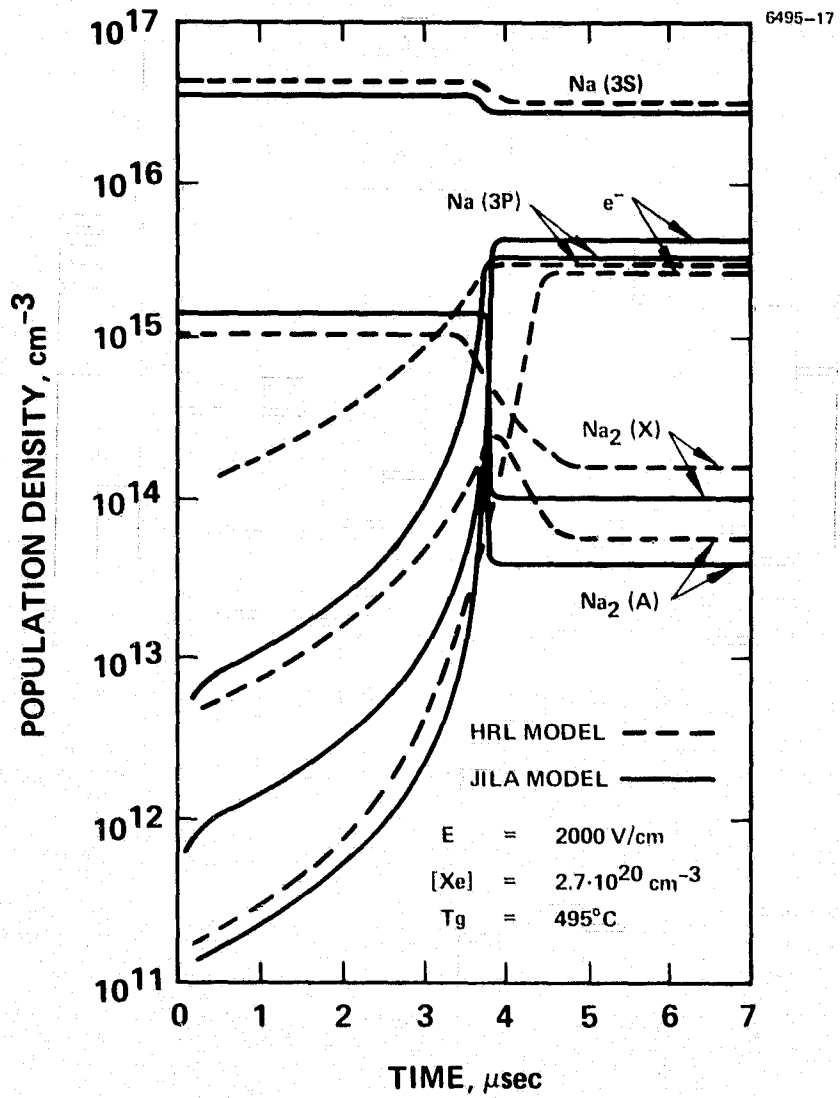


Figure 14. Na-Xe/Na<sub>2</sub> system-comparison with JILA model.

discharge, they are in close agreement during the steady-state phase, which is the region of interest for cw operation. Together with cost effectiveness, this result provides a good justification for our use of the Maxwellian electron energy distribution approximation in our model of the K Ar/K<sub>2</sub> system.

It is important to note that a steady-state regime is reached in spite of the fact that the discharge is dominated by two-step ionization and occurs without the use of a ballast resistor as would be required for the steady-state operation of the XeF system. In this case the two-step ionization instability is evidently being suppressed by the depletion of the ground state and by the quadratic dependence on electron density of the recombination rate as discussed in Section 2.

We applied our model to the K Ar/K<sub>2</sub> system for the conditions of the experiments both in the capillary discharge and the transverse discharge. In these cases a finite storage capacitance was used in the circuit response portion of the model. Typical results are shown in Figures 15 and 16. The corresponding experimental results (discussed further in Section 7) are included.

In the case of the transverse discharge the predicted current densities and fluorescence levels are more than an order of magnitude greater than the observed experimental values. The theoretical peak of the laser gain on the excimer and dimer bands for this case are on the order of  $2 \times 10^{-3} \text{ cm}^{-1}$  and  $1 \times 10^{-2} \text{ cm}^{-1}$ , respectively. Possible explanations for the large discrepancy between theory and experiment is discussed in Section 7.

In the case of the capillary discharge, the theoretical and experimental values appear to be in better agreement, although there is a measurement problem for the fluorescence.

In both the transverse and capillary discharge results, the predicted small-signal gain pulse has a shorter duration than the fluorescence as a result of gas heating. This is problematic for cw operation. However, this result is based on the extreme assumption that all of the discharge power goes into gas heating and is also presumably far from optimal operating conditions for cw operation.

$T = 330^\circ$   
 $[Ar] = 1.1 \times 10^{19} \text{ cm}^{-3}$   
 $V_c = 2 \text{ kV (5 cm DISCHARGE LENGTH)}$   
 $C = 0.0084 \mu\text{F}$

45

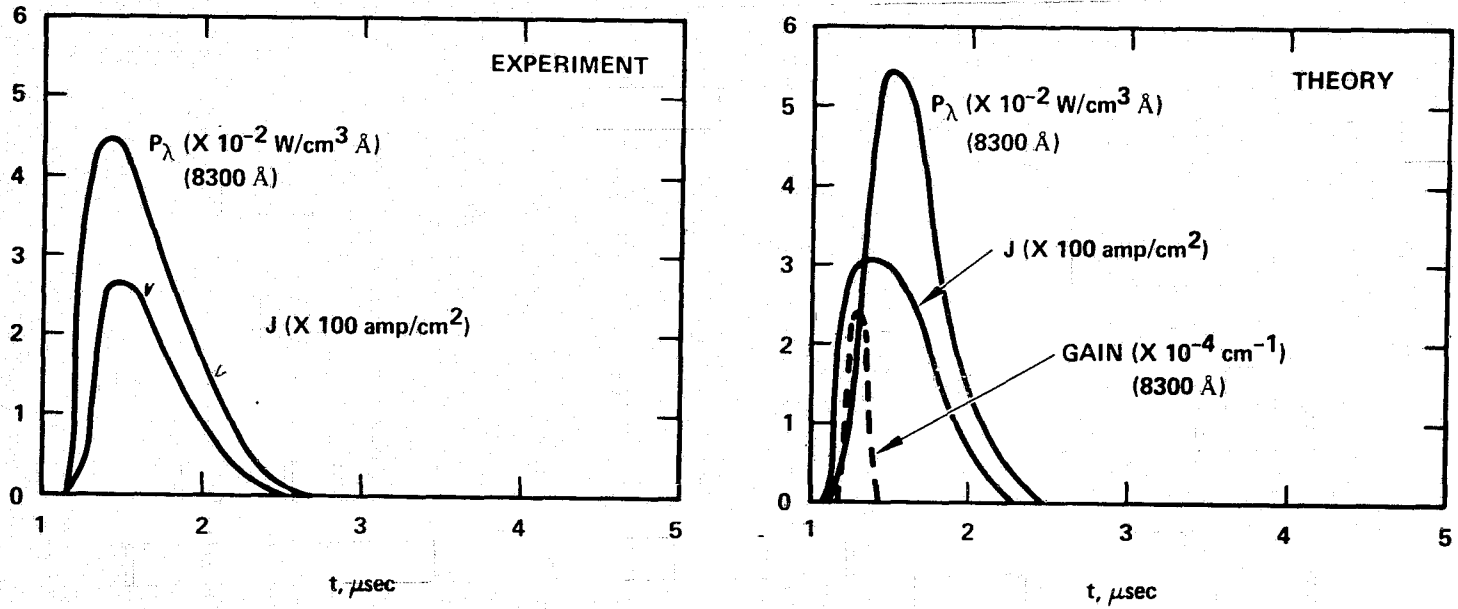


Figure 15. K Ar/K<sub>2</sub> capillary discharge: results.

$T = 350^\circ$   
 $[Ar] = 7 \times 10^{19} \text{ cm}^{-3}$   
 $V_c = 6 \text{ kV (1 cm DISCHARGE GAP)}$

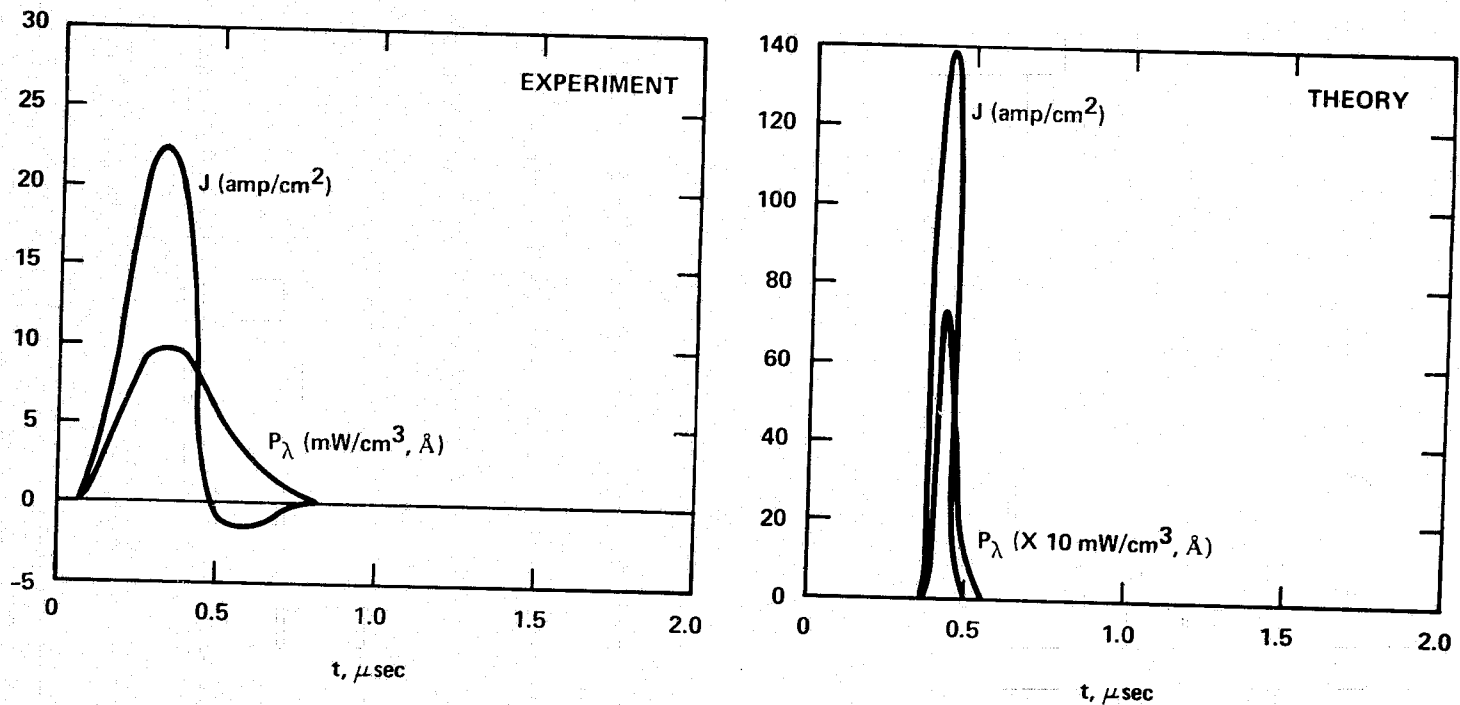


Figure 16.  $K \text{ Ar}/K_2$  transverse discharge: results.

Finally, the K Ar/K<sub>2</sub> theoretical model was used to predict the absorption coefficient in the unexcited K Ar/K<sub>2</sub> vapor so that experimental measurements of the absorption could provide a check that equilibrium vapor pressures were being attained. An example calculation of the absorption coefficient versus wavelength, compared with experiment, is shown in Figures 17 and 18 where the agreement is good. The experimental techniques used to obtain the absorption data are discussed in Section 7.

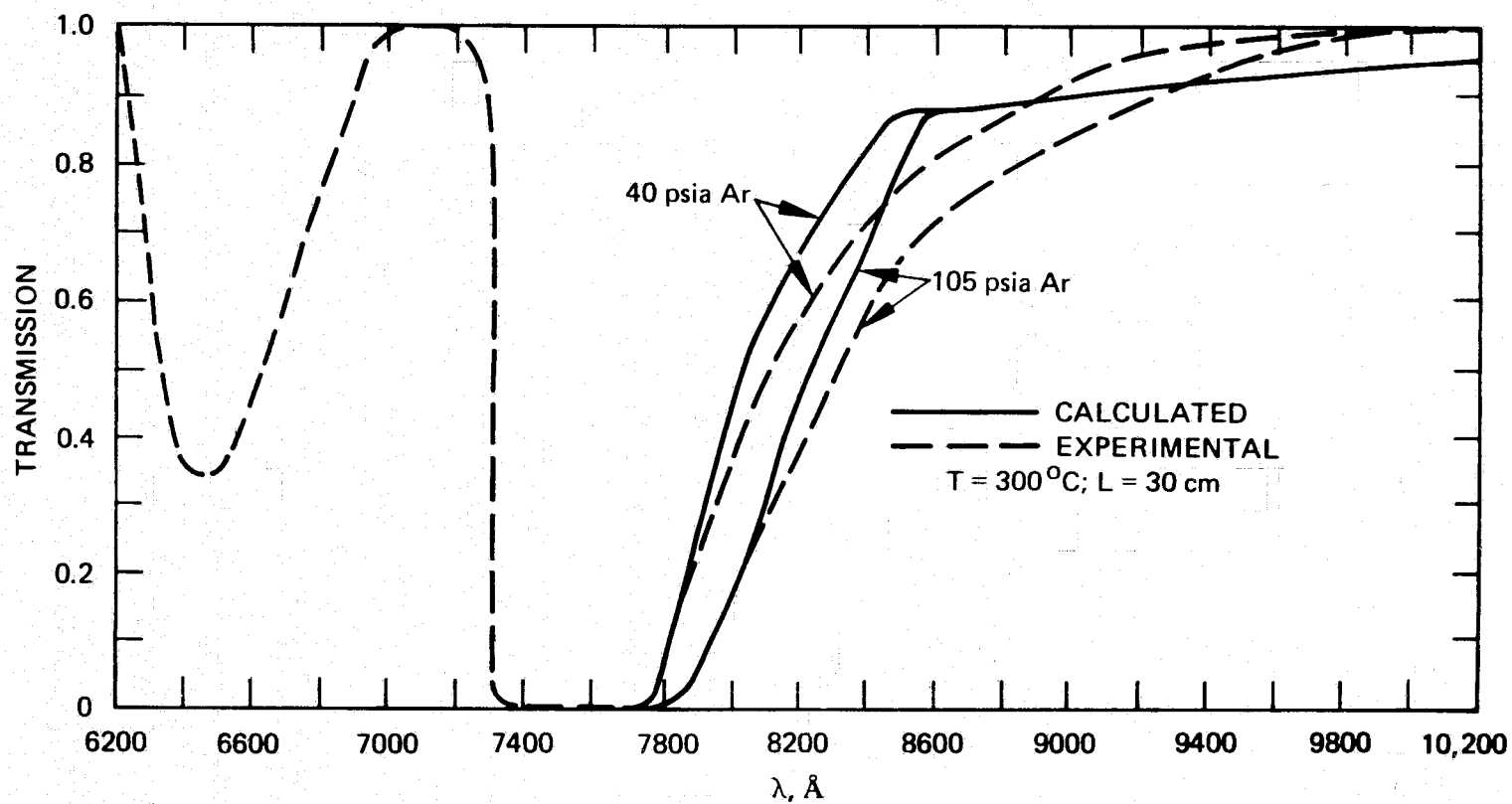


Figure 17. K Ar/K<sub>2</sub> transverse discharge system: absorption spectra.

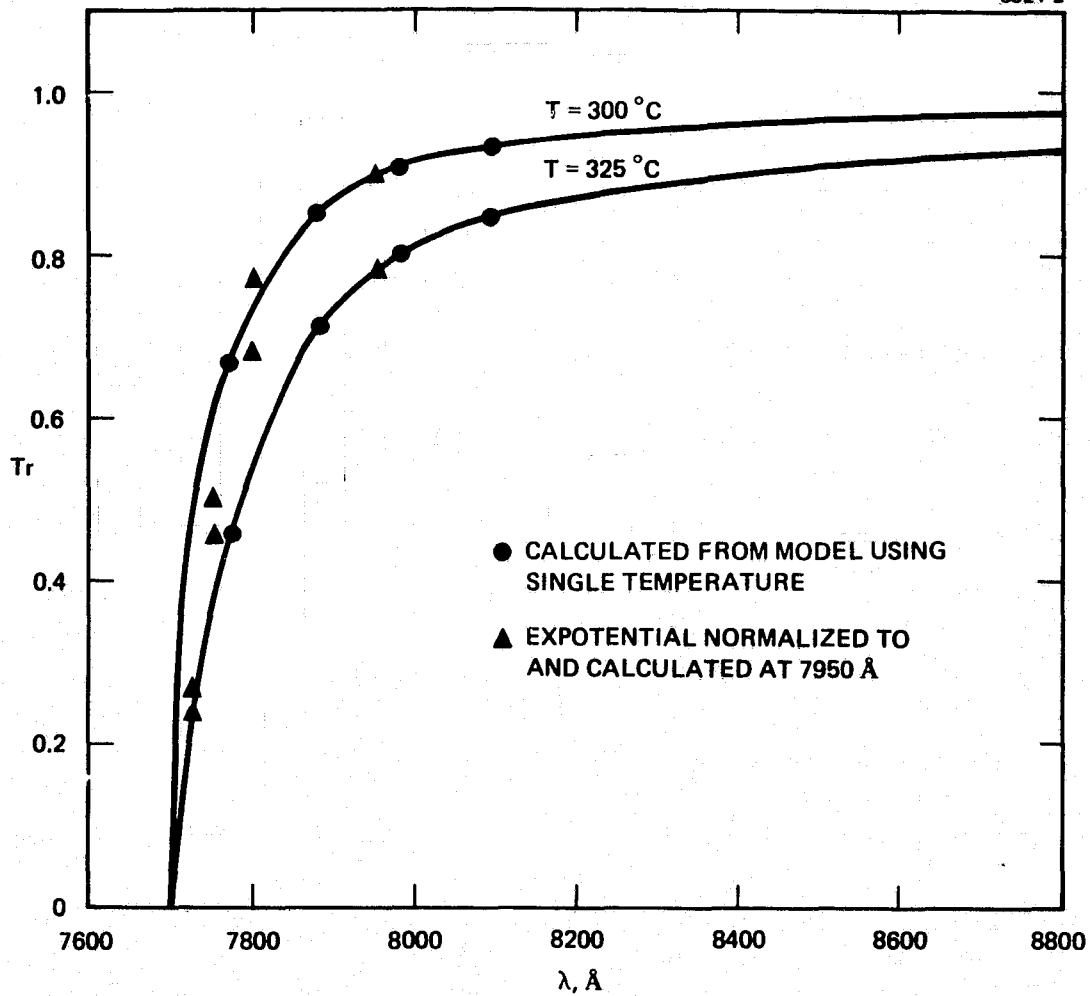


Figure 18. K Ar/K<sub>2</sub> capillary discharge system: absorption spectra.

ORIGINAL PAGE IS  
OF POOR QUALITY

## SECTION 6

### DISCHARGE EXPERIMENTS ON THE XeF EXCIMER SYSTEM

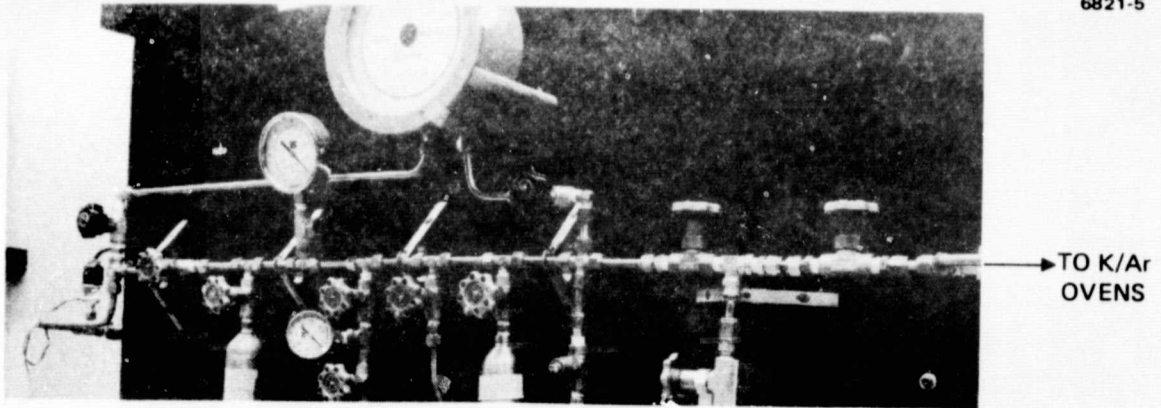
#### A. CAPILLARY DISCHARGE

##### 1. Apparatus

The rare-gas halides pose significant materials problems which must be considered in the design of the apparatus. Molecular fluorine is difficult to handle because it is one of the most powerful oxidizing agents known. The gas-handling apparatus shown in Figure 19 was designed and fabricated for use with the XeF laser system. This apparatus is constructed primarily of stainless steel tubing and incorporates stainless steel packless valves and fluorine compatible pressure gauges. The entire system was passivated with fluorine-helium mixtures and pure fluorine prior to use for discharge measurements. Nitrogen trifluoride ( $\text{NF}_3$ ) presents less of a materials problem and was used in this apparatus as a fluorine source for reaction with excited xenon atoms.

The discharge tube and electrical pulse circuit are shown photographically in Figure 19 and schematically in Figure 20. Stainless steel cylindrical cavity electrodes as shown in these figures were found to be more satisfactory than the simple tungsten pin electrodes that were used in our first XeF discharge experiments. The discharge tube was situated within an optical cavity as shown in Figure 19. Alignment of the optical cavity was achieved with the use of a He-Ne laser and conventional alignment techniques.

To evaluate discharge characteristics and laser potentialities, absolute fluorescence measurements were conducted with a variety of gas mixtures and electrical parameters. The optical configuration used for this purpose is shown schematically in Figure 21. A calibrated photodetector and optical filter were used to measure the side light emission from a well-defined volume in the discharge tube. These measurements can then be used to determine excited state populations



(a)

Figure 19. Rare-gas halide capillary discharge laser apparatus.

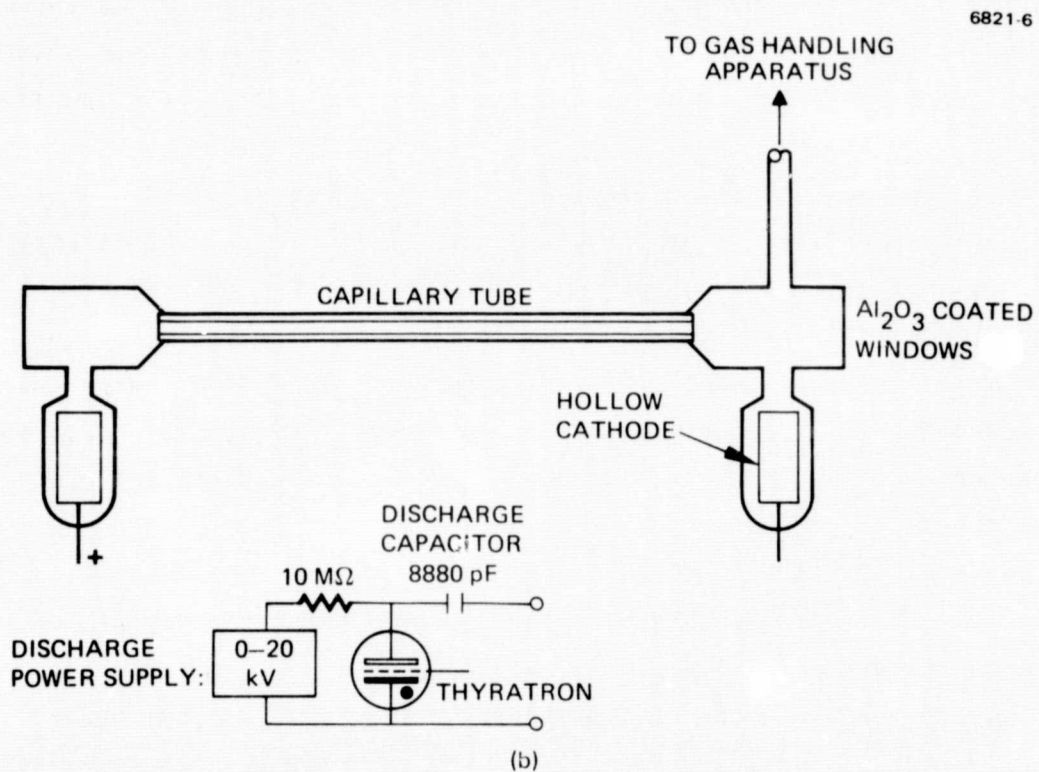


Figure 20. Schematic diagram of XeF capillary discharge tube and pulse circuit.

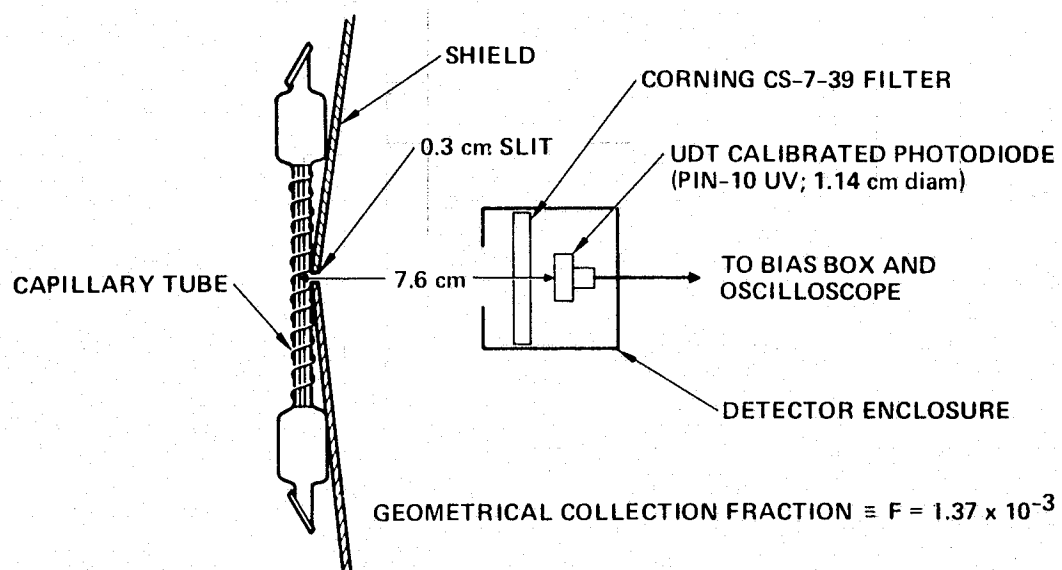


Figure 21. Experimental arrangement for absolute fluorescence measurements.

of XeF and the maximum optical gain coefficient,  $\alpha$ , with the assumption that the lower laser level is unoccupied. The relationships used to obtain this information are given below:

$$P_T = \frac{S_D}{FT} I_D$$

$$(XeF^*) = \frac{\lambda}{hcA} \frac{P_T}{V}$$

$$\alpha = \frac{\lambda_o^4 A}{4\pi^2 c \Delta\lambda} (XeF^*)$$

where

$P_T$  = total optical power emitted from volume, V

$I_D$  = photodetector current

F = geometrical collection fraction ( $1.37 \times 10^{-3}$ )

$S_D$  = detector sensitivity (10 W/A at 3450 Å)

T = average transmission of filter (0.464 from 340 Å to 3500 Å)

A = Einstein spontaneous emission coefficient ( $2.0 \times 10^7 \text{ sec}^{-1}$ )

$\Delta\lambda$  = full width at half maximum of XeF\* emission band (105 Å)

Use of the appropriate constants with the expression above shows that an upper state XeF concentration of  $3.76 \times 10^{13} \text{ cm}^{-3}$  is required to give a small-signal peak gain coefficient of  $1 \times 10^{-3} \text{ cm}^{-1}$ .

Spectral emission profiles were measured with a 1/4 m monochromator equipped with an optical multichannel analyzer detection system. The fluorescence spectrum of XeF obtained with this apparatus is shown in Figure 22. An  $NF_3$ :Xe:Ar = 1:1:10 mixture at a total pressure of 30 Torr was used in the quartz capillary discharge tube to obtain these data.

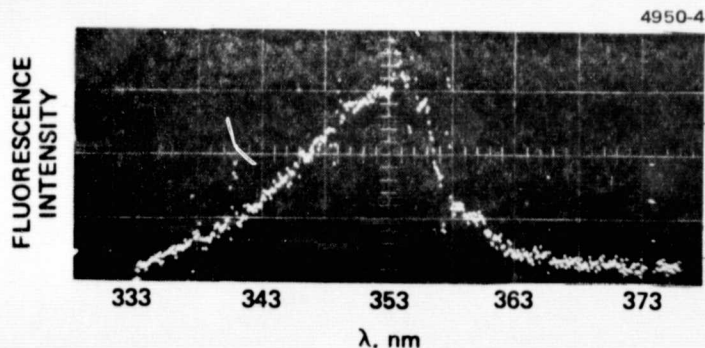


Figure 22. Spectral profile of XeF excimer fluorescence from capillary discharge tube.

## 2. Experimental Results

Data obtained from the XeF apparatus included discharge voltage, discharge current, and absolute fluorescence intensity measured as a function of gas mixture, pressure, and external circuit parameters (e.g., capacitor and ballast resistor size). Upper-state XeF\* populations and small-signal gain were calculated from the fluorescence data according to the procedures outlined in Section 6.A.1.

Experiments were performed with two different size capillaries: (1) a 15-cm-long x 0.3-cm-diameter tube, and (2) a 1.6-cm-long by 0.1-cm-diameter tube. Tube 1 was used in the initial experiments and was designed to provide a gain path long enough for laser action and a bore size large enough to permit easy mirror alignment. Tube 2 was used in the second phase of the experiment primarily to obtain a better understanding of the system kinetics. This tube was designed to provide more efficient gas cooling and higher E/P than tube 1.

Several unsuccessful attempts at pulsed laser action were made with tube 1 under conditions where the fluorescence measurements indicated peak gains of  $8 \times 10^{-3} \text{ cm}^{-1}$ . The modeling studies indicated that the gas temperature was too high and E/P too low to produce an inversion. The high fluorescence yields observed were apparently dominated by thermal excitation.

Tube 2 was then used to obtain additional data under more favorable operating conditions (lower temperature, higher E/P) which were then used as input to the modeling study. The pulsed and cw performance of tube 2 was not significantly better than tube 1. Pulsed gains were typically  $0.8 \times 10^{-3} \text{ cm}^{-1}$  for  $\sim 2 \mu\text{sec}$  durations. Continuous-wave gains were typically  $1 \times 10^{-5} \text{ cm}^{-1}$  and limited in duration only by the thyatron turnoff characteristics and fluorine consumption as discussed in Section 4.A.

### 3. Experiments With Tube 1

The initial experiments with tube 1, the 15-cm-long x 0.3-cm-i.d. tube, were carried out with a 50-to-200 k $\Omega$  resistor in series with the discharge capacitor to investigate the quasi-cw behavior of the system. Later experiments were performed with  $R = 0$  to examine the short pulse behavior. A summary of the experimental conditions and main results of these studies is shown in Table 6.

#### a. Quasi-CW Experiments With Tube 1

Both He and Ar were tried as diluents and  $\text{NF}_3$  was employed as the fluorine source. The He mixtures typically exhibited slightly better ( $\sim 20\%$ ) fluorescence intensities than comparable Ar mixtures. A typical mixture ratio used in these experiments was 1:1:2/ $\text{NF}_3$ -Xe-He. Uniform quasi-cw discharges of 100  $\mu\text{sec}$  duration could be readily obtained at total pressures  $\sim 10$  Torr, at current densities of 1 to 10  $\text{A}/\text{cm}^2$ , and E/P values of  $\sim 100 \text{ V}/\text{cm Torr}$ . At pressures higher than  $\sim 10$  Torr, the discharge would detach from the capillary wall and run a twisting course through the tube. The fluorescence intensity would be decreased by a factor of  $\sim 2$  when in this mode.

Typical data appear in Figure 23. Fluorescence intensity, total discharge current, and total anode-cathode voltage drop are shown. After 15 to 20  $\mu\text{sec}$  of fluctuations, the discharge reaches a steady-state operating mode at  $\sim 1 \text{ A}/\text{cm}^2$  and  $\sim 120 \text{ V}/\text{cm-Torr}$ . The steady-state  $\text{XeF}^*$  population is  $\sim 3.8 \times 10^{11} \text{ cm}^{-3}$  corresponding to a gain of  $\sim 10^{-5} \text{ cm}^{-1}$ . Gain of this magnitude is too small for laser action in tube 1.

Table 6. Operating Conditions and Main Results of  
15-cm-Long x 0.3-cm-i.d. Tube Experiments

Mixtures	$\text{NF}_3:\text{Xe}:\text{He} = 0.1 - 1.5: 1 - 3: 1.67 - 10$ $\text{NF}_3:\text{Xe}:\text{Ar} = 1 - 1.5: 1 - 3: 10$ $\text{NF}_3:\text{Xe} = 1: 4 - 9$
Pressures	0.5 - 10 Torr
Apparatus	C = 260 and 780 pF R = 0 to 200 K $\Omega$ 20.0 kV charging voltage
Long Pulse Experiments	$\text{XeF}^*$ of order $10^{11} - 10^{12} \text{ cm}^{-3}$ ( $\alpha \sim 10^{-5} \text{ cm}^{-1}$ ) Fluorescence Pulses $\sim 50 + \mu\text{sec}$ long Current Densities $J \sim 1 - 10 \text{ A cm}^2$ Steady State E/P $\sim 100 \text{ V/cm - Torr}$
Short Pulse Experiments (R=0)	$\text{XeF}^*$ Peak Values of $1 \text{ to } 3 \times 10^{14} \text{ cm}^{-3}$ Apparent Gains of $\alpha = 2.6 - 8.0 \times 10^{-3} \text{ cm}^{-1}$ Fluorescence Pulses $\sim 0.5 \mu\text{sec}$ long Current Pulses $\sim 0.2 \mu\text{sec}$ long, $J = 100 \text{ to } 4000 \text{ A cm}^2$ E/P Low (Unmeasured) Laser Action Tried With 1 to 4/ $\text{NF}_3 - \text{Xe}$ Mixture Attempt Unsuccessful Because of Gas Heating

T1938

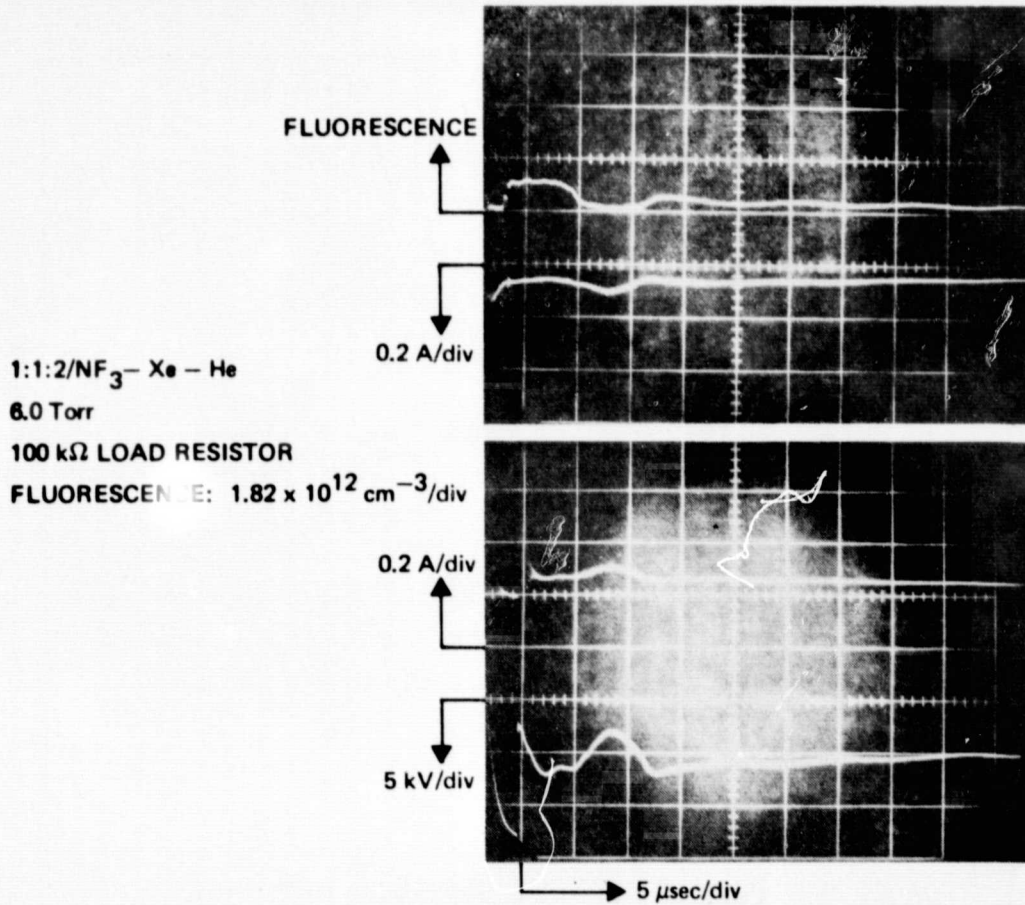


Figure 23. Quasi-cw operation of a typical NF<sub>3</sub> mixture in the 3-mm tube.

b. Short Pulse Experiments with Tube 1

(1) Fluorescence Optimization — As the ballast resistor (R) is decreased the current pulse shortens, the initial current rises, and the fluorescence changes from a quasi-cw to a pulsed character. The peak fluorescence increases with increasing current to the point where  $R = 0$  and the current is limited primarily by the circuit inductance. The increase in fluorescence obtained by going from  $R = 100$  or  $200 \text{ k}\Omega$  to  $R = 0$  was typically a factor of  $\sim 200$ .

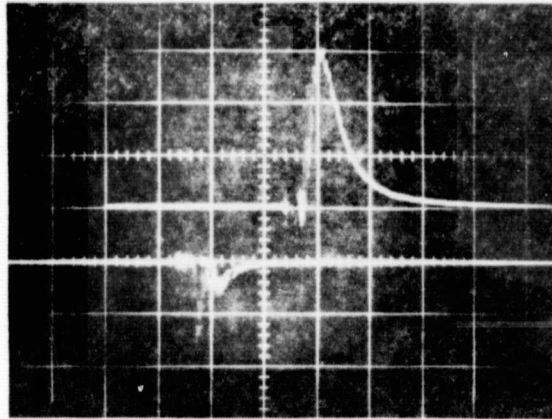
Further increases in the fluorescence intensity were obtained by varying the mixture ratio and gas pressure. It was found that the fluorescence increased with increasing  $\text{NF}_3$  and decreasing He diluent. Ultimately, conditions were found where peak  $\text{XeF}^*$  populations of  $3 \times 10^{14} \text{ cm}^{-3}$  and gains of  $8 \times 10^{-3} \text{ cm}^{-1}$  were observed. This corresponds to a single-pass gain of 12% in our 15-cm tube.

Figure 24 shows fluorescence and current traces for this maximum gain condition in the 3-mm tube. The fluorescence from this 1:4/ $\text{HF}_3$ -Xe mixture at 7 Torr has an FWHM of  $\sim 300$  nsec. The current pulse is also  $\sim 300$  nsec wide and reaches a peak value of  $\sim 700 \text{ A/cm}^2$ . The discharge voltage was unmeasurable because of noise, but the E/P was probably  $\sim 50 \text{ V/cm-Torr}$ . In Figure 24 the fluorescence trace is displaced two divisions to the right, relative to the current trace.

(2) Laser Action Experiments — Laser action was attempted with this 1:4/ $\text{NF}_3$ -Xe mixture at pressures of 1 to 10 Torr. The optical cavity consisted of two 50-cm radius mirrors spaced 40 cm apart. The mirrors were made of quartz and coated with multilayer dielectric films to give high reflectivity and 0.1% transmission near  $3500 \text{ \AA}$ . This stable cavity was carefully aligned with an external He-Ne beam. A photomultiplier equipped with a narrow band  $3500 \text{ \AA}$  filter was placed  $\sim 40$  cm from the output window in the output beam path. The apparatus was carefully apertured so that the phototube saw only the light emitted through the output mirror. The detector system was sensitive enough to easily see the nonlasing  $\text{XeF}^*$  spontaneous emission obtained when the rear laser mirror was blocked.

The onset of laser action with the above system would have been observable as a drastic (several orders of magnitude) change in the photomultiplier signal level. By comparing the detector signals obtained with the rear laser mirror blocked and unblocked, even extremely weak lasing action should have been observable.

No change in the phototube signal was observed despite pressure and current variations as well as mirror excursions performed about the He-Ne alignment condition. Laser action with a 1.5:3.0:10/ $\text{NF}_3$ -Xe-He mixture was also tried with a similar lack of success.



1 - 4/NF<sub>3</sub> - Xe      7.0 Torr

780 pF AT 20 kV

NO DISCHARGE RESISTOR

TIME: 0.5 μsec/div

FLUORESCENCE (TOP):  $1.03 \times 10^{14}$  XeF\* cm<sup>-3</sup>/div  
 $\text{XeF}^* \text{ PEAK} = 3.0 \times 10^{14}$  cm<sup>-3</sup>  
 $\alpha \text{ PEAK} = 8 \times 10^{-3}$  cm<sup>-1</sup>

CURRENT (BOTTOM): 100 A/div

$I_{\text{PEAK}} \cong 700$  A/cm<sup>2</sup>

Figure 24. Optimized fluorescence for 3-mm tube experiments.

The lack of laser action is probably due to a high gas temperature and low E/P brought on by the high current densities required to give apparent gains of practical magnitude. The high fluorescence yield is not caused by selective excitation of XeF\*, but instead is the result of thermal pumping which also populates the XeF ground state.

(3) Experiments With the 1.6-cm-Long x 0.1-cm-i.d. Tube (Tube 2) - Quasi-cw, as well as short pulse operation, was also examined in the 1-mm tube. Current densities were usually kept below 50 to 75 A/cm<sup>2</sup> to prevent significant gas heating. A summary of the experimental conditions and main results of the 1 mm tube studies are shown in Table 7.

Table 7. Operating Conditions and Main Results of  
1.6-cm-long x 0.1-cm-i.d. Tube Experiments

<b>Mixtures</b>	$\text{NF}_3:\text{Xe}:\text{He} = 0.1 \text{ to } 1:1:1 - 2$ $\text{F}_2:\text{Xe}:\text{He} = 0.2:1:1$
<b>Pressures</b>	0.5 – 40 Torr
<b>Apparatus</b>	C = 260 and 780 pF R = 5 to 500 K $\Omega$ 20 kV Charging Voltage
<b>Long Pulse Experiments</b>	
	Steady State $\text{XeF}^*$ of $2 - 4 \times 10^{11} \text{ cm}^{-3}$ Observed for 0.5 msec Durations in $\text{NF}_3$ and $\text{F}_2$ Mixtures
	Steady State Gains = $0.5 \times 10^{-5} - 1.0 \times 10^{-5} \text{ cm}^{-1}$
	$J \cong 1 - 5 \text{ A cm}^2$
	$E/P \cong 60 \text{ to } 250 \text{ V/cm - Torr}$
<b>Short Pulse Experiments (R &gt; 5 K<math>\Omega</math>)</b>	
	Peak $\text{XeF}^*$ of $\sim 3 \times 10^{13} \text{ cm}^{-3}$ ( $\alpha \sim 0.8 \times 10^{-3} \text{ cm}^{-1}$ )
	Fluorescence Pulses 1 to 20 $\mu\text{sec}$ Long
	$J \cong 5 - 50 \text{ A cm}^2$
	Discharge Runs at High E/P (400 to 700 V/cm – Torr) for $\sim 5 \mu\text{sec}$ at Start
	Discharge Then Makes Transition to Lower E/P (80 to 300 V/cm – Torr)
	Maximum Fluorescence Occurs During High E/P Initial Phase

T1939

c. Quasi-CW Experiments With Tube 2

(1) Measurements on  $\text{NF}_3$  and  $\text{F}_2$  Mixtures — The first experiments with the smaller tube were directed toward quasi-cw operation. Both  $\text{F}_2$  and  $\text{NF}_3$  were used as fluorine sources and He was used as a diluent. A typical mixture investigated was 0.2:1:1/ $\text{NF}_3(\text{F}_2)$ -Xe-He. Data for this mixture are shown in Figure 25 (with  $\text{NF}_3$ ) and Figure 26 (with  $\text{F}_2$ ). Total anode-cathode voltage drop,  $\text{XeF}^*$  fluorescence intensity and total discharge current are shown as functions of total pressure. Operating pressures were usually limited to below 30 to 40 Torr by the discharge not breaking down.

The  $\text{NF}_3$  data (Figure 25) show that after an initial 50 to 100  $\mu\text{sec}$  high fluorescence period with  $\text{XeF}^* \cong 1.5 \times 10^{12} \text{ cm}^{-3}$ , the discharge voltage and current reach a steady state and produce a quasi-cw  $\text{XeF}^*$  population for  $\sim 0.5$  msec. The termination of the fluorescence is caused by the turnoff of the thyatron, not by kinetics effects. Rough calculations indicate that the fluorescence could remain at these levels for several milliseconds before  $\text{NF}_3$  consumption effects become significant.

The steady-state fluorescence scales approximately linearly as the total pressure from a value of  $1.2 \times 10^{11} \text{ cm}^{-3}$  at 7.5 Torr to  $3.7 \times 10^{11} \text{ cm}^{-3}$  at 23 Torr. The corresponding quasi-cw gains are  $0.3 \times 10^{-5} \text{ cm}^{-1}$  and  $1.0 \times 10^{-5} \text{ cm}^{-1}$ , respectively. Steady-state E/P falls from 250 V/cm-Torr at 7.5 Torr to 135 V/cm-Torr at 23 Torr. Current densities are about  $2 \text{ A/cm}^2$  for all three cases shown.

It should be noted that the current does not decay as fast as is indicated in Figure 25. About half of the decay is caused by the 0.06%/ $\mu\text{sec}$  droop (36% in 600  $\mu\text{sec}$ ) of the Pearson 2100 Rogowski coil used in these measurements. This spurious decay is evident at the end of the discharge where the current trace undershoots the baseline.

The  $\text{F}_2$  data (Figure 26) shows similar time and pressure variations. After an initial transient, a 0.5 to 0.7 msec quasi-cw fluorescence level is observed during a period of nearly constant discharge current and voltage. The steady-state fluorescence again scales approximately linearly with pressure from  $1 \times 10^{11} \text{ cm}^{-3}$  at 15 Torr ( $0.27 \times 10^{-5} \text{ cm}^{-1}$

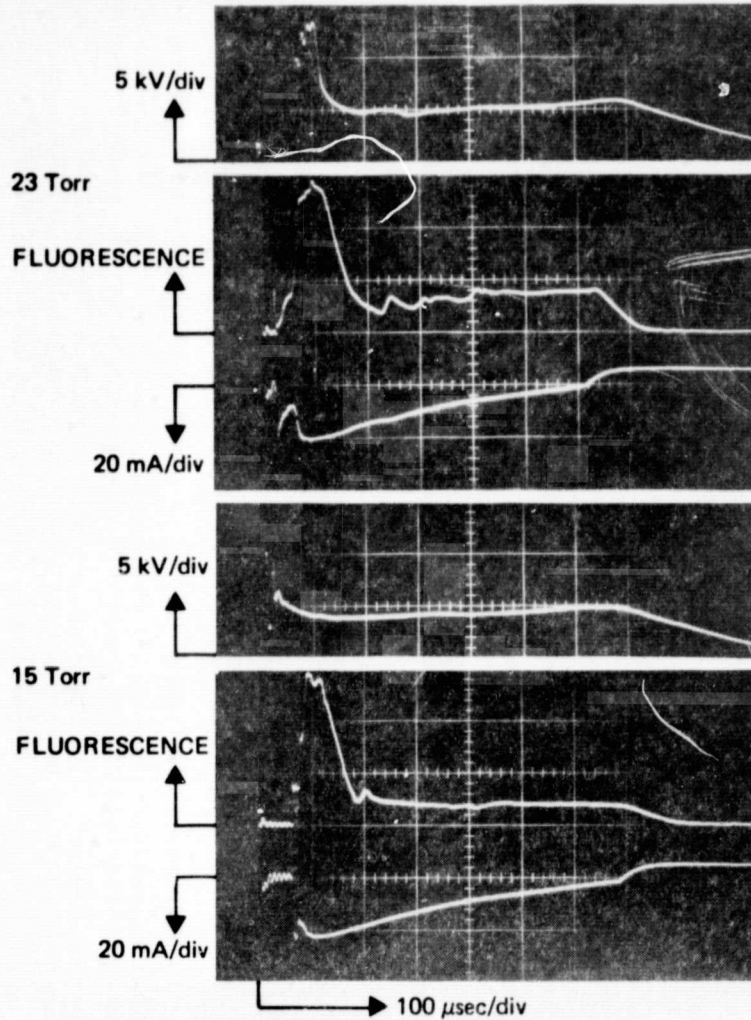
0.2:1:1/NF<sub>3</sub> - Xe - HeFLUORESCENCE =  $4.71 \times 10^{11} \text{ cm}^{-3}/\text{div}$ 

Figure 25. Quasi-cw operation in typical NF<sub>3</sub> mixture.

ORIGINAL PAGE IS  
OF POOR QUALITY

0.2:1:1/NF<sub>3</sub> - Xe - He

FLUORESCENCE:  $4.71 \times 10^{11} \text{ cm}^{-3}/\text{div}$

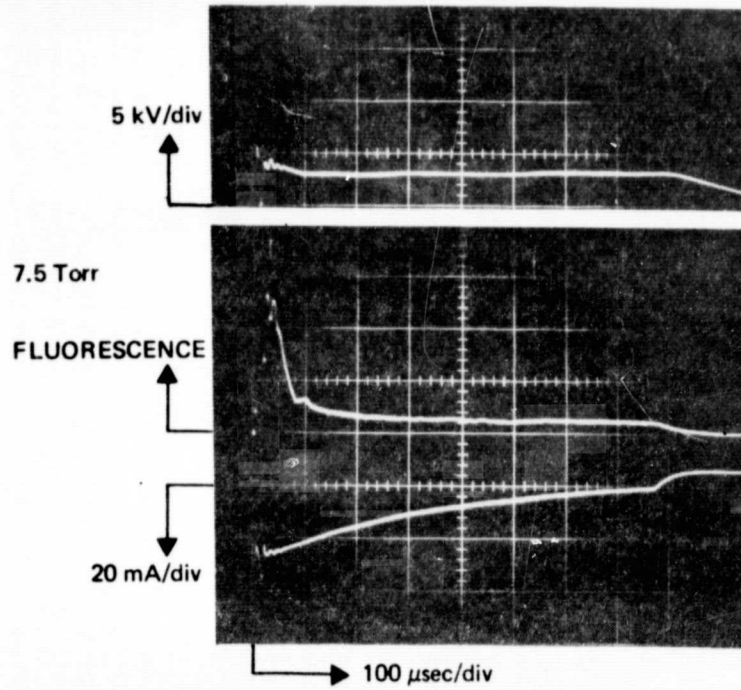


Figure 25. Continued.

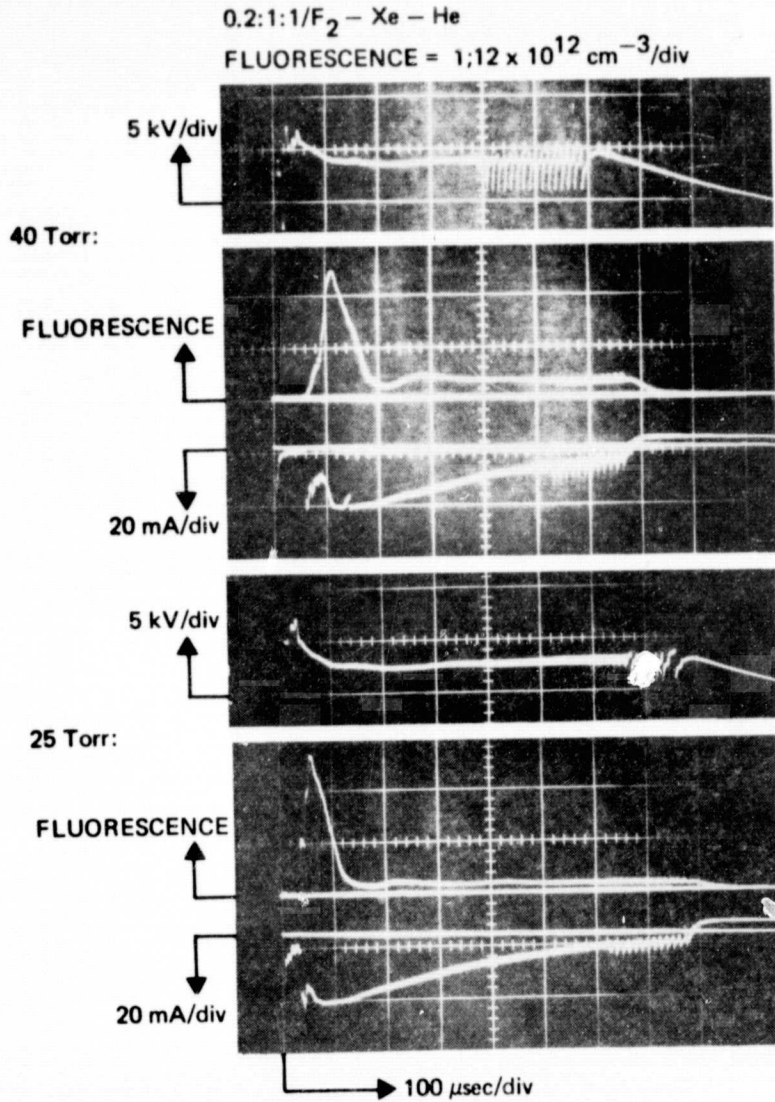


Figure 26. Quasi-cw operation in typical F<sub>2</sub> mixture.

ORIGINAL PAGE IS  
OF POOR QUALITY

0.2:1:1/F<sub>2</sub> - Xe - He

FLUORESCENCE =  $1.12 \times 10^{12} \text{ cm}^{-3}/\text{div}$

5117-47

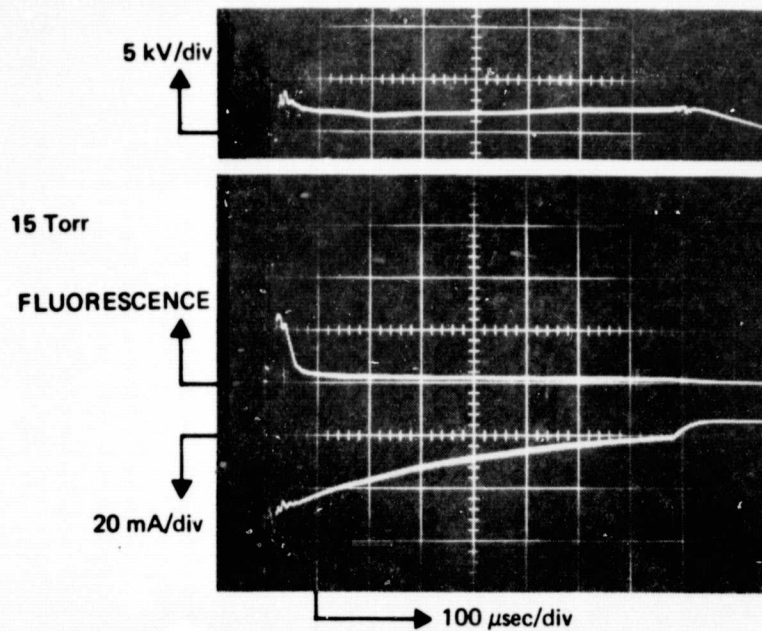


Figure 26. Continued.

gain). The mixtures containing  $F_2$  thus produce about one-half as much fluorescence as corresponding ones containing  $NF_3$ . This may be a result of the visually poorer discharge uniformity obtained with the  $F_2$  mixtures. Whereas the  $NF_3$  mixtures were uniform across the entire tube bore, the  $F_2$  mixtures were noticeably brighter at the tube center than they were near the tube wall. The steady-state E/P was also lower in the  $F_2$  mixtures, decreasing from 80 V/cm-Torr at 15 Torr to 60 V/cm-Torr at 40 Torr.

(2) Fluorine Atom Recombination Experiment - A significant factor limiting cw operation is consumption of the fluorine source by the reaction  $Xe^* + F_2(NF_3) \rightarrow XeF^* + F(NF_2)$ . One way to avoid this problem is to add a large amount of diluent to the mixture to enhance the three-body recombination reaction  $F + F + He \rightarrow F_2 + He$ . To see if this recombination reaction would have any effect upon the fluorescence level observed during quasi-cw operation, a 0.2:1:40/ $F_2$ -Xe-He mixture was studied at pressures up to 200 Torr. A 0.2:1:40 mixture at 200 Torr has the same  $F_2$  and Xe concentrations as a 10.7 Torr 0.2:1:1 mixture, but 40 times more He to act as a third body.

Figure 27 shows the 200 Torr operation of this mixture. The gas broke down easily, but the discharge was filamentary in nature with only about one-half of the bore filled with a bright discharge directly down the tube center. The nonuniformity in the case was much worse than in the previous 0.2:1:1 mixture. As before, the discharge lasted for  $\sim 0.7$  msec at constant voltage and approximately constant current until the thyratron shut off. E/P was 6.25 V/cm-Torr (258 V/cm-Torr Xe), and assuming that the current and  $XeF^*$  population were uniformly distributed throughout the tube, these had values of  $2.5 \text{ A/cm}^2$  and  $2.35 \times 10^{11} \text{ cm}^{-3}$ , respectively.

This  $XeF^*$  population is about a factor of two greater than that observed in 0.2:1:1 mixtures at 10 to 15 Torr, indicating that the added He may be having a positive effect. However, the filamentary nature of the discharge makes these results suspect. The "filament" could be an "arc" with a high current density and a thermally excited population, similar to the high current experiments with the 3-mm tube.

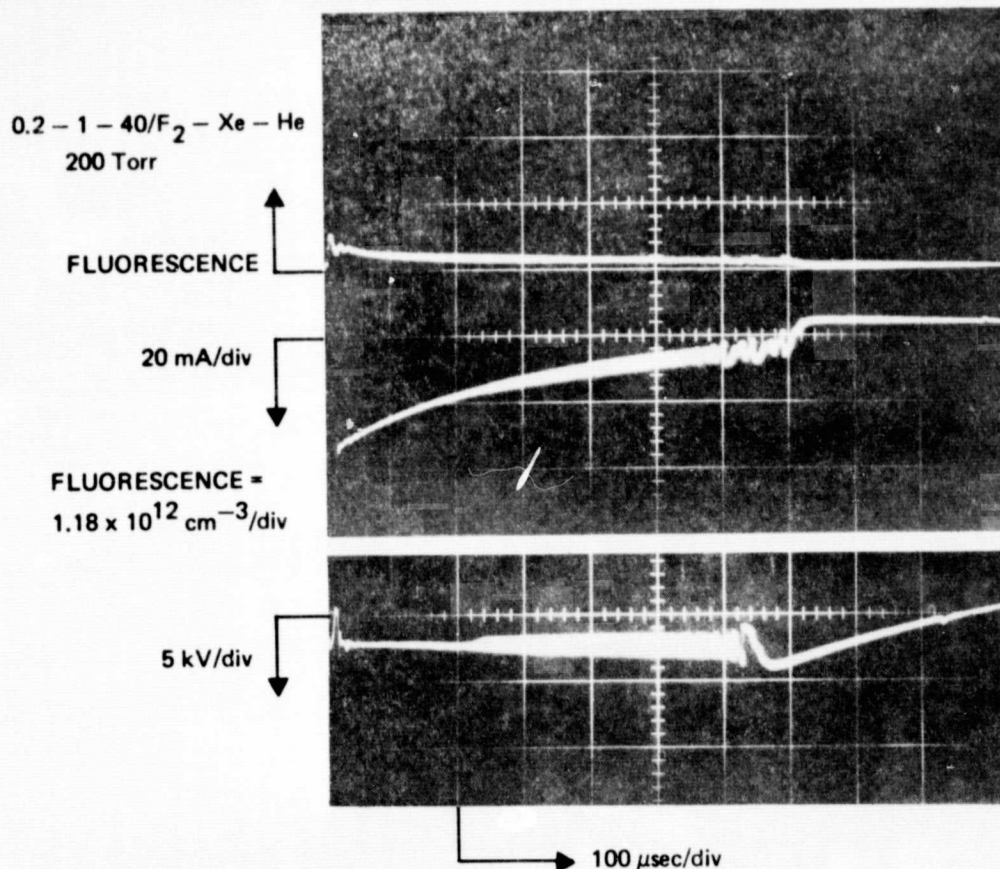


Figure 27. Operation at 200 Torr with high helium concentration.

Further studies are required before a definite conclusion can be made on the efficacy of the recombination approach.

d. Short Pulse Experiments with Tube 2

(1) Current Density Limitations - As the current is increased in the 1-mm tube (tube 2), the initial fluorescence intensity also increases. The current cannot be increased indefinitely, however, since eventually gas heating becomes excessive and any hope of obtaining a XeF inversion is destroyed by a lowered E/P and thermal filling of the XeF ground state. We therefore conducted several experiments

in an effort to determine an upper limit on the current density below which high E/P and good XeF\* fluorescence could be obtained simultaneously. This limit is  $\sim 50$  to  $75 \text{ A/cm}^2$  for the mixtures studied.

At current densities below this limit, high E/P is observed for  $\sim 5 \text{ } \mu\text{sec}$  at the beginning of the current pulse. After this initial high E/P phase, the discharge then makes a transition to lower E/P and continues to operate there until the thyatron shuts off. The high E/P phase is characterized by E/Ps in the range 400 to 700 V/cm-Torr, while 80 to 300 V/cm-Torr is typically observed during the low E/P phase. The maximum XeF\* fluorescence is observed during the low E/P phase. The maximum XeF\* fluorescence is observed during the high E/P phase. The exact values of E/P obtained depend upon mixture ratio and pressure. E/P generally increases with decreasing pressure and increasing  $\text{NF}_3(\text{F}_2)$ .

This dual mode of operation is illustrated in Figures 28(a), (b), and (c). These figures show discharge voltage and current for decreasing values of the ballast resistor. An initial  $\sim 5 \text{ } \mu\text{sec}$  voltage hump (the high E/P phase) is followed by a relatively flat voltage trace (the low E/P phase). Despite the fact that the current density varies from  $\sim 10 \text{ A/cm}^2$  in Figure 28(a) to  $\sim 40 \text{ A/cm}^2$  in Figure 28(c), all three cases exhibit E/Ps of  $\sim 400 \text{ V/cm-Torr}$  during the first phase and  $\sim 125 \text{ V/cm-Torr}$  during the second.

This collapse of the initial high E/P is a result of consumption of  $\text{NF}_3(\text{F}_2)$ . Since this effect is proportional to current density, one would expect the high E/P phase to shorten drastically at high current densities. This, in fact, is observed. At current densities above  $50$  to  $75 \text{ A/cm}^2$  most mixtures exhibit a high E/P phase of only several hundred nanoseconds duration. This effect is illustrated in Figures 28(d) and 28(e), where initial current densities are  $\sim 150$  and  $\sim 350 \text{ A/cm}^2$ , respectively. The E/P in these mixtures falls almost immediately to low values of  $\sim 80 \text{ V/cm-Torr}$ . At current density of this level, excessive gas heating will also have a detrimental effect upon the XeF\* inversion.

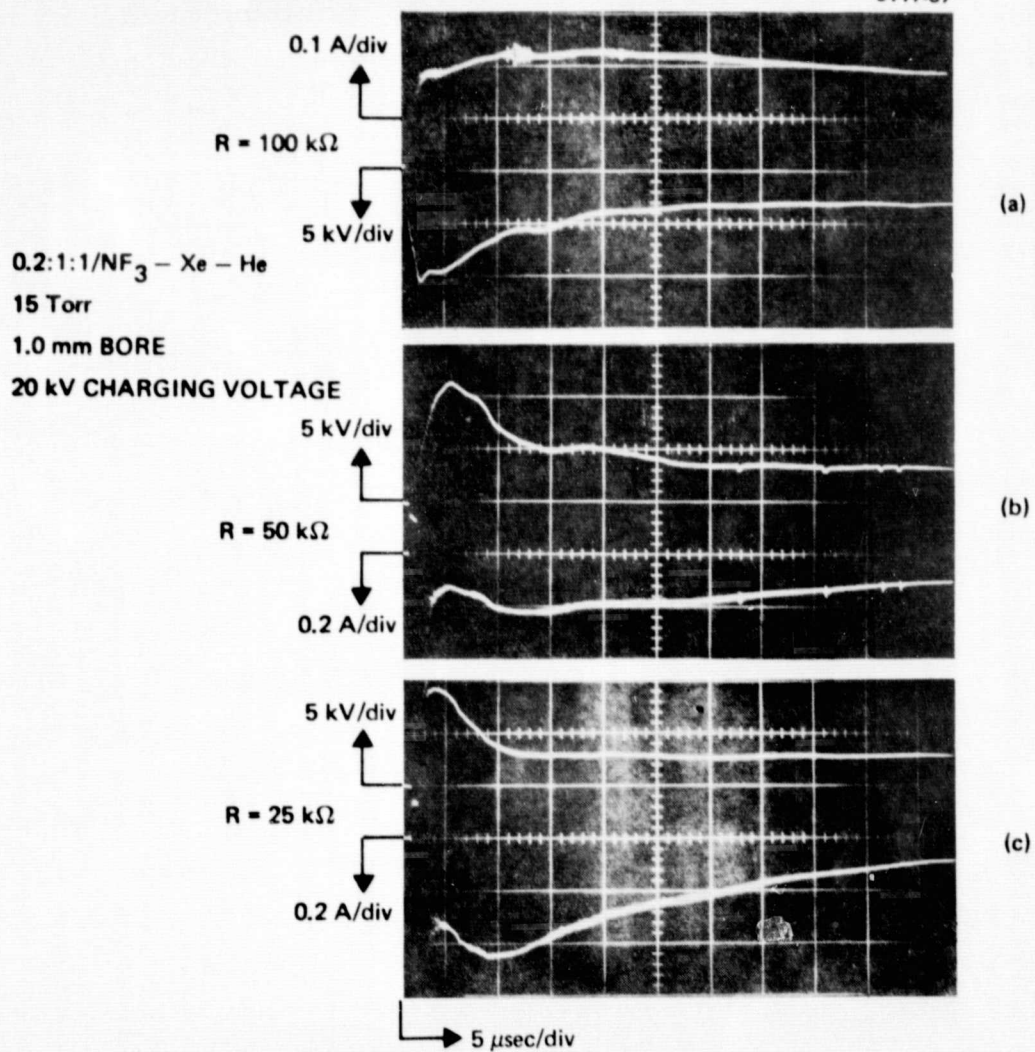


Figure 28. V-I data for NF<sub>3</sub> mixtures illustrating current density limit.

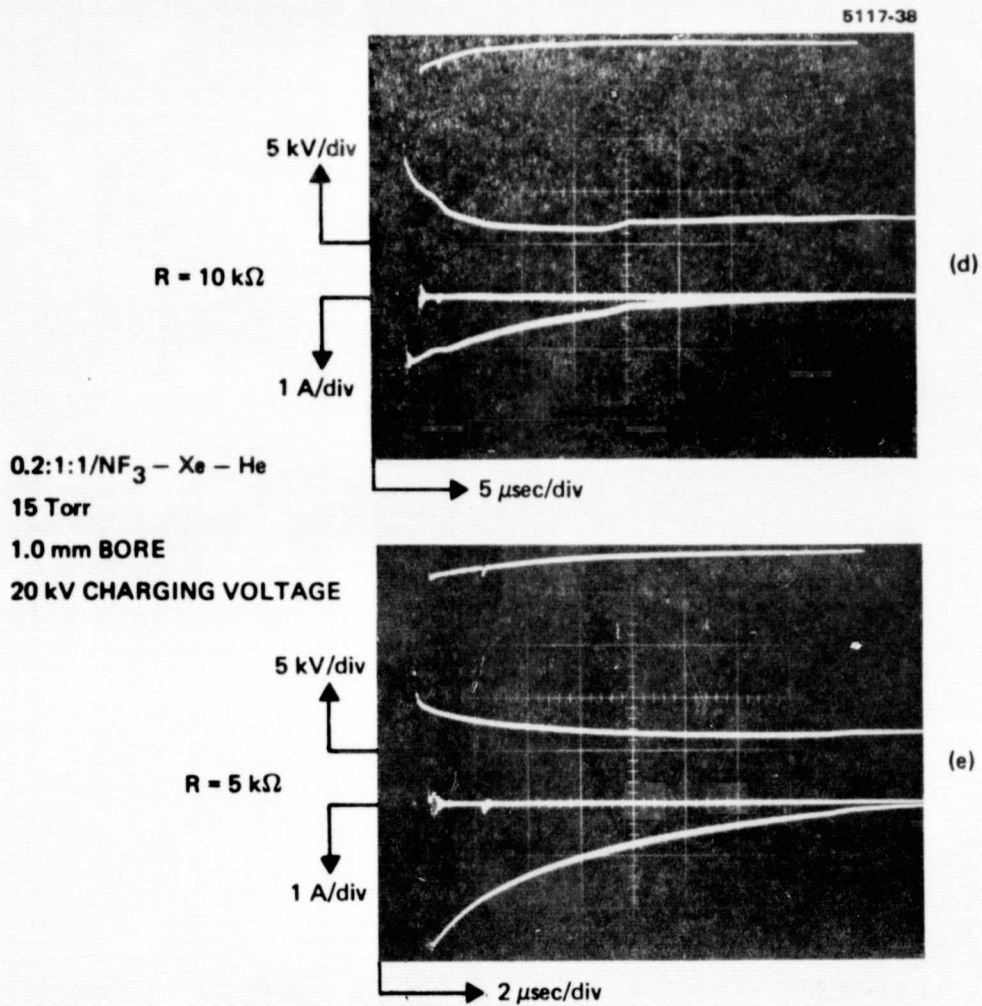


Figure 28. Continued.

(2) Discharge Stability — In Section 2 a stability condition was derived which indicated that the discharge will be stable as long as the voltage drop across the ballast resistor is greater than the voltage drop across the discharge. The data shown in Figure 29 support this stability condition.

This series of oscilloscope traces shown the V-I characteristic of a 0.2:1:1/NF<sub>3</sub>-Xe-He mixture as a function of pressure for a fixed charging voltage (20 kV) and fixed ballast resistor (50 kΩ). In Figures 29(a), (b), and (c), the peak discharge voltage is well over half of the total 20 kV on the discharge capacitor. It is 15 kV, 13 kV,

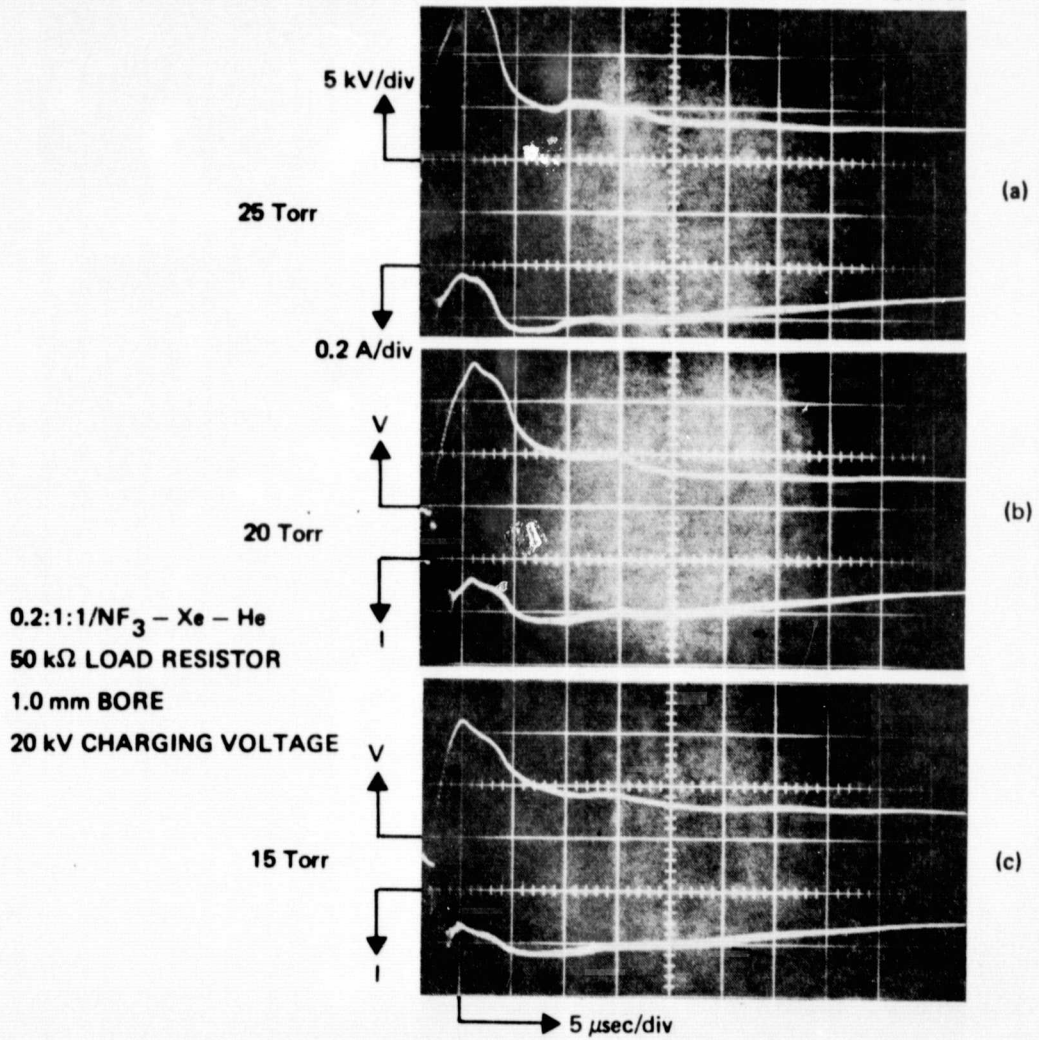


Figure 29. V-I data for NF<sub>3</sub> mixture illustrating the discharge stability condition.

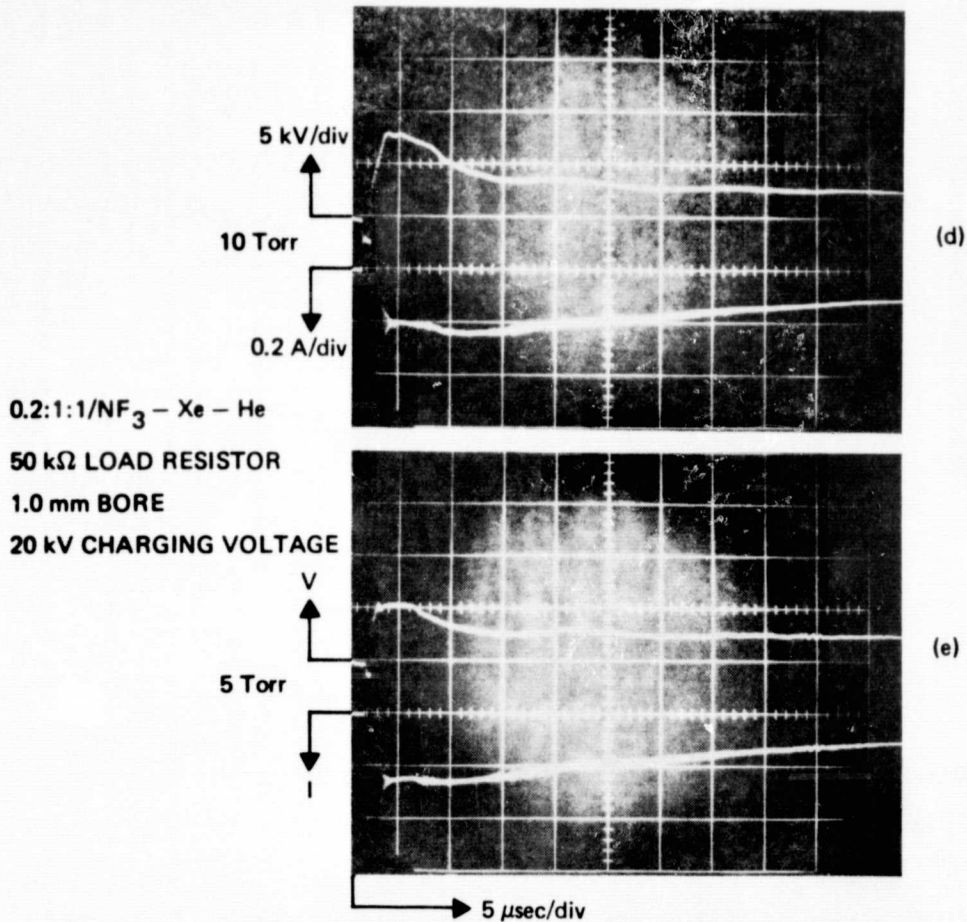


Figure 29. Continued.

and 11 kV in Figures 29(a), (b), and (c), respectively. The ballast resistor thus has  $\sim 5$  kV,  $\sim 7$  kV, and  $\sim 9$  kV across it in the corresponding cases. The discharge should be unstable, and indeed the discharge current does exhibit a factor of 2 type fluctuations in the first 10  $\mu$ sec of each trace.

In Figures 29(d) and (e), however, these fluctuations are absent. In these cases the peak discharge voltages are 8 and 5 kV corresponding to ballast resistor voltage drops of  $\sim 12$  and  $\sim 15$  kV. These voltages satisfy the stability criterion and indeed the V-I characteristics of

Figures 29(d) and (e) do come to a steady state more rapidly with less severe fluctuations than do cases of Figures 29(a), (b), and (c).

(3) Fluorescence Measurements - With the 50 to 75 A/cm<sup>2</sup> limit in mind, variations in system parameters were carried out to maximize the XeF\* fluorescence. The XeF\* population was a weak function of current density, pressure, and mixture ratio. Typically, the peak fluorescence would vary by only factors of 2 to 4 for fairly large excursions in operating conditions. The use of F<sub>2</sub> in place of NF<sub>3</sub> also produced only small differences in performance.

Figure 30 illustrates how the XeF\* fluorescence varies with pressure for a typical NF<sub>3</sub>-Xe-He mixture. The optimum pressure for this mixture is ~ 10 Torr where XeF\*  $\cong 3.3 \times 10^{13} \text{ cm}^{-3}$  (i.e., gain  $\cong 0.9 \times 10^{-3} \text{ cm}^{-1}$ ) is obtained. The fluorescence, which is significant only during the initial part of the current pulse (high E/P phase), varies by only about a factor of two over the range 5 to 20 Torr. The current density varies from ~ 25 A/cm<sup>2</sup> at 20 Torr to ~ 65 A/cm<sup>2</sup> at 5 Torr.

Figure 31 shows oscilloscope traces of the maximum fluorescence obtained for four different X:1:1/NF<sub>3</sub>-Xe-He mixtures with X = 0.2, 0.35, 0.5, and 1.0. These mixtures produced the highest fluorescence of any evaluated during this part of the study. In this series, the operating pressure has been varied with constant charging voltage (20 kV) and a fixed ballast resistor (25 k $\Omega$ ) until maximum fluorescence was obtained for each mixture.

Despite the wide variation in NF<sub>3</sub> concentration, the optimum fluorescence obtained is nearly the same for all mixtures: XeF\*  $\cong 3 \times 10^{13}$  corresponding to ~ 0.8  $\times 10^{-3} \text{ cm}^{-1}$  gain. As indicated previously, this lack of a strong dependence upon operating conditions appears to be a general characteristic of the XeF\* capillary system and is not restricted to this particular set of mixtures.

Figure 32 shows typical short pulse operation with F<sub>2</sub> at two different current levels 15 A/cm<sup>2</sup> (top) and 30 A/cm<sup>2</sup> (bottom). Despite these relatively modest current densities, the discharge does not exhibit the initial high E/P phase observed in NF<sub>3</sub> discharges. Maximum

5117-43

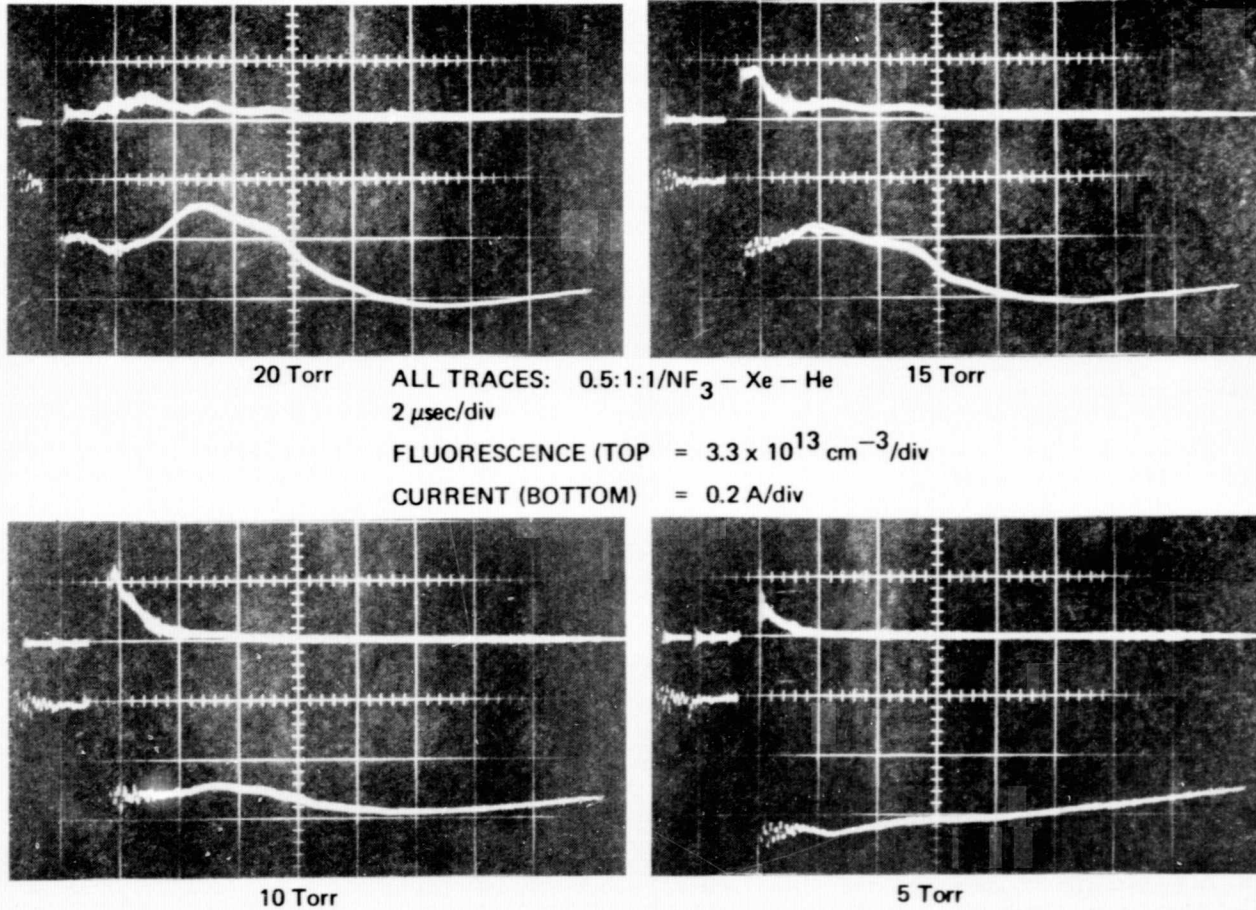


Figure 30. Pressure dependence of fluorescence from a typical NF<sub>3</sub> mixture.

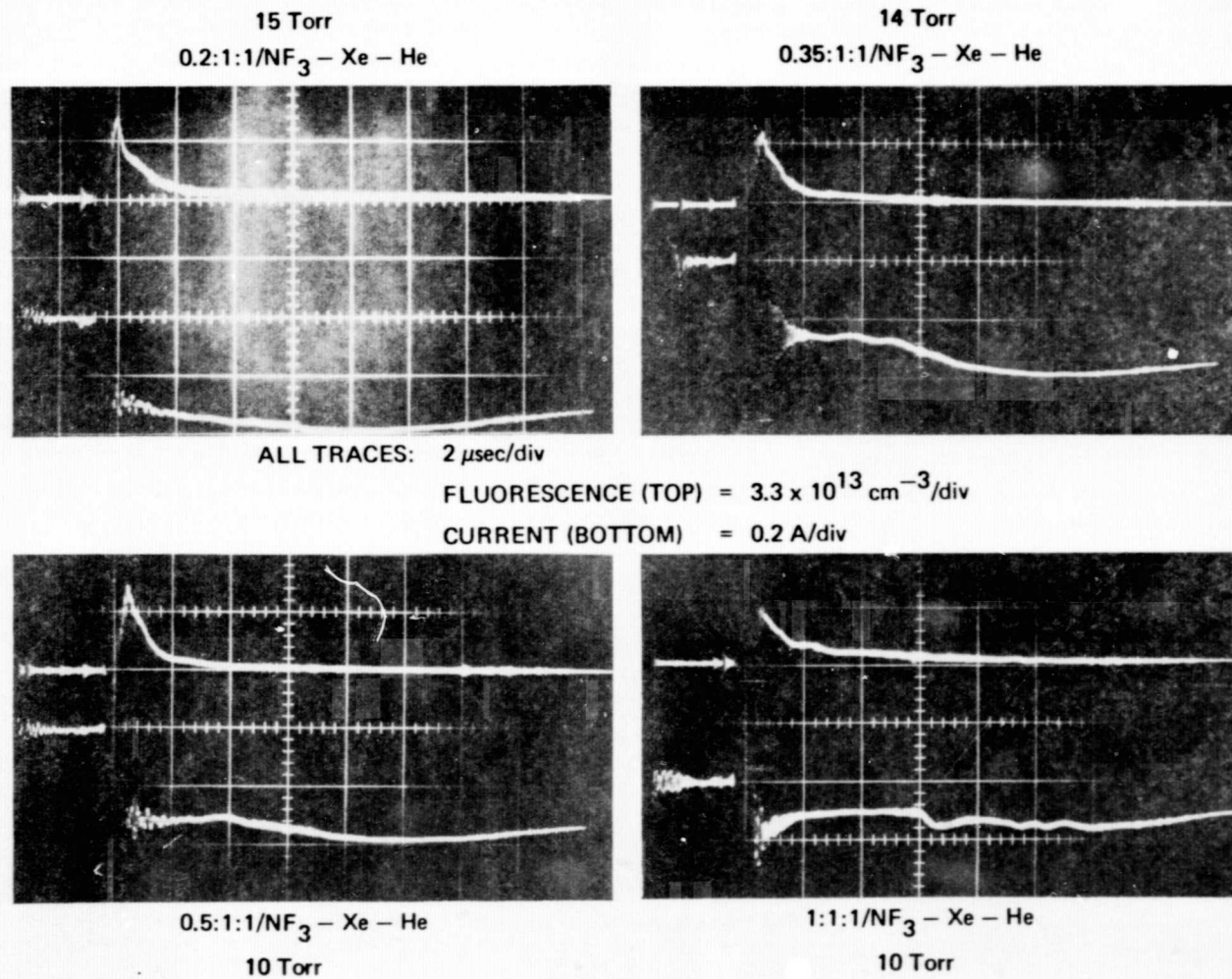


Figure 31. Optimized fluorescence in 1 mm bore tube for several NF<sub>3</sub> mixtures.

0.2:1:1/F<sub>2</sub> - Xe - He  
15 Torr

5117-46

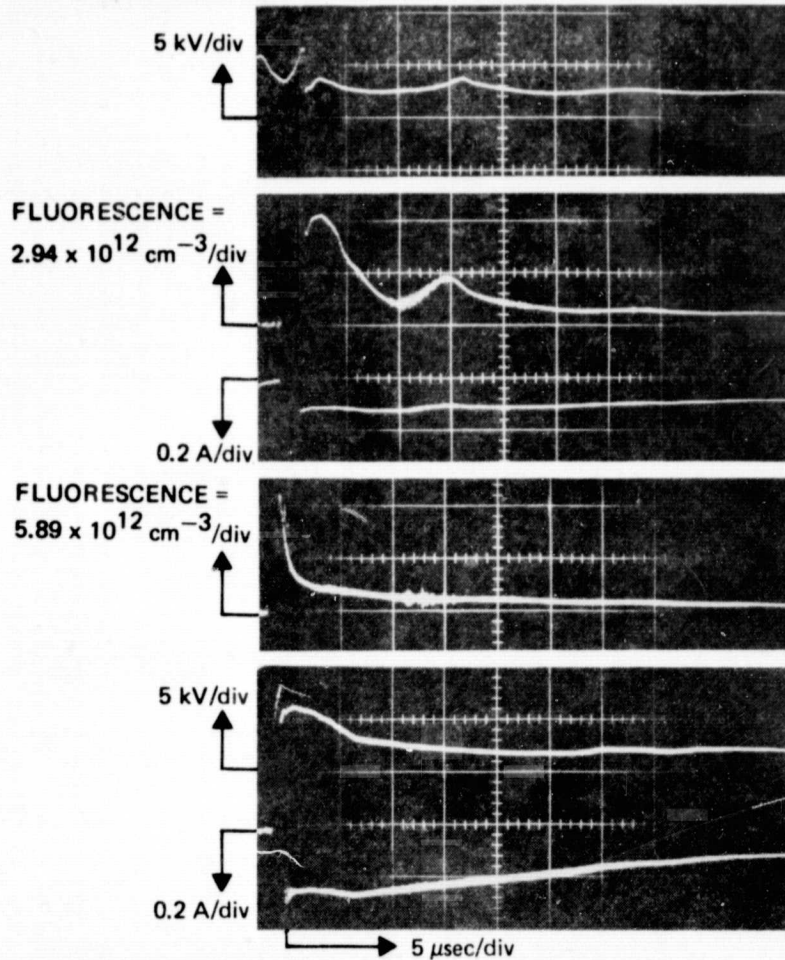


Figure 32. Fluorescence and discharge measurements for a typical F<sub>2</sub> mixture.

E/P in this mixture is  $\sim 200$  V/cm-Torr. The fluorescence observed is also somewhat lower than in the NF<sub>3</sub> mixtures. As in the quasi-cw experiments, the F<sub>2</sub> mixture discharges were visibly nonuniform with the center being considerably brighter than the regions near the walls. This lack of discharge uniformity is undoubtedly linked to the relatively poor performance of these mixtures.

## B. TRANSVERSE DISCHARGE

### 1. Apparatus

The apparatus used in the transverse discharge studies of the XeF xenon fluoride system is shown schematically in Figure 33. The basic components are

- Discharge Chamber: The discharge chamber consists of a fluorine-compatible aluminum box with quartz windows for visual and photographic observation of the discharge, a plexiglass cover with provisions for mounting a resistive electrode, cathode electrode, and a base plate containing six individual spark plugs. The box is vacuum tight and is routinely pumped to a pressure of  $< 10$  MTorr to ensure adequate mixture purity during experiments.
- Preionizer Generator: The preionizer consists of six individual spark plugs. All six plugs are connected in parallel with a  $1 \Omega$  resistor in series for ballasting. The parallel combination of spark plugs are driven by four 2700 pF ceramic capacitors. The capacitors are switched by mercury ignitrons.
- The resistive cathode electrode used was fabricated from a composite material (SAN-polymer and bone coal) and shaped to approximate a Bruce profile having a flat area of approximately  $2 \times 18 \text{ cm}^2$ . The volume resistance of the electrode was  $\sim 200 \Omega\text{-cm}$ .

The discharge gap was nominally 1 cm. Under these conditions the effective discharge resistance through a typical Xe-F mixture ( $F_2 = 0.5$  Torr, Xe  $\sim 4$  Torr, He  $\sim 10$  to 400 Torr) at the peak of the current pulse for a charging voltage of  $\sim 10$  kV was less than the resistance of the resistive electrode thus satisfying the discharge stability requirement discussed in Section 2.

### 2. Results

Although short pulse diffuse discharges  $\sim 50$  nsec were obtained with the use of the resistive electrode, all attempts to extend the pulse length into the 1 to 10  $\mu\text{sec}$  range resulted in a filamentary discharge. This was the case for both the low (10 Torr) and high

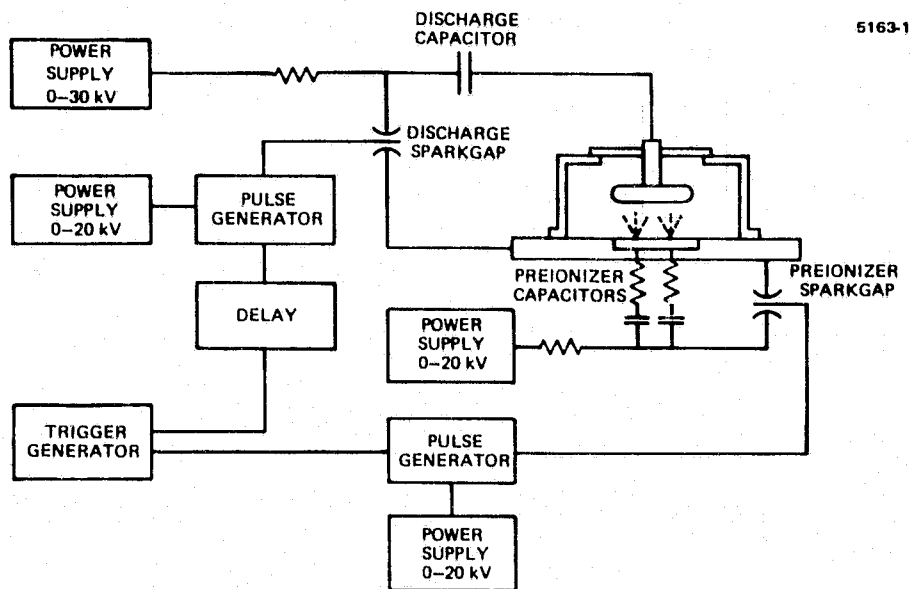


Figure 33. Schematic diagram of the apparatus used to investigate avalanche discharges in rare-gas monohalide device.

(400 Torr) He pressure ranges. As expected, the discharge appeared best in the low pressure range. However, attempts to increase the current density to greater than  $28 \text{ A/cm}^2$  in the low pressure regime met with failure because of discharge spreading over a larger area than the electrodes for voltages higher than  $\sim 10 \text{ kV}$ .

After making these observations, we began adapting a 2 m long transverse discharge chamber, previously used for lasing nitrogen, for pumping the XeF excimer system with a resistive electrode. In this apparatus the discharge is confined by walls so that the discharge cannot spread out to the extent that occurred in the previous apparatus. Also, the discharge length is sufficient to achieve laser oscillation which would enable us to determine definitely the lowest pressure at which laser action can be maintained. Time did not permit completion of these experiments.

## SECTION 7

### DISCHARGE EXPERIMENTS ON THE KAr/K<sub>2</sub> EXCIMER/DIMER SYSTEM

#### A. TRANSVERSE DISCHARGE

##### 1. Apparatus

An experimental apparatus capable of containing potassium vapor at 300°C and 10 atm pressure was developed on a complementary excimer laser program (DARPA Contract N00014-75-C-0081) at Hughes and was modified for use on this program following completion of the DARPA/ONR contract work. This apparatus is shown in Figure 34 and a schematic layout of the discharge apparatus and optical system for monitoring potassium absorption and excimer emission spectra is given in Figure 35. Uniform glow discharges in K-Ar mixtures at 300°C and 7 atm pressure had been achieved previously with this system (Ref. 24). The primary objective of the experimental effort on this program was to obtain a quantitative measurement of the spectral fluorescence power of the K-Ar excimer to determine the laser potential and effectiveness of discharge pumping in systems of this type.

The transverse discharge apparatus contains stainless-steel electrodes with dimensions of 2 cm x 13.5 cm and a gap spacing of 1 cm. The electrode profile is planar over a distance 1.3 times the gap spacing with the sides and ends contoured to the curvature of an ellipse. Sapphire windows are brazed to stainless-steel tubing and mounted with metal vacuum flanges at the ends and on one side port as shown in Figure 34. This arrangement allows observation of sidelight emission and end-on absorption and emission measurements, as well as overall viewing of the discharge uniformity. The apparatus is heated with nine separately controlled electrical heating elements to provide control over spatial temperature uniformity. Individual heaters on the windows were used to maintain window temperatures 10 to 20°C warmer than the coldest point in the apparatus. Twenty-four thermocouples

M11595

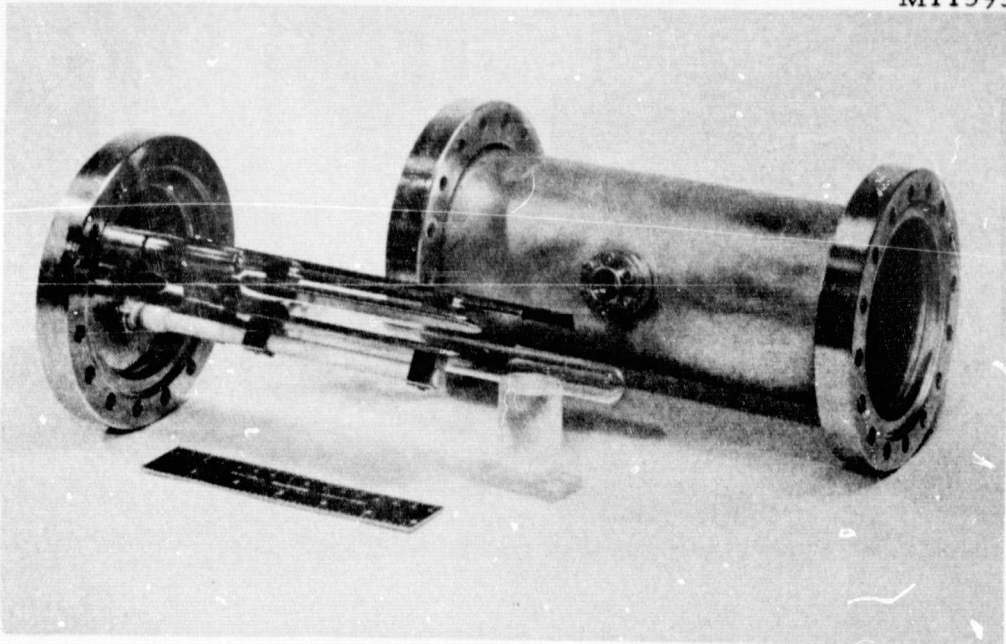


Figure 34. Photograph of KAr/K<sub>2</sub> transverse discharge apparatus.

ORIGINAL PAGE IS  
OF POOR QUALITY

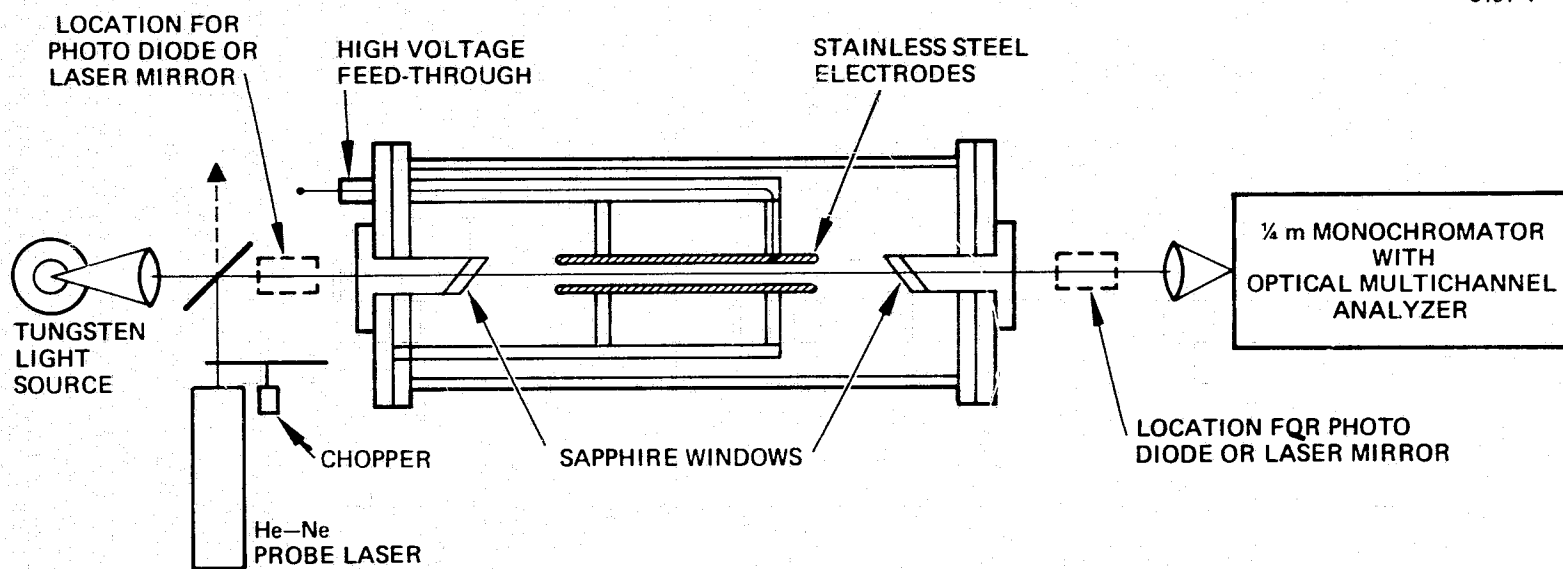


Figure 35. Schematic of  $KAr/K_2$  transverse discharge apparatus and optical monitoring equipment.

were inserted in the flanges and other key locations to monitor the temperature of the system.

Potassium was admitted to the system in a dry box under argon after the apparatus had been thoroughly leak checked and baked out at 150°C on a high vacuum system ( $10^{-6}$  Torr). Previous experience had shown that potassium aerosol formation could be eliminated by first heating the apparatus at low pressure ( $< 1$  Torr) before admitting argon. To provide for mixing of argon and potassium vapor at 300°C the argon was admitted through a perforated sting that extended over the length of the discharge. Additionally, the argon was preheated to 400°C to avoid condensation of potassium by gas-dynamic cooling of argon during the pressurization process.

Discharge currents were measured with a Pearson Model 110 transformer coil and voltages by means of a Tektronix P6015 high-voltage probe. Care was taken to provide a coaxial low-inductance discharge circuit to provide a good impedance match to the discharge and to eliminate electrical noise. The external circuit inductance was determined to be 1.9  $\mu$ H from analysis of current pulse shapes obtained with known resistive loads substituted for the discharge.

Potassium densities were determined from measurements of optical absorption in the 6400 Å region by  $K_2$  and by K-Ar excimer absorption in the 8200 Å region. Resonance line absorption by atomic potassium at 7665 and 7699 Å was also monitored routinely but was not useful for quantitative measurements of potassium at temperatures above 150°C where its density exceeds  $10^{13}/\text{cm}^3$ . A He-Ne laser was used for alignment purposes and to monitor the optical loss at the sapphire end windows which developed as a result of slow chemical attack by potassium vapor. The photodiode shown in Figure 35 was used to monitor the He-Ne laser intensity before and after transmission through the discharge chamber. A tungsten halogen lamp operating at a color temperature of 2500°K provided broadband radiation for measurement of potassium dimer and excimer absorption. Light from this source was collimated by a 7.5 cm f.l. lens and passed through a 5-mm aperture before traversing

the discharge chamber. The radiation transmitted through the discharge region passed through a second 5-mm aperture at the exit of the chamber and was collected by an 8.5 cm f.l. lens with an  $f/\#$  matching the 1/4 m monochromator. An optical multichannel analyzer was used for detection of the spectrum in the exit focal plane of the monochromator and to give either a real time spectral display or an accumulated time averaged spectrum on an oscilloscope screen that could be photographed. The former was normally used for absorption and the latter for emission measurements.

To make a quantitative determination of the spectral fluorescence power from the K-Ar excimer, an RCA 7102 photomultiplier tube was carefully calibrated with the use of a standard tungsten ribbon lamp (G.E. 30 A/T24/17) and a set of interference filters. The photomultiplier spectral sensitivity varied considerably from the manufacturer's specifications at long wavelengths ( $\lambda > 8500 \text{ \AA}$ ); its sensitivity at  $8200 \text{ \AA}$  was  $399 \pm 7 \mu\text{A}/\mu\text{W}$  with a filter having a bandwidth of  $97 \text{ \AA}$ . A plot of the calibrated spectral sensitivity of this detector over the wavelength range studied is shown in Figure 36. This detector-filter combination and two apertures were carefully aligned to view sidelight radiation from the discharge region through the side port on the chamber shown in Figure 34. With this geometry and the calibrated detector, absolute values of the spectral brightness of the discharge region can be measured and used to deduce the absolute fluorescence power of the active medium.

Before the discharge chamber could be used on this program, several repairs and modifications had to be made on the high voltage feedthrough and gas inlet systems. Although these problems, which stem from chemical attack by high temperature potassium, could be solved temporarily they continued to cause difficulties throughout the program and limited the amount of quantitative data that could be collected when all parts of the system were operating properly.

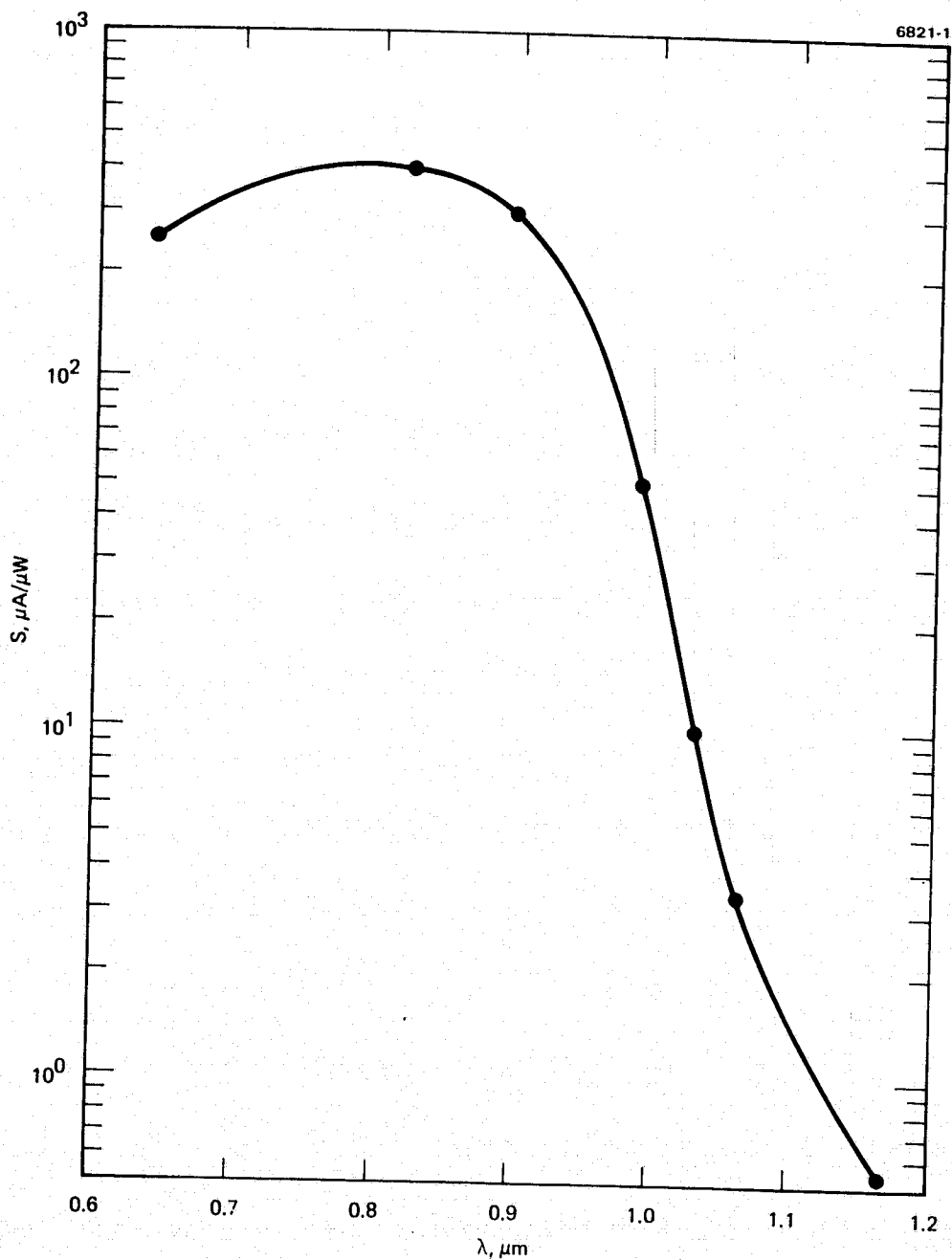


Figure 36. Calibrated spectral sensitivity of photomultiplier used for measurement of absolute excimer fluorescence power; RCA 7102, -1250 V; dark current -  $5 \times 10^{-3} \mu\text{A}$ .

## 2. Experimental Results

The absorption spectra of diatomic potassium and the potassium argon excimer are shown in Figures 37 and 38 for a series of argon pressures and a temperature of 325°C. Note that the dimer spectrum is intrinsically broadened as a result of its vibrational structure, and is virtually unaffected by pressure at the spectrometer resolution of 3 Å, whereas the atomic resonance line absorptions at 7665 and 7699 Å (Figure 38) are extensively broadened with increasing argon pressure. At the normal operating pressure of 105 psia argon, the transmittance through the 30 cm discharge chamber is essentially zero over the spectral range ( $\sim 400$  Å) shown in Figure 38. The measured and calculated excimer absorption outside the resonance line spectral region are in good agreement. Also we found that the potassium density, as determined from the dimer absorption spectra shown in Figure 37, is in good agreement with the density of potassium calculated from thermodynamic data. This agreement confirms that we were able to obtain essentially equilibrium potassium vapor densities in our discharge apparatus at 325°C and a total pressure of 105 psia in spite of the competing side effects of aerosol formation and slow chemical reaction of potassium with some of the materials in the discharge chamber.

Electrical characteristics were measured routinely, and an example of the discharge voltage and current waveforms is shown in Figure 39. In these experiments the discharge is initiated by applying an overvoltage across the discharge electrodes which initiates spontaneous breakdown of the medium after 0.5 to 1  $\mu$ sec delay with subsequent formation of a uniform yellow-orange discharge. As shown in Figure 38 the voltage drops quickly to the operating voltage of the medium,  $\sim 1$  kV in this case, remains constant for a short duration while the current pulse builds up, and then decreases gradually as the charge on the capacitor decays to zero. As is evident from the waveforms shown in Figure 38 the circuitry is reasonably well matched to the discharge since the system shows only slight underdamping. The power deposited in the discharge at the peak of the current pulse for these experimental conditions is

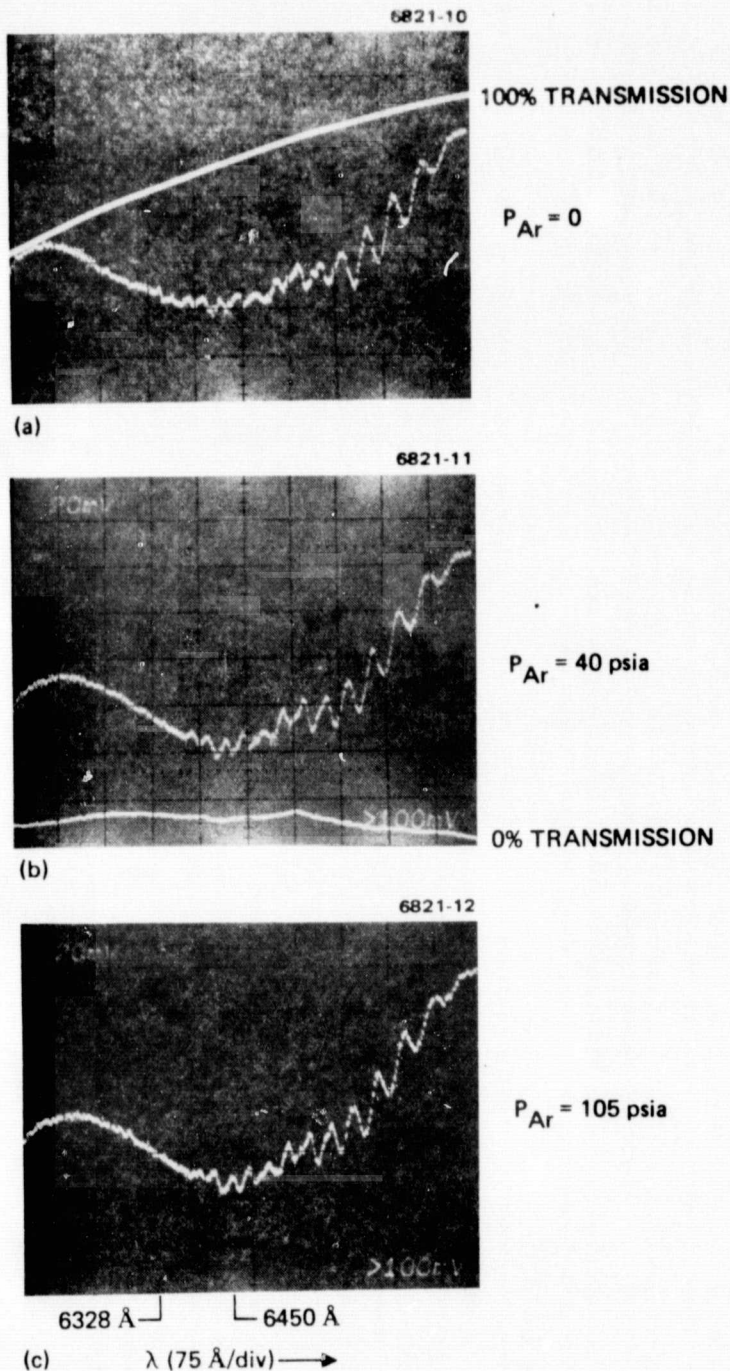
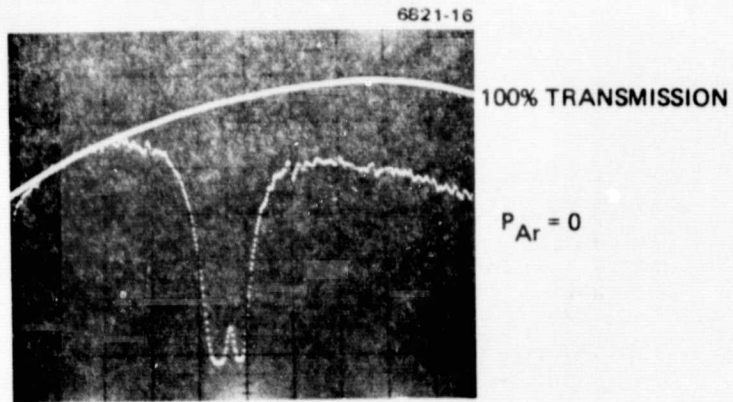
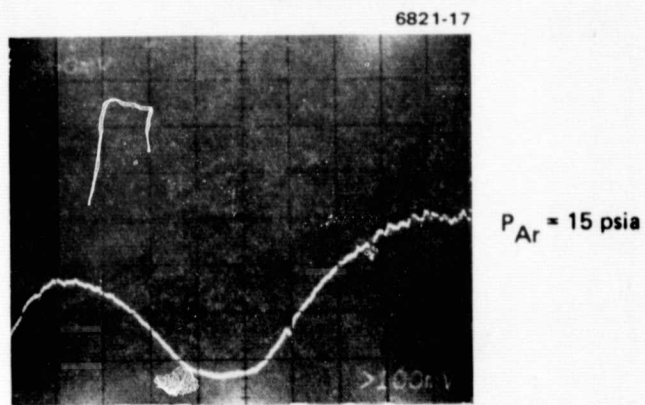


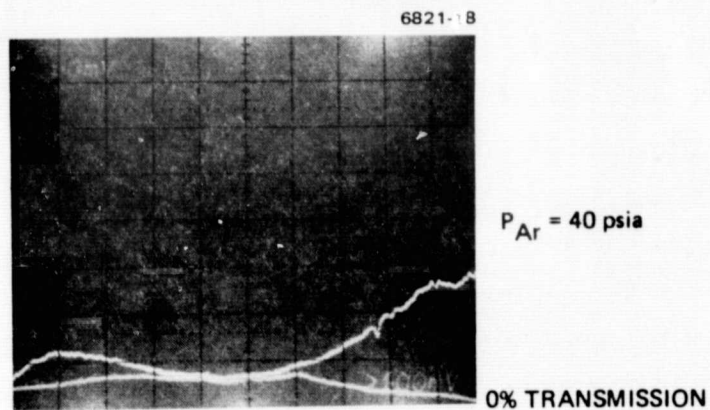
Figure 37. Transmission spectra of potassium dimer at 325°C and argon pressures from 0 to 105 psia.



(a)



(b)



(c)

Figure 38. Transmission spectra of atomic potassium at 325°C and argon pressures from 0 to 40 psia.

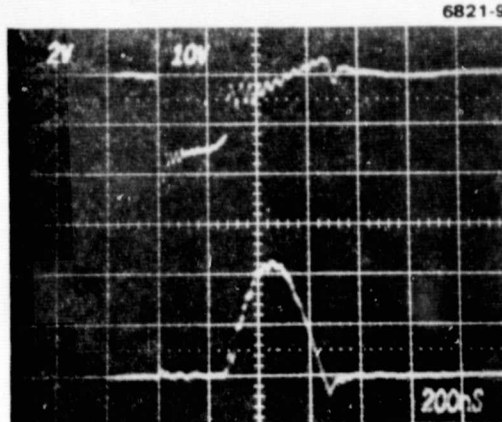


Figure 39. Current and voltage waveforms for potassium-argon transverse discharge at 325°C, 105 psia argon. Upper trace - 2 kV/div, lower trace - 100 A/div; electrode area is 27 cm<sup>2</sup>; time scale is 200 nsec/div; C = 0.01 μF.

$\sim 8 \text{ kW/cm}^3$ , a value expected to be sufficient for producing significant optical gain in the K-Ar excimer.

An emission spectrum of the transverse discharge-pumped K-Ar excimer as viewed from the end-on configuration of the spectrometer is shown in Figure 40. Resonance line absorption by unexcited potassium outside the discharge region causes the line reversals seen at 7665 and 7699 Å. Note the asymmetry of the excimer emission on the long wavelength side of the resonance lines and the extension of the emission out to the 8600 Å region. The relative values of excimer emission at the wavelengths 7874, 7981, 8091, and 8319 Å are 1:0.65:0.5:0.3 as measured from this type of qualitative spectral data. Corresponding relative values of excimer emission as calculated from our theoretical model are 1:0.7:0.6:0.4, which show good agreement with the experimental data.

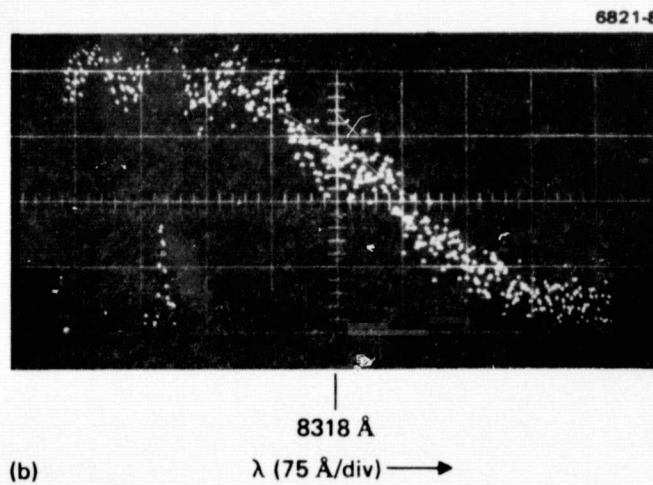
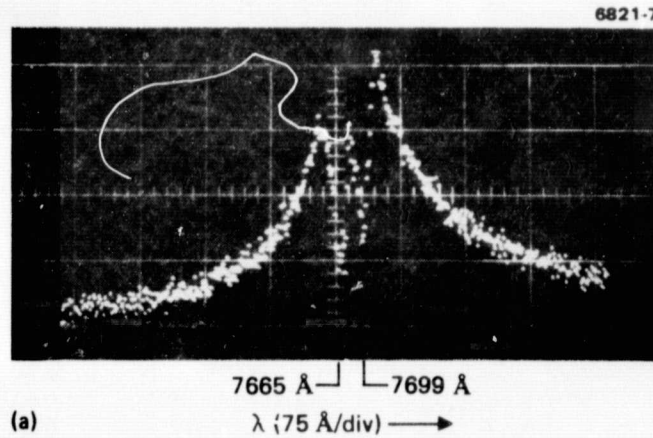


Figure 40. Emission spectra of transverse discharge pumped potassium excimer at 325°C and 105 psia argon. Amplitude scale of lower spectrum is increased by a factor of 5 compared to the upper spectrum.

Unfortunately, much of the spectral data obtained on this program are qualitative rather than the quantitative information required for proper evaluation of the laser potential of this system. Numerous experimental difficulties were encountered with the electrical aspects of the discharge system during the period when quantitative emission measurements were attempted. Some quantitative data were obtained, however, and were analyzed according to the double-aperture geometry described in the previous section. With a calibrated filter and detector located adjacent to an aperture of area  $A_1$ , which is separated by a distance  $D$  from a second aperture of area  $A_2$  located near the discharge region, the spectral brightness of the discharge is given by

$$B = \frac{\phi D^2}{A_1 A_2 \Delta \lambda T_f(\lambda)} .$$

The units of brightness,  $B$  are  $\text{W}/\text{cm}^2$  - steradian  $^{-1}$ ,  $\phi$  is the power received by the detector in  $\text{W}$ ,  $A_1$  and  $A_2$  are measured in  $\text{cm}^2$ ,  $\Delta \lambda$  is the bandpass of the detector filter,  $97 \text{ \AA}$  and  $T_f(\lambda)$  is the filter transmission at the center of its bandpass. This equation for spectral brightness is an approximation to the complete spatial integral over the two apertures and is accurate for circular apertures whose dimensions are small compared to their separation  $D$ . For the measurements reported here the diameter of  $A_1$  and  $A_2$  is 2 mm and  $D \geq 400$  mm. Similarly, the product  $\Delta \lambda T_f(\lambda)$  is a good approximation to the spectral integral as found by numerical integrations carried out during the detector calibrations. For the case of low optical gain over the transverse dimension of the discharge,  $X_o$ , the fluorescence power,  $P(\lambda)$  in  $\text{W}/\text{cm}^3$  -  $\text{Å}$  is related to the spectral brightness by

$$P(\lambda) = \frac{4\pi}{X_o} B(\lambda) .$$

The gain of the medium  $g_0$ , can then be computed from  $P(\lambda)$  as before:

$$g_0 (\text{cm}^{-1}) = k \lambda^5 P(\lambda)$$

where  $k = 4.2 \times 10^{-22}$  for this system.

The quantitative emission data were analyzed in this way and yielded a gain value far below that predicted by theory. A comparison between experimental and theoretical values for  $P(\lambda)$  is shown by the plots in Figure 16. There were visual indications during the discharge pulses used to obtain this fluorescence data that hot spots were forming in the discharge regions outside the region viewed by the fluorescence detector. The occurrence of such high current density regions could account for the discrepancy between theory and experiment for both the current and fluorescence waveforms in Figure 16.

## B. CAPILLARY DISCHARGE

### 1. Laboratory Apparatus

The alkali excimer-dimer system poses significant materials problems that must be considered in the design of apparatus. Potassium is chemically reactive with many materials and must be heated to  $\sim 300^\circ\text{C}$  to achieve sufficient density for laser oscillation. With these factors in mind we have designed and constructed an apparatus for conducting discharge experiments with potassium rare-gas mixtures at temperatures between 250 to  $300^\circ\text{C}$ . A schematic drawing of the high temperature apparatus is shown in Figure 41. This apparatus is constructed primarily of stainless steel tubing and incorporates stainless steel packless valves. The entire system was baked out at  $150^\circ\text{C}$  and purged with research purity argon prior to use for discharge measurements.

Separate ovens are used for the discharge tube and potassium reservoir in order to eliminate condensation effects in the discharge tube. Homogeneous mixtures of potassium vapor and rare gases are prepared in a  $100 \text{ cm}^3$  stainless steel cylinder. Partial pressures of potassium are

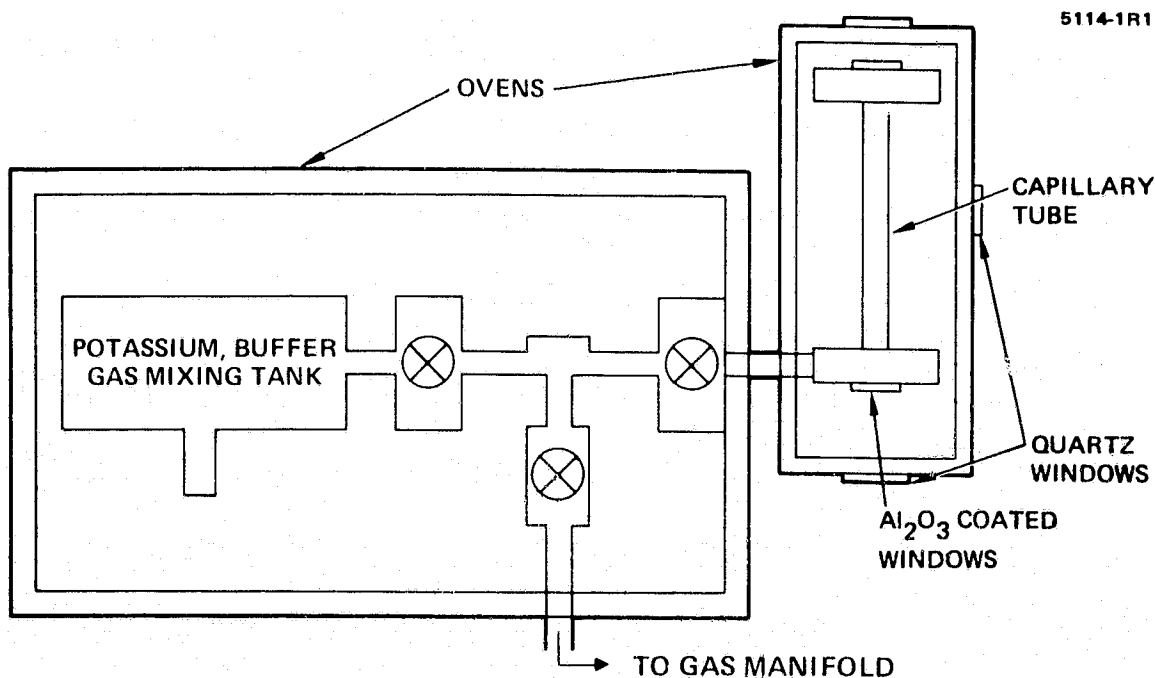


Figure 41. Schematic diagram of KAr/K<sub>2</sub> capillary discharge apparatus.

controlled by the temperature of this reservoir which contains enough potassium to produce saturated vapor pressures. The small volume discharge tube is then filled by gas expansion from this chamber: the potassium dimer (K<sub>2</sub>) absorption at 6328 Å and resonance line absorption by atomic potassium at 7665 Å and 7699 Å are used to determine dimer and atomic densities, respectively. A photograph of this apparatus is shown in Figure 42. The remainder of the electrical and gas handling apparatus for the potassium experiments is shown in Figure 43.

Stainless steel cylindrical cavity electrodes as shown in these figures were found to be more satisfactory than simple tungsten pin electrodes which were used in our first discharge experiments. The discharge tube was situated as shown in Figure 42. The Pyrex capillary

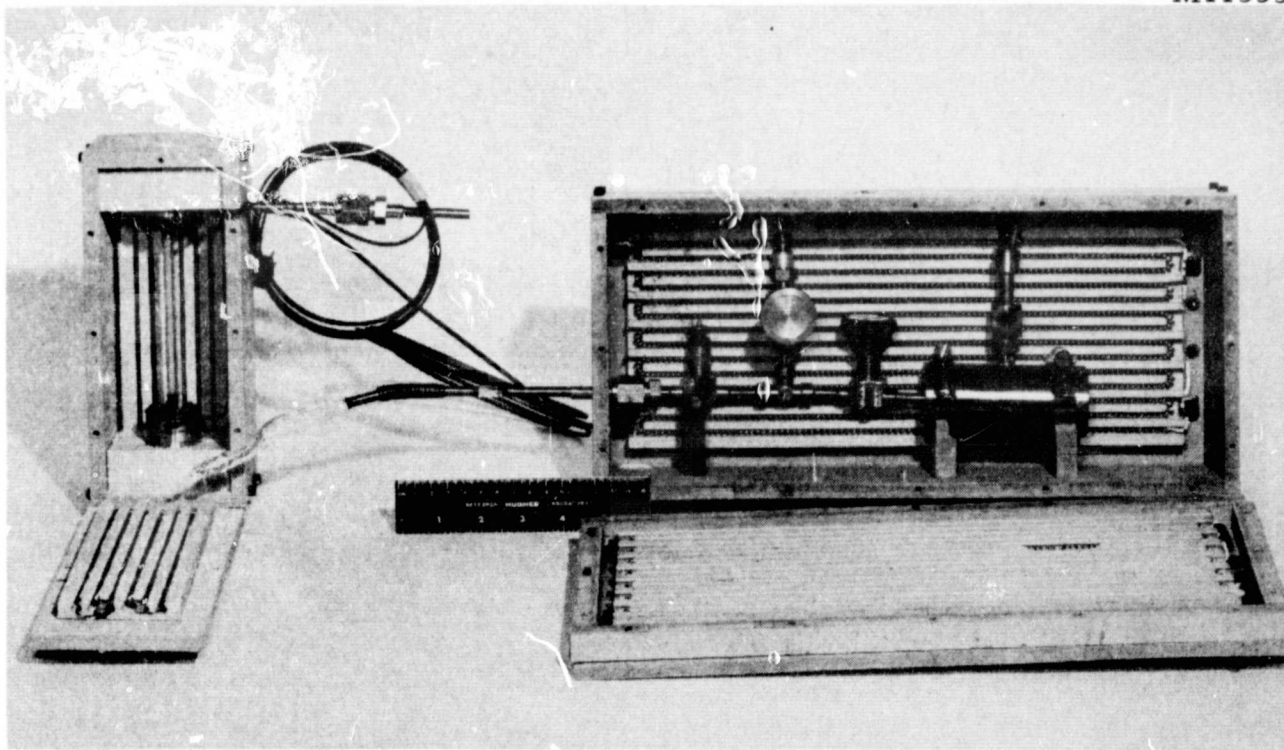
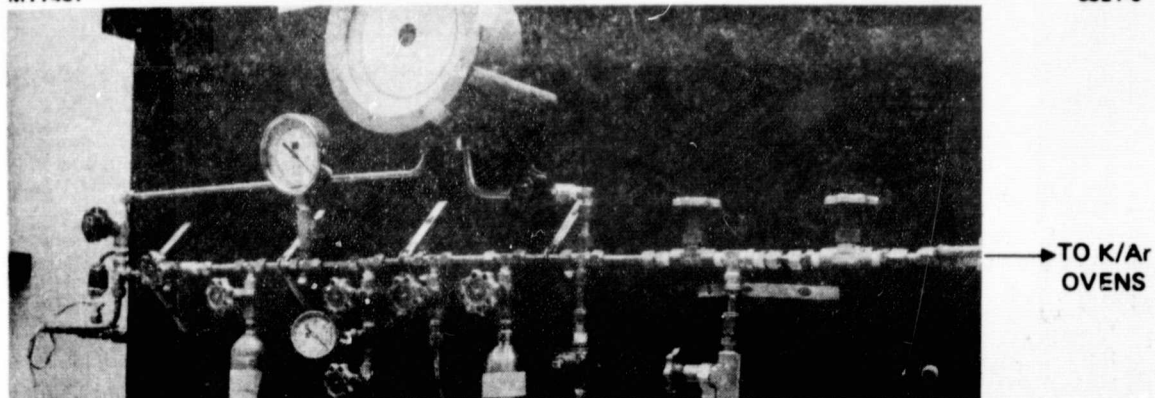


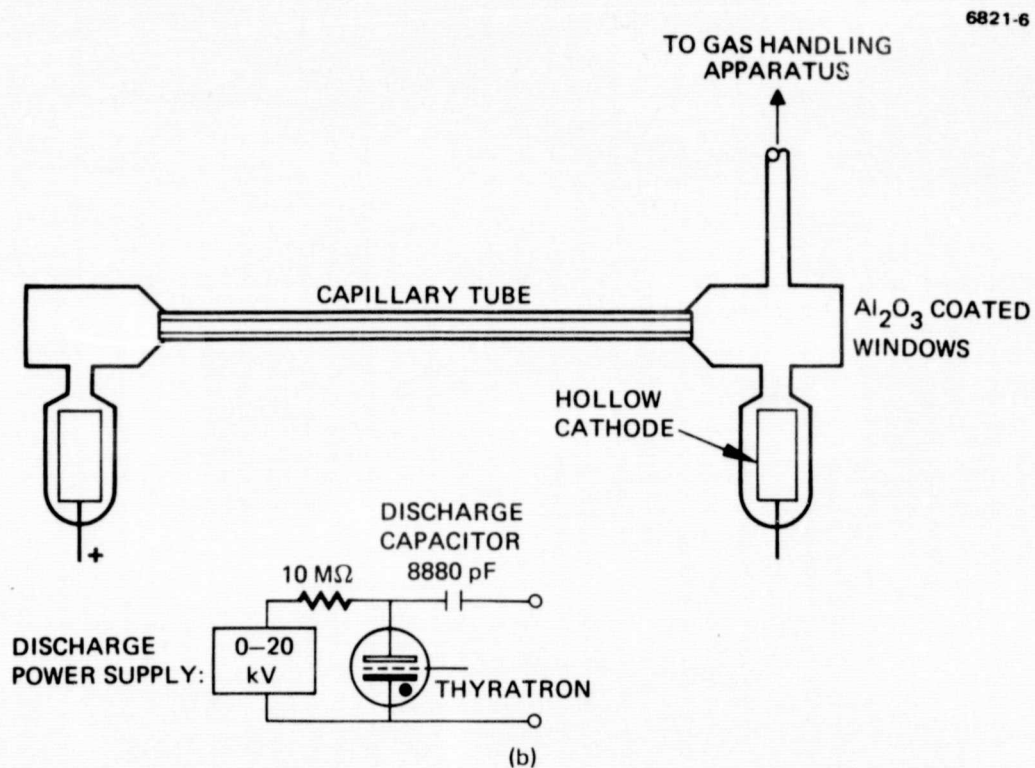
Figure 42. Photograph of KAR/K<sub>2</sub> capillary apparatus in final stages of fabrication.

E-7



(a)

Figure 43(a). Capillary discharge gas handling manifold.

Figure 43(b). Schematic diagram of KAr/K<sub>2</sub> capillary discharge tube and pulse circuit.

discharge tube was constructed with an i.d. of 2 mm and active length (between electrodes) of 10 cm; the overall length of the tube was 15 cm. Since potassium reacts with Pyrex (K apparently replaces the Si), the inside surface of the tube windows was sputtered with sapphire ( $\text{Al}_2\text{O}_3$ ) prior to operation. Details of the potassium Pyrex reaction effects on the fluorescence measurements will be discussed in the next section.

All of the capillary discharge experiments conducted on this program have been done with the apparatus shown in Figures 41 and 42 and will be discussed in the following section. The potassium vapor pressure is determined by the temperature at the coolest point of the gas filling system. Temperatures were measured at more than 15 positions throughout the system using copper-constantan thermocouples. The value of the potassium density obtained from temperature measurements was compared with that obtained by measuring the X  $\rightarrow$  B dimer absorption (at  $\sim 6450 \text{ \AA}$ ) and the atomic resonance absorptions (at 7665 and 7699  $\overset{\circ}{\text{A}}$ ) along the discharge tube. Figure 44 shows the apparatus used for these measurements. A calibrated tungsten white light source was incident at one end of the capillary tube. The transmitted radiation was then focused by an 8-cm focal length lens into a 1/4 m Jarrell Ash spectrometer. Spectra were recorded using an Optical Multichannel Analyzer whose output was viewed in real time on an oscilloscope. This system established the presence of potassium in the discharge tube and verified the equilibrium potassium density. Absolute fluorescence measurements were conducted with a variety of gas mixtures and electrical parameters in order to evaluate discharge characteristics and laser potentialities. The optical configuration used for this purpose is shown schematically in Figure 45. An RCA 7102 photomultiplier and optical filter were calibrated with a tungsten ribbon standard source and used to measure the side light emission from a well defined volume in the discharge tube. Alignment of the discharge tube with the spectrometer and detector was achieved with the use of a He-Ne laser and conventional alignment techniques. These measurements can then be

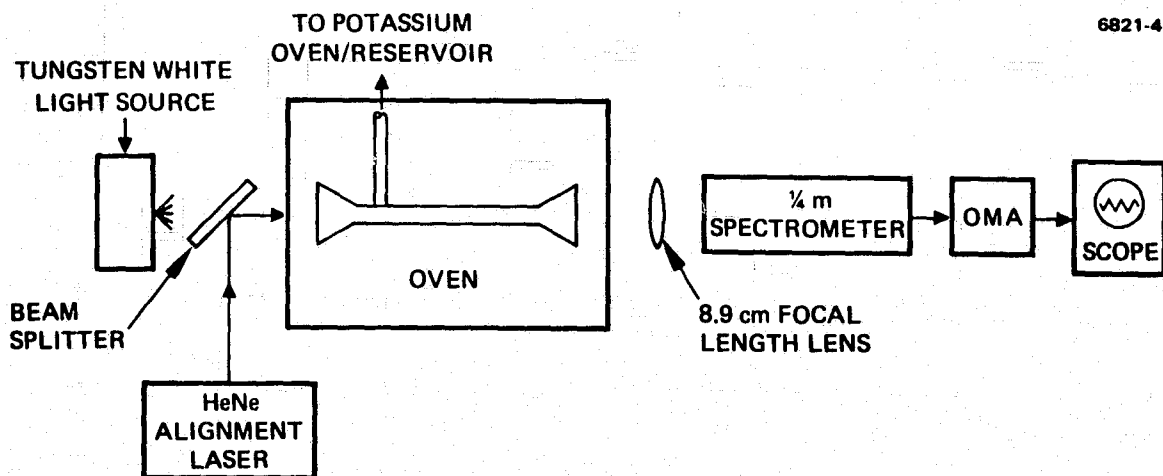


Figure 44. Apparatus used for emission/absorption measurements.

6821-3

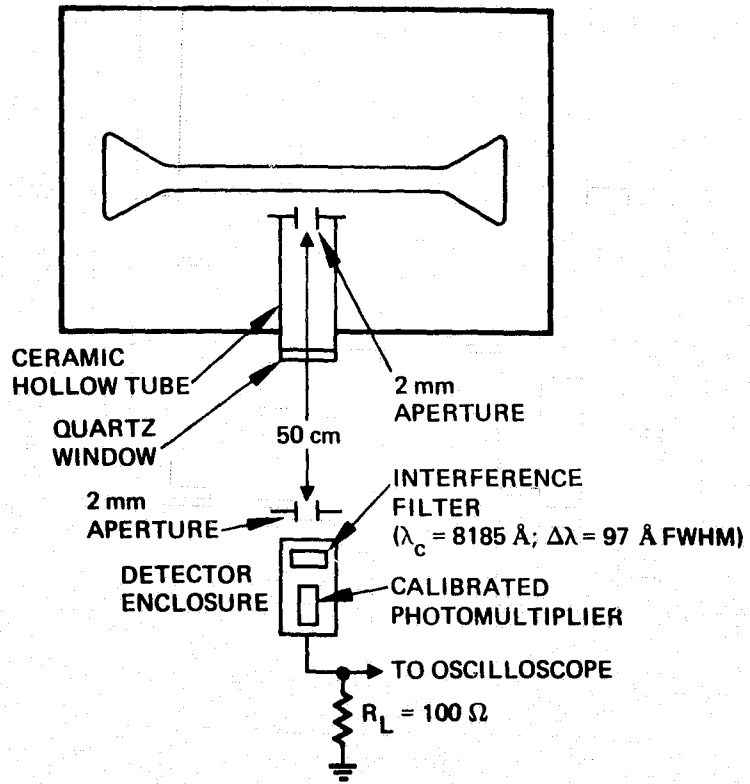


Figure 45. Experimental arrangement for absolute fluorescence measurements.

ORIGINAL PAGE IS  
OF POOR QUALITY

used to determine excited state populations of K Ar and the maximum optical gain coefficient in accordance with the formulas presented in the previous sections.

## 2. Experimental Results

The results of measurements taken on the  $K_2/K$  Ar capillary discharge apparatus follow.

The primary measurements carried out were tests for gain and the determination of discharge conditions. Data obtained from the  $K_2/K$  Ar apparatus included discharge voltage, discharge current, and absolute fluorescence intensity measured as a function of gas mixture, pressure, and external circuit parameters. Upper state populations and small-signal gain were calculated from the fluorescence data according to the procedures outlined in Section 7.A.1.

As mentioned in the previous section, potassium reacts with the Pyrex discharge tube which results in a brown colored film that coats the inner surfaces of the glass. This has a twofold effect. First, the reaction tends to "getter" the potassium from the gas phase, leading to a decrease in density in the tube. This point will be discussed in more detail. Second, the potassium induced film reduces the optical transmission through the affected surfaces. In order to minimize this effect on the longitudinal absorption/emission measurements, the tube windows were coated with sapphire ( $Al_2O_3$ ) which is much less reactive with potassium than Pyrex. As a result of this coating, negligible changes in optical transmission through these coated surfaces resulted. However, due to the uncoated inner walls of the capillary tube, brown film deposits were unavoidable. Hence, the sidelight fluorescent measurements were affected throughout the course of this experiment. To correct the fluorescence measurements for this effect, the sidelight fluorescence from a controlled pure argon discharge (at a given pressure) in the region of the  $A \rightarrow X$  K Ar excimer transition was recorded prior to each excimer measurement. In addition, the current and voltage of this discharge was recorded to insure that only the argon controlled

the discharge (as opposed to potassium or other residual gases). Typically, the argon fluorescence decreased 5 to 10% of its previous value after a given set of measurements (with the V-I characteristics unchanged), thus indicating that additional potassium reacted with the glass each time.

A typical set of experimental data is shown in Figures 46 to 50. Figure 46 shows the V-I characteristics of the discharge pulse. For these measurements, the power supply was set at 2 kV, charging a 8880 pF capacitor through a 10 M $\Omega$  resistor. The total pressure in the discharge apparatus was about 2 atm. Figure 47 shows the raw side-light fluorescence output from the calibrated photomultiplier. For this measurement, a narrowband (97 Å) interference filter (8185 Å) was used to pass radiation within the excimer emission band. Figure 48 shows the measured response of this filter for various angles of rotation (about an axis in the plane of the filter) which shows that only small amplitude and optical frequency passband changes result for angular rotations up to 4°.

The density of potassium was determined from both oven temperature and dimer ( $X \rightarrow B$ ) absorption. Figure 49 shows the spectrum of the dimer absorption band. Figure 50(a) shows the white light absorption of the potassium-argon excimer and Figure 50(b) shows the K-Ar excimer emission. The self reversed resonance lines are clearly visible in the center of the emission spectrum and arise from unexcited potassium outside the discharge regions at the tube ends. Figure 16 in Section 5 shows a plot of both the calculated and measured values for the gain and fluorescence as a function of time.

Operational problems were encountered during the course of most of these experiments. A major problem was the apparent "gettering" of potassium to the walls of the discharge tube during the period when quantitative emission measurements were made. The reduction in potassium density was so severe at times that the measurements had to be performed within 5 to 10 minutes after the introduction of the excimer into the tube. This is in sharp contrast to earlier experimental work when qualitative emission and quantitative absorption

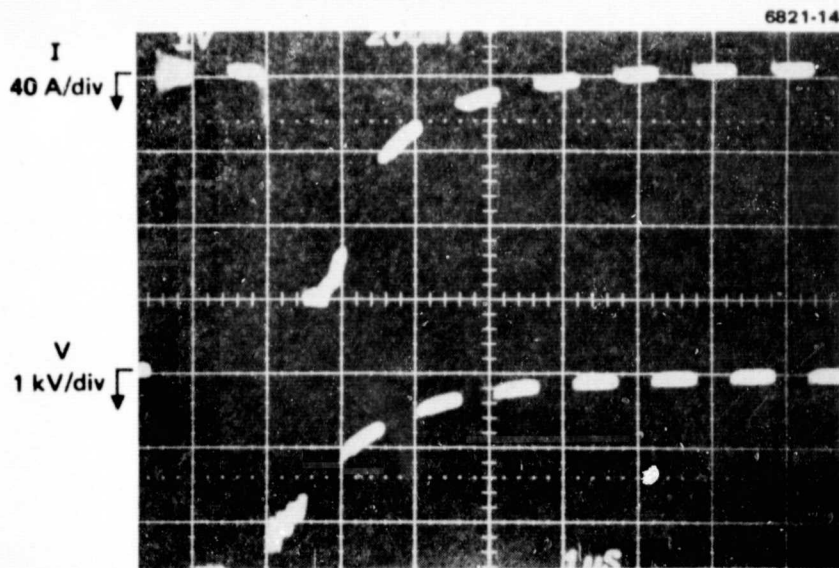


Figure 46. I-V characteristic of K/Ar discharge.

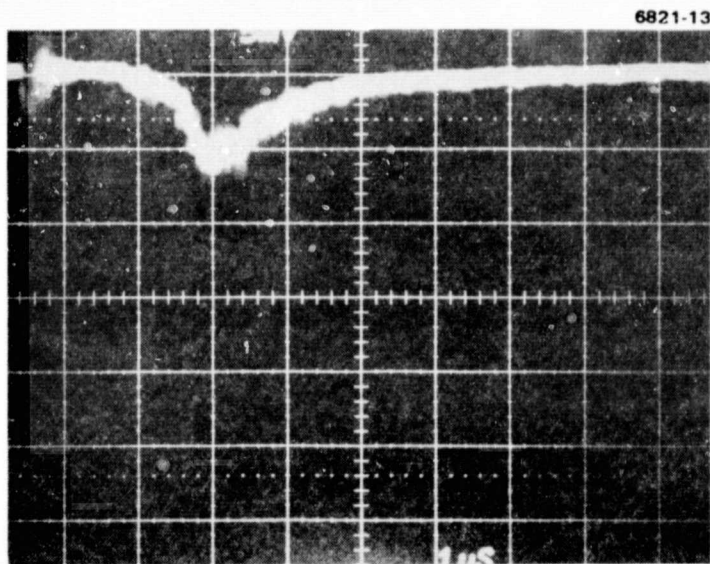


Figure 47. Photomultiplier output of fluorescence (through bandpass interference filter;  $\lambda_c = 8185 \text{ \AA}$ ,  $(\Delta\lambda = 97 \text{ \AA})$  of K/Ar excimer discharge.  $R_2 = 100 \Omega$ .

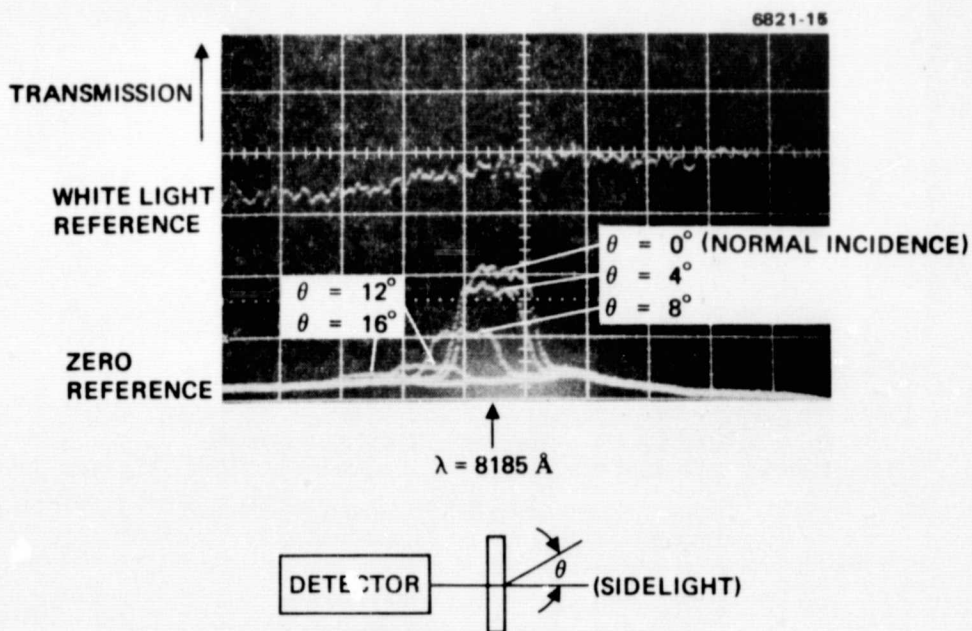


Figure 48. Angular response of interference filter used for fluorescence measurements ( $80^\circ/\text{div}$ ).

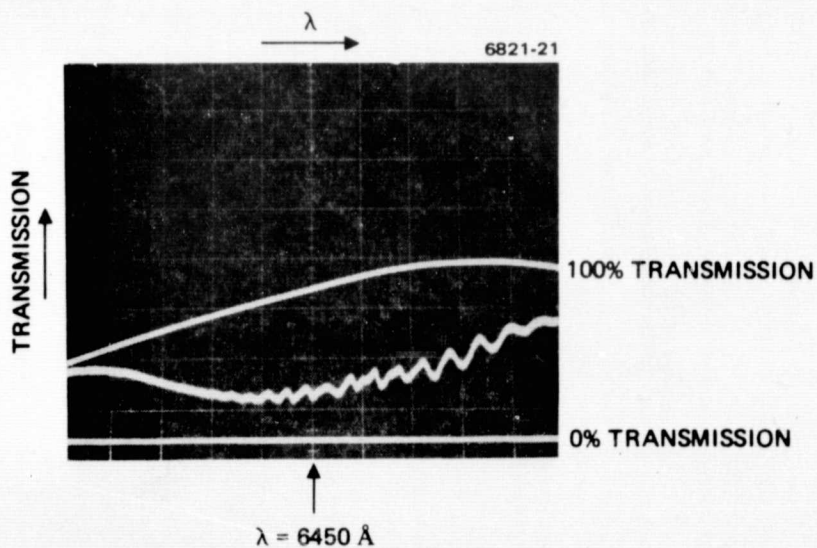


Figure 49. Potassium dimer ( $X \rightarrow B$ ) absorption spectrum. Wavelength scale:  $75 \text{ \AA}/\text{div}$ .

ORIGINAL PAGE IS  
OF POOR QUALITY

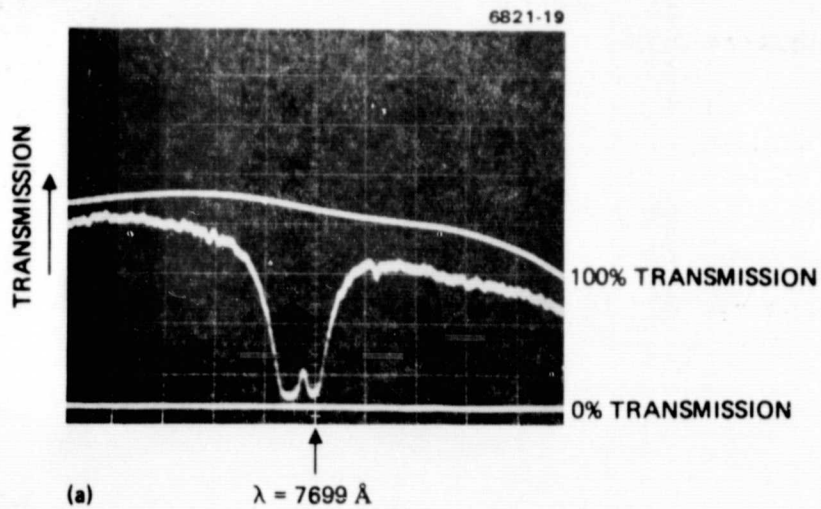


Figure 50(a). Potassium-argon absorption spectrum. Wavelength scale: 75 Å/div.

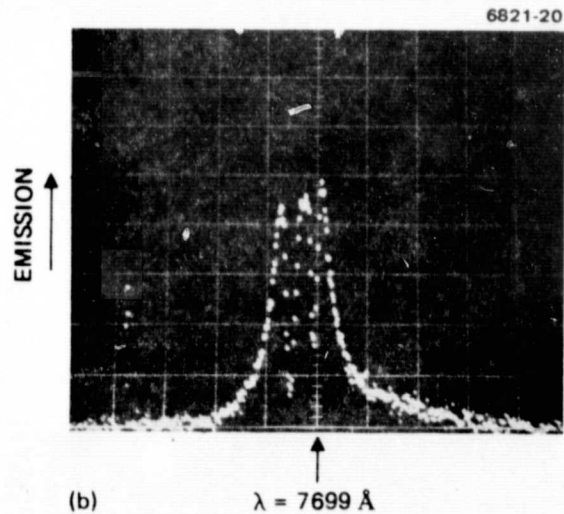


Figure 50(b). Potassium-argon excimer emission spectrum. Wavelength scale: 75 Å/div.

measurements were made (see Figures 49 and 50). This apparent "gettering" could have been due to a cold spot in the system during these particular experiments. However, this seems unlikely due to the presence of over 15 thermocouples distributed throughout the oven and discharge tube apparatus with none showing abnormally low temperatures. Since the V-I characteristics remained essentially constant (with a relatively low voltage that wouldn't ignite a pure argon discharge) during the first several minutes after filling the tube, the absolute fluorescence values measured during this time period are reasonably accurate but represent a lower limit on the gain of the K/Ar excimer. There is also a possibility that part of the observed fluorescence signal used to calculate optical gain may be due to atomic argon emission. Some of the measurements made during the period when potassium gettering was a problem showed argon emission lines in the bandpass spectral region of the interference filter although these lines were not observed earlier when qualitative emission measurements such as those shown in Figure 50(b) were made.

## SECTION 8

### CONCLUSIONS

Of the four combinations of excimer systems and pumping methods explored in this study, the capillary discharge pumped KXe/K<sub>2</sub> is probably the closest to demonstrating cw excimer laser action. This is due to the lower predicted pumping threshold required compared to the other molecular system explored and to the predicted and demonstrated discharge stability. At least a one-year period of further study on this system is estimated to be required to demonstrate long-pulse laser action and to obtain definite conclusions concerning the cw operation of this system.

Scalable cw excimer lasers are probably further in the future. The alkali excimer-dimer system seems promising, theoretically, because of their inherent discharge stability but have not yet demonstrated consistent, uniform discharge behavior in the laboratory nor any discharge pumped laser action. On the other hand, the rare-gas halide excimer systems are demonstrated lasing systems but possess an inherent discharge instability which, so far, has limited pulse lengths to less than one microsecond.

ORIGINAL PAGE IS  
OF POOR QUALITY.

## REFERENCES

1. C.E. Moore, Atomic Energy Levels, National Bureau of Standards.
2. H.M. Michaels and F.E. Harris, J. Chem. Phys. 19, 1464 (1963).
3. A.J. Palmer, J. Appl. Phys. 41, 438 (1970).
4. J. Pascale and J. Vandeplanque, CEA Report, March 1974.
5. C. York and A. Gallagher, Jt. Inst. Lab. Astrophys. Rpt. 114, October 1974.
6. R. Carbone and M. Litvak, J. Appl. Phys. 39, 2413 (1968).
7. R. Hill, et al., Appl. Phys. Lett 23, 373 (1973).
8. C. Cooper, C. Cobb, and E. Tolnas, J. Mol. Spectrosc. 7, 223 (1961).
9. C. Harzberg, Spectra of Diatomic Molecules (B. Van Nostrand, 1950).
10. J. Ewing and C. Brau, Phys. Rev. A12, 129 (1975).
11. E. George and C. Rhodes, Appl. Phys. Lett. 23, 139 (1973).
12. A.V. Phelps, Jt. Inst. Lab. Astrophys. Rpt. 110, September 1972.
13. J.G. Eden, Appl. Phys. Lett. 31, 448 (1977).
14. A. von Engle, Ionized Gases (Oxford Clarendon Press, 1965).
15. L.J. Kieffer, Jt. Inst. Lab. Astrophys. Information Center Rpt. No. 13, University of Colorado, September 30, 1973.
16. S.C. Brown, Basic Data of Plasma Physics (The MIT Press, 1967).
17. P. Mahadevan and R. Hofland, Aerospace Corporation reprint (1976).
18. C.A. Beam and J.J. Ewing, Semiannual Tech. Rpt., Contract N00014-75-C-0063, Avco Everett Research Laboratories, Inc.
19. A. Hill, Appl. Phys. Lett. 22, 670 (1973).
20. D. Rensch, Final Technical Report, "High Pressure CW Chemical Laser - Phase 1," ARPS order No. 1180, Nov. 1976.
21. A.C. Gallagher and A.V. Phelps, Final Technical Report, ERDA Contract No. E(49-1)-3800, Feb. 1977.
22. S.C. Brown, Basic Data of Plasma Physics (The MIT Press, 1967).

23. A.J. Palmer, J. Appl. Phys. 47, 3088 (1976).
24. A.J. Palmer and L.D. Hess, Final Technical Rpt. DARPA Contract N00014-75-C-0081, (1976).

APPENDIX

Section 1: XeFL Model

C XEFL - DISCHARGE PUMPED XEFL LASER

REAL MASE, MASXE, MASM, M1, M2, MI, K, K3X, K5X, K41, NEO, NE  
 REAL NEP  
 REAL J  
 REAL M  
 REAL LENGTH  
 REAL KPLUS, KNI, KEL  
 REAL L  
 REAL MD1, MDI, MD  
 EXTERNAL FUNC  
 COMMON/STOR/M, XE, NE, NEP, CM1, CX1, XEFG, EM1, EX1, EXEFU, CEL,  
 +MASE, MASM, V, LENGTH, A, L, R, DT, E, FL

C CONSTANT DATA

MASE=0.5E6; E=1.6E-19; MASXE=131\*1840\*.5E6  
 L=0  
 C=1000E-9  
 D=.1  
 A=3.14\*(D/2)\*\*2

C M=HELIUM

MASM=4\*1840\*.5E6  
 EX1=8.3; EX2=9.6; EXI=12.08  
 EM1=22.; EM2=23.; EMI=24.5  
 EXEFU=3.1  
 CX1=.3E-16; CX2=.05E-16; CXI=.11E-16  
 CX1I=5E-16; CX2I=5E-16  
 CM1=.025E-17; CM2=.025E-17; CM1I=.08E-17  
 CM1I=5E-16; CM2I=5E-16  
 CEL=5.5E-16  
 CDIF=1E-15

ORIGINAL PAGE IS  
 OF POOR QUALITY

LENGTH=1.6  
 K=1440E19  
 NEO=1E10  
 TGO=.03  
 AX2=4E7; AM2=32E7; AXED1=4E7; AMD1=32E7; AXEF=2E7; AMX=10E7

C INITIAL CONDITIONS

WRITE(5, 50)  
 50 FORMAT(2X, 1HM, 5X, 2HFL, 5X, 2HXE, 5X, 2HVO, 5X, 1HR, 5X, 2HDT,  
 +5X, 6HIPRINT, 5X, 4HTMAX, 5X, 2HVS)  
 ACCEPT\*, M, FL, XE, VO, R, DT, IPRINT, TMAX, VS  
 TG=TGO  
 V=VO  
 WRITE(5, 80)  
 80 FORMAT(4X, 4HTIME, 6X, 5HYDISC, 5X, 1HJ, 9X, 2HNE, 8X, 3HFNI,  
 +7X, 2HMI, 8X, 3HXEI)  
 WRITE(5, 85)  
 85 FORMAT(7X, 2HFL, 8X, 3HXEI, 7X, 4HXEFU, 6X, 4HXEFG, 6X, 4HGAIN, 6X, 2HTG,  
 +8X, 2HTE)

```

C TIME STEP
  20 ISTEP=ISTEP+1
      T=T+DT
      IF(T-TMAX) 21,21,22
  21 CONTINUE
C CIRCUITRESPONSE
  NE=NEO+MI+XEI+MDI+XEDI+XEMI-FNI
  VO=VO-DT*J*A/C
  IF (VO-VS) 4,5,5
  5 V=VO; GO TO 6
  4 V=VS
  6 CONTINUE
  IERR=0; JND=1; EPS=0.02
  IF (ISTEP-1) 10,10,8
  8 IF (TE-.5) 9,9,10
  9 TE=.5; GO TO 2
  10 CONTINUE
      TE=SOLN(IND, FUNC, .4, 10., EPS, IERR)
      IF(IERR) 1,2,1
  1 TE=.4
  2 CONTINUE
C RATE CONSTANTS - ELECTRONIC
  VD=SQRT(2*TE/MASA)*3E10
  J=NE*E*VD
  VDISC=V-R*J*A-I.*A*E*VD*(NE-NEP)/DT
  NEP=NE
  RC=6.38E7*(SQRT(2*TE))*3
  R1=RC*EXP(-EMI/TE)*(1.+EMI/(2*TE))*(NE*CM1*M)
  R1B=(R1/M)*EXP(EMI/TE)*M1*.25
  R1X=RC*EXP(-EX1/TE)*(1.+EX1/(2*TE))*(NE*CX1*XE)
  R1XB=(R1X/XE)*EXP(EX1/TE)*XE1*.25
  R37=RC*EXP(-EM2/TE)*(1.+EM2/(2*TE))*(NE*CM2*M)
  R37B=(R37/M)*EXP(EM2/TE)*M2*.1
  R37X=RC*EXP(-EX2/TE)*(1.+EX2/(2*TE))*(NE*CX2*XE)
  R37XB=(R37X/XE)*EXP(EX2/TE)*XE2*.1
  R39=RC*EXP(-(EMI-EM1)/TE)*(1.+(EMI-EM1)/(2*TE))*
+ (NE*CM1I*M1)
  R39=RC*EXP(-(EMI-EM2)/TE)*(1.+(EMI-EM2)/(2*TE))*
+ (NE*CM2I*M2)
  R38X=RC*EXP(-(EX1-EX1)/TE)*(1.+(EX1-EX1)/(2*TE))
+*(NE*CX1I*XE1)
  R39X=RC*EXP(-(EX1-EX2)/TE)*(1.+(EX1-EX2)/(2*TE))
+*(NE*CX2I*XE2)
  R2=RC*EXP(-EMI/TE)*(1.+EMI/(2*TE))*(NE*CM1*M)
  R2X=RC*EXP(-EX1/TE)*(1.+EX1/(2*TE))*(NE*CX1*XE)
  R4=.29E-8*MDI*NE/(SQRT(TE))
  R4X=.346E-6*XEDI*NE/(SQRT(TE))
  R4MX=.346E-7*XEMI*NE/(SQRT(TE))
  R17 = 9.1E-10*TE**(-2.16)*EXP(-.165/TE)*NE*FL
  R28=2E-8*XEFU*NE
  R28R=2E-8*EXP(-XEFU/TE)*NE*XEFG
  REL=(NE*CEL*M*SQRT(2*TE/MASE))*3E10*(2*MASE/MASM)*TE

```

RATE CONSTANTS - GAS KINETIC

$SQRTG = \sqrt{TG}$   
 $K3X = 1.E-23 * EXP(.6/TG)$   
 $K5X = 1.E-23 * EXP(1.5/TG)$   
 $K41 = 1.E-23 * EXP(.074/TG)$   
 $G3 = M * 3.7E-31 * M * MI * SQRTG$   
 $G3X = XE * 12E-31 * M * XE1 * SQRTG$   
 $G3MX = M * 5.8E-31 * M * XE1 * SQRTG$   
 $G3XB = 12E-31 * XE * XEDI / K3X * SQRTG$   
 $G5 = M * 12E-33 * M * MI * SQRTG$   
 $G5X = M * 15E-32 * XE * XE1 * SQRTG$   
 $G5MX = M * 47E-33 * M * XE1 * SQRTG$   
 $G5XB = 15E-32 * XE * XEDI / K5X * SQRTG$   
 $G13 = 29E-10 * MI * XE * SQRTG$   
 $G14 = 29E-10 * MD1 * XE * SQRTG$   
 $G18 = 0; G18X = 34.7E-10 * SQRTG * XE1 * FL$   
 $G20 = 0; G20X = 35E-10 * XEDI * FL * SQRTG$   
 $G22 = 5E-7 * MI * FNI * SQRTG$   
 $G22X = 17E-7 * XE1 * FNI * SQRTG$   
 $G23 = 3E-25 * MI * FNI * M * SQRTG$   
 $G23X = 12E-25 * XE1 * FNI * M * SQRTG$   
 $G24 = 5E-7 * MD1 * FNI * SQRTG$   
 $G24X = 17E-7 * XEDI * FNI * SQRTG$   
 $G25 = 3E-25 * MD1 * FNI * M * SQRTG$   
 $G25X = 12E-25 * XEDI * FNI * M * SQRTG$   
 $G27X = 46E-10 * XEFU * FL * SQRTG$   
 $G31 = 10E-10 * MI ** 2 * SQRTG$   
 $G31X = 30E-10 * XE1 ** 2 * SQRTG$   
 $G31MX = 20E-10 * XE1 * MI * SQRTG$   
 $G32 = 10E-10 * MI * MD1 * SQRTG$   
 $G32X = 30E-10 * XE1 * XEDI * SQRTG$   
 $G32MX = 20E-10 * MI * XEDI * SQRTG$   
 $G33 = 10E-10 * MD1 ** 2 * SQRTG$   
 $G33X = 30E-10 * XEDI ** 2 * SQRTG$   
 $G33MX = 20E-10 * XEMI ** 2 * SQRTG$   
 $G34 = 10E-10 * MI * XEFU * SQRTG$   
 $G34X = 30E-10 * XE1 * XEFU * SQRTG$   
 $G34MX = 0$   
 $G35 = 10E-10 * MD1 * XEFU * SQRTG$   
 $G35X = 30E-10 * XEDI * XEFU * SQRTG$   
 $G35MX = 20E-10 * XEMI * XEFU * SQRTG$   
 $G40 = F * 1E-32 * F * M * SQRTG$   
 $G41 = M * 2E-32 * XE * F * SQRTG$   
 $G41B = 2E-32 * M * XEFG / K41$   
 $G44 = 6E-32 * F * XE1 * M * SQRTG$   
 $GSTM = 2.6E-17$

ORIGINAL PAGE IS  
OF POOR QUALITY

C DIFFUSIN RATES

$KPLUS = .44E3 * (3E16 / (XE + M)) * \sqrt{.03/TG}$   
 $KNI = 2E3 * (3E16 / (XE + M)) * \sqrt{.03/TG}$   
 $KFI = VD / (VDISC / LENGTH)$   
 $DPLUS = 12 * (3E16 / (XE + M)) * \sqrt{.03/TG} ** 3 * (4.8/D) ** 2$

```

DNI=30*(3E16/(XE+M))*SQRT(TG/.03)**3*(4.8/D)**2
DEL=SQRT(2*TE/MASE)*3E10/(3*CEL*(XE+M))*(4.8/D)**2
DXE=SQRT(2*TG/MASXE)*3E10/(3*(M+XE)*CDIF)*(4.8/D)**2
DM=LXE*SQRT(MASXE/MASM)
DAPOS=DPLUS-KPLUS*(DPLUS*XEI-DNI*FNI-DEL*NE)/
+(KPLUS*XEI+KNI*FNI+KEL*NE)
DANEG=DNI+KNI*(DPLUS*XEI-DNI*FNI-DEL*NE)/(KPLUS*XEI+KNI*FNI+
+KEL*NE)

```

C RATE EQUATIONS

```

M1=M1+DT*(R1+R4+G22+G5B-G5-G1B-R1B-G13-G31-D1*M1)
M2=M2+DT*(R37+R4-AM2*M2-R37B)
MI=MI+DT*(R2+G3B+R3B+R39-G3-G22-G23-DAPOS*MI)
XE1=XE1+DT*(R1X+R4X+G22X+G5XB-G5X-G18X-R1XB-G31X-R38X- )XE*XE1)
XE2=XE2+DT*(R37X+R4X-AXE2*XE2-R37B)
XEI=XEI+DT*(R2X+G3XB+G3MXB+G13+G14+R38X+R39X-G3X-G34X-G22X-G23X
+-DAPOS*XEI)
MDI=MDI+DT*(G3+G31+G32+G33+G34+G35-R4-G24-G25-G3B-DAPOS*MDI)
XEDI=XEDI+DT*(G5X+G24X-AXED*XEDI-G5XB)
XEDI=XEDI+DT*(G3X+G31X+G32X+G33X+G34X+G35X-R4X-G24X-G25X-G3XB
+-DAPOS*XEDI)
XEMI=XEMI+DT*(G54X+G24MX-AMX*XEMI-G5MXR)
XEMI=XEMI+DT*(G3MX+G31MX+G32MX+G33MX+G34MX+G35MX-R4MX-(G24MX-G25MX)-
+G3MXB-DAPOS*XEMI)
FNI=FNI+DT*(R17-G22-G22X-G23-G23X-G24-G24X-G25-G25X-DANEG*FNI)
FL=FL+DT*(R17B+G40-R17-G18-G18X-G20-G20X)
XEFG=XEFG+DT*(AXEF*XEFU+R2B+G27X+G35+G41+G35X-R28B-G41B)
XEFU=XEFU+DT*(G18X+G20+G23X+G25X+R28B-AXEF*XEFU-G27X-R23-G34-G34X-
+G35-G35X)
F=F+DT*(R17+G18X+G20X+G22+G22X+G24+G24X+G25+G25X+2*G27X+G34+G34X+
+41B
+ -G44-G41-2*G40)

```

C GAS TEMPERATURE

```

TG=TG+DT*2/(3*M)*(NE*VD*(VDISC/LENGTH)-(4.8/D)**2*K*(TG-TG0))

```

C GAIN

```

GAIN=CSTIM*(XEFU-XEFG*EXP(-.074/TG))

```

C OUTPUT

```

IF(ISTEP/IPRINT-FLOAT(ISTEP)/FLOAT(IPRINT)) 31,30,31
30 CONTINUE
WRITE(5,90) T,VDISC,J,NE,FNI,MI,XEI
90 FORMAT(7(E10.2))
WRITE(5,95) FL,XE1,XEFU,XEFG,GAIN,TG,TE
95 FORMAT(3X,7(E10.2))
31 CONTINUE
GO TO 20
22 WRITE(5,200)
200 FORMAT(2X,19H>0, GO 0.1---<0, END)
ACCEPT*,Z
IF(Z) 41,41,42
42 WRITE(5,250)
250 FORMAT(2X,28HNEW VALUES: DT, TMAX, IPRINT)
ACCEPT*,DT,TMAX,IPRINT

```

```

1 STEP=0
GO TO 20
STOP
41 END
FUNCTION FUNC(TE)
REAL M, M1, M2, NE, MASE, MASM, LENGTH, NEP, L
COMMON/STOR/M, XE, NE, NEP, CM1, CX1, XEFG, EM1, EX1, EXEFU, CEL,
+ MASE, MASM, V, LENGTH, A, L, R, DT, E, FL
VD=SQRT(2*TE/MASM)*3E10
RC=6.38E7*(SQRT(2*TE))**3
IF (TE-.4) 51,52,52
51 R1=0.; RIX=0.; GO TO 53
52 CONTINUE
R1=RC*EXP(-EM1/TE)*(1.+EM1/(2*TE))*(CM1*M)
RIX=RC*EXP(-EX1/TE)*(1.+EX1/(2*TE))*(CX1*XE)
53 CONTINUE
R17=9.1E-10*TE**(-2.16)*EXP(.165/TE)*FL
R28B=2E-8*EXP(-EXEFU/TE)*XEFG
REL=(CEL*M*SQRT(2*TE/MASE))*3E10*(2*MASE/MASM)*TE
FUNC=(V-R*A*E*NE*VD-L*A*E*VD*(NE-NEP)/DT)/LENGTH
+ -(1/VD)*(RIX*EX1+R1*EM1+R17*TE+R28B*EXEFU+REL)
RETURN;END

```

ORIGINAL PAGE IS  
OF POOR QUALITY

## C KARTV - KAR/K2 LASER

REAL MASE, MASXE, MASM, M1, M2, MI, K, K3X, K5X, K41, NEO, NE  
 REAL LAMDE, LAMDD, KAEX, KADI, KXEX, KXDI  
 REAL NEP  
 REAL J  
 REAL LENGTH  
 REAL KPLUS, KNI, KEL  
 REAL L  
 EXTERNAL FUNC  
 COMMON/STOR/XE, P, CP1, CK1, NE, NEP, L, A, R, DT, E,  
 + EP1, EX1, CEL, MASE, MASXE, V, LENGTH, P1, CP1 I, CPI, RX1  
 COMMON/STI/TE

## C CONSTANT DATA

MASE=0.5E6; E=1.6E-19; MASXE=39.9\*1840\*.5E6  
 R=0  
 L=0  
 D=1  
 A=27

## C XE=ARGON

LAMDE=.83E-4  
 LAMDD=1.04E-4  
 REX=3.3E-8  
 RDI=5.4E-8  
 RDIE=4.3E-8  
 DRDFE=.53E-8/(612)  
 DRDFD=1E-8/(.04E4)  
 DRDFDE=.4E-8/(1.388E3)  
 VEA=-.0199  
 VEX=.094  
 VDA=-.66  
 VDX=-.262  
 VDXE=-.520  
 EP1=1.61  
 EP2=3.5  
 EPI=5.138  
 EPX1=1.46  
 EPXI=4.19  
 EPDT=1.03  
 EPD1=1.46  
 EPDI=4.19  
 CPDT=3E-15  
 CEL=3E-15  
 CP1=6E-15  
 CP2=6E-16  
 CPI=.5E-16  
 CPII=3E-15  
 CPX1=6E-15

ORIGINAL PAGE IS  
 OF POOR QUALITY

```

CPXI=.5E-16
CPDI=6E-15
CPDI=.5E-16
CPHI=.05E-13
CDIF=1E-15
EXI=11.5
CXI=3E-17
SA=0.49E4;SB=7.13
LENGTH=1
K=160E19
AX2=4E7;AP=3.69E7;AXEDI=4E7
OSTME=AP/2*LA*DE**2*DEX**2*DRDFE
OSTMD=AP/2*LA*DD**2*DDI**2*DRDFD
OSTMDE=AP/2*LA*DE**2*DDI**2*DRDFDE

```

C INITIAL CONDITIONS

```

WRITE(5, 50)
50 FORMAT(2X,2HXE,2X,2HTG,2X,1HV,2X,
+2HDT,2X,6HIPRINT,2X,4HTMAX,2X,1HC,2X,3HCXI)
ACCEPT*,XE,TG,V,DT,IPRINT,TMAX,C,CXI
W=3E1; DELAY=1E-4
PO=3.5E16*(273/(273+TG))*10**(SB-.052*SA/(TC+273))
TG=(TG+273)*(1/1.16E4)
TG0=TG
F=W/(1.6E-19*EPI)*(1.24/EPI-.2)
KXDI=1.8E-22*EXP(.56/TG)
KXEX=2.2E-23*EXP(-.05/TG)
PX=KXEX*PO*XE
PDE=KXDI*PO**2
PD=PDE
PX=KXEX*PO*XE
PI=F*CPHI*PO*DELAY
PI=10.*PI
AT=AP*1.6/(8.3E-15*PO*DT)
IF(AT-AP) 13,17,17
17 AT=AP
13 CONTINUE
WRITE(5, 82) PO,PDE,PI
82 FORMAT(2X,'PO=',E10.3,5X,'PDE=',E10.3,5X,'PI=',E10.3)
WRITE(5, 80)
80 FORMAT(4X,4HTIME,6X,5HVDISC,5X,1HJ,9X,2HNE,8X,4HPLAV,
+3X,2HPD,7X,3HPDI)
WRITE(5, 85)
85 FORMAT(7X,1HP,9X,2HPI,3X,5HGAIN,5X,5HGAIND,5X,5HBETA,5X,5HBETAD,
+5X,2HTE)

```

C TIME STEP

```

20 ISTEP=ISTEP+1
T=T+DT
IF(T-TMAX) 21,21,22
21 CONTINUE

```

C CIRCUIT RESPONSE

P=PO-(PI+PI)  
 NE=PI  
 V=V-DT\*J\*A/C  
 IERR=0; IND=1; EPS=.01  
 TE=SOLN(IND, FUNC, .2, 5., EPS, IERR)  
 IF(IERR .GT. 1, 2, 1)  
 1 WRITE(5, \*) IERR; GO TO 30  
 STOP

2 CONTINUE

C RATE CONSTANTS - ELECTRONIC

VD=SQRT(2\*TE/HASXE)\*3E10  
 J=XE\*E+VD  
 VDISC=V  
 NEP=NE  
 RC=6.39E7\*(SQRT(2\*TE))\*3  
 RPI=RC\*EXP(-EPI/TE)\*(1+EPI/(2\*TE))\*(NE\*CP1)\*P  
 RPIE=RPI/P\*EXP(EPI/TE)\*P1\*.33  
 RPI=RFN(EPI)\*(NE\*CP1)\*P  
 RPII=RFN(EPI-EPI)\*(NE\*CP1I)\*P1  
 RPXI=RFN(EPX1)\*(NE\*CPX1)\*PX  
 RPXIB=RPXI/PX\*EXP(EPX1/TE)\*PX1\*.5  
 RPXI=RFN(EPX1)\*(NE\*CPX1)\*PX  
 RPD1=RFN(EPD1)\*(NE\*CPD1)\*PD  
 RPD1B=RPD1/PD\*EXP(EPD1/TE)\*PD1\*.25  
 RPDD=RFN(EPDT)\*(NE\*CPDT)\*PD  
 RPD1=RFN(EPD1)\*(NE\*CPD1)\*PD  
 RECP=PI\*2.28E-26\*NE\*TE\*\*(-4.39)\*NE  
 RECPX=1.E-8\*PX1\*NE  
 RECPD=1.E-8\*PD1\*NE

C RATE CONSTANTS - GAS KINETIC

SGRTG=SQRT(TG)  
 KAEX=2.2E-23\*EXP(.074/TG)  
 KADI=6.5E-23\*EXP(.735/TG)  
 KXEX=2.2E-23\*EXP(-.05/TG)  
 KXDI=1.8E-22\*EXP(.56/TG)  
 GPX=XE\*8E-32\*XE\*PI  
 GPXB=XE\*8E-32/KAEX  
 GPD=P\*(XE\*1E-30\*PI)  
 GPDE=(XE\*1E-30)/KADI  
 GPDX=P\*(XE\*1E-31\*P)  
 GPDXB=(XE\*1E-31)/KADI  
 GPXI=(XE\*8E-32\*XE)\*PI  
 GPXIB=(XE\*8E-32\*PX1)/KAEX  
 GPD1=(XE\*8E-30\*P)\*PI  
 GPD1B=(XE\*8E-30\*PD1)/KADI

ORIGINAL PAGE IS  
 OF POOR QUALITY

DIFFUSION RATES

KPLUS=2E3\*(3E16/(XE))\*SQRT(.03/TG)  
 KEL=VD/(VDISC/LENGTH)  
 DXE=SQRT(2\*TG/MASXE)\*3E10/(3\*(XE)\*CDIF)\*(4.8/D)\*\*2  
 DAPOS=KPLUS\*TE\*(4.8/D)\*\*2  
 DP=DXE\*1.3

RATE EQUATIONS

PI=P1+DT\*(RP1+RECP+RECPX+RECPD-RP1B-AP\*(PX1)-DP\*PI)  
 IF (PI/P-3\*EXP(-EPI/TE)) 8,9,9  
 9 P1=P\*3\*EXP(-EPI/TE)  
 8 CONTINUE  
 PX=KXEX\*P\*XE  
 IF (PD-PDE) 61,61,62  
 62 PD=PDE;GO TO 65  
 61 CONTINUE  
 PD=PD+DT\*(GPD+RPDI-RPDXB\*PD-RPDI-RPDD)  
 65 CONTINUE  
 PDI=PDI+DT\*(GPD+RPDI-(GPD+AP)\*PDI-RPDI)  
 PI=PI+DT\*(RP1+RP1I+RP2I+GPN\*P+P\*CPHI\*F-RECP-RECPX-RECPD-DAPOS\*PI)  
 PX1=GPX/(GPXB+AP)  
 PXI=KAEX\*PI\*XE  
 PDI=KADI\*P\*PI

GAS TEMPERATURE

TG=TG+DT\*(NE\*VD\*VDISC/LENGTH-(4.8/D)\*\*2\*K\*(TG-TG0))\*2/(3\*XE)

GAIN

BETA= CSTME\*2\*P\*XE\*EXP(-VEX/TG)/3E10+CSTMDE\*PD/KXDI\*EXP(-VDXE/  
 +TG)\*.25/3E10  
 BETAD=CSTMDE\*PD/KXDI\*EXP(-VDX/TG)\*.25/3E10  
 GAIN=CSTMDE\*(PX1\*EXP(-VEA/TG)/(KAEX\*1.5)-2\*P\*XE\*EXP(-VEX/TG))/3E10  
 +CSTMDE\*(PD/KXDI\*EXP(-VDXE/TG)\*.25)/3E10  
 GAIN=CSTMDE\*(.25\*PDI\*EXP(-VDA/TG)/(KADI\*12)-  
 +PD/KXDI\*EXP(-VDX/TG)\*.25)/3E10  
 PLAM=235E-21\*(GAIN+BETA)/LAMDE\*\*5

OUTPUT

IF (ISTEP/IPRINT-FLOAT(ISTEP)/FLOAT(IPRINT)) 31,30,31  
 30 CONTINUE  
 RCPDT=RFN(EPDT)\*CPDT  
 WRITE(5,\*) TG  
 WRITE(5,90) T,VDISC,J,NE,PLAM,PD,PDI  
 90 FORMAT(7(E10.2))  
 WRITE(5,95) P,P1,GAIN,GAIN,BETA,BETAD,TE  
 95 FORMAT(3X,7(E10.2))  
 31 CONTINUE  
 GO TO 20  
 22 WRITE(5,200)  
 200 FORMAT(2X,19H>0, GO ON---<0, END)  
 ACCEPT\*,Z  
 IF(Z) 41,41,42  
 42 WRITE(5,250)

```

250 FORMAT(2X,28HNEW VALUES: DT, TMAX, IPRINT, F)
ACCEPT*, DT, TMAX, IPRINT
ISTEP=0
GO TO 20
STOP
41 END
FUNCTION FUNC(TE)
REAL NE, MASE, MASXE, LENGTH, NEP, L
COMMON/STOR/XE, P, CPI, CX1, NE, NEP, L, A, R, DT, F,
+ EP1, EX1, CEL, MASE, MASXE, V, LENGTH, PI, CPII, CPI, RXI
VD=SQRT(2*TE/MASXE)*3E10
RC=6.38E7*(SQRT(2*TE))**3
RXI=RC*EXP(-EX1/TE)*(1+EX1/(2*TE))*CX1*XE
REL=(CEL*XE*SQRT(2*TE/MASE))*3E10*(2*MASE/MASXE)*TE
FUNC=(V-R*A*E*NE*VD)/LENGTH-(1/VD)*(RXI*EX1+REL)
RETURN;END
FUNCTION RFN(Y)
COMMON/STE/TE
RFN=6.38E7*(SQRT(2*TE))**3*EXP(-Y/TE)*(1+Y/(2*TE))
RETURN;END

```

ORIGINAL PAGE IS  
OF POOR QUALITY